

https://dspace.org/

Synthesis and characterization of novel colloidal gold selenide nanostructures and their application as counter electrodes for dye-sensitized solar cells

Machogo, Lerato Florence Eugenia

2020

https://hdl.handle.net/10539/31026

Downloaded from a DSpace repository. https://dspace.org/

Synthesis and characterization of novel colloidal gold selenide nanostructures and their application as counter electrodes for dye-sensitized solar cells



A thesis submitted to the Faculty of Science, University of the Witwatersrand,
in partial fulfilment for the degree
Doctor of Philosophy

By

Lerato Florence Eugenia Machogo
Student number:
690585

_____ _____

Lerato F.E. Machogo Date

_____ _____

Supervisor:
Prof. Nosipho Moloto Date

_____ _____

Co-supervisor:
Dr Poslet M. Shumbula Date

Declaration

I declare that the work reported herein is my own independent work, submitted at the School of Chemistry, University of the Witwatersrand, Johannesburg. This work has not been submitted for any degree or examination in any other institution of higher learning.

_____ _____

Lerato F.E. Machogo Date

Abstract

Energy demands have been on the rise lately due to the growing global population. Projection of global energy consumption has been estimated to increase by 44% between the periods 2006 to 2030. This puts tremendous pressure on most developing countries, who still today, generate majority of their electricity through burning of fossil fuels such as coal. These countries, like South Africa, therefore, need to upscale their energy production but also need to take into account the adverse environmental implications (i.e. increase in carbon emissions) that the "traditional" routes may have. Having this in mind and the perception of possible fossil fuel depletion, cleaner, renewable and more sustainable sources for energy generation need to be strongly considered. Harnessing of solar energy has over the years proven to effectively work through various types of photovoltaic/solar cell technologies. However, highly efficient devices in the market are commercially expensive, hence there is a need to reduce on these costs yet maintaining comparable power conversion efficiencies (PCEs). Dye-sensitized solar cells (DSSCs) are a cost-effective and environmentally friendly option, which has previously reported promising PCEs. However, the use of the corrosion-prone Pt metal counter electrode (CE) hinders the stability and reproducibly of the device long term. Hence the current study focused on synthesis of 2D-layered gold selenide (AuSe) nanomaterials for potential use as a CE in DSSCs.

The colloidal synthesis using varied molar ratios of gold to selenium precursors yielded polymorphic samples with β-AuSe being the predominant phase over α-AuSe. Temperature studies showed that synthesis at lower temperatures gave high impurities of unreacted selenium where excess reduced gold was observed at high working temperatures. The ideal temperature was thus 200 °C which was used in subsequent experiments. Adding precursors in a different sequence to improve on the purity of AuSe instead produced intriguing morphology differences. XRD, TEM and SEM showed that the addition of gold at higher temperatures gave long flexible α-AuSe dominated nanobelts, contrary to the β-AuSe nanoplates observed when gold was added at lower temperatures. The α-AuSe nanobelts also had β-AuSe spherical deposits on their surfaces, which explained most of the polymorphism observed in all the as-synthesized samples. EDS mapping showcased the level of homogeneity of the AuSe nanostructures which presented each particle having both Au and Se at an appreciable amount. The use of different capping agents produced α-AuSe dominated materials, however, 1DDT had short rod-like nanostructures and OLA and OA depicted nanobelts. OLA was the preferred

stabilizing agent in producing AuSe as a result of giving more of the desired product than the other two which gave more of Au and Se impurities. DFT studies confirmed the preference for nanobelt morphologies for OLA and OA capped particles.

XPS not only depicted the presence of the Au^{+} ions, it also confirmed Au–Se bonding in the Se 3d high resolution spectra where a strong presence of the Au5p peak was observed. The presence of Au^{3+} ions in the AuSe system was confirmed by vibrational shifts associated with the square planar geometry in Raman spectroscopy. These results were true for both α- and β-AuSe. The electrocatalytic activity of AuSe was illustrated by using cyclic voltammetry. Alpha-AuSe CE had a lower ΔEpp value (532 mV) and a higher cathodic peak current of 6.1 mA while β-AuSe CE had 739 mV for ΔEpp and 4.2 mA for the cathodic peak current. AuSe therefore, showed good redox catalytic activity, stability and reproducibility towards the I^{-}/I_3^{-} electrolyte, illustrating its potential as a counter electrode in dye-sensitised solar cells.

Dedication

I dedicate this work to my mother Vivian Machogo, my grandmother Pulane Kodisang, my fiancé Neo Phao and my family at large.

Acknowledgments

- My sincerest appreciation goes to my supervisors Prof Nosipho Moloto and Dr Poslet Shumbula, you have nurtured me from my Honours infancy days, helped me go through some of my fuzziest scientific moments and encouraged me to spread my wings and fly. Thank you for trusting me with this project and for your immeasurable support and guidance.
- Successful completion of this work would have not been possible without the valuable guidance and contributions from outstanding researchers, Dr Mbuso Mlambo, Prof Phumlane Mdluli and Prof Neil Coville. Thank you all.
- My appreciation also goes to Mintek and Tiso Foundation for funding my studies. The School of Chemistry at University of the Witwatersrand for affording me the opportunity to conduct my research. The Mujeres por Africa Foundation for funding my research visit at the University of Malaga, Spain.
- The LAB330B group and CATMAT group, your constructive criticism meant a great deal. The endless “Lab 330B talk sessions” with Rudo Sithole, Dr Mildred Airo, Dr Siziwe Gqoba, Prince Shumbula, Grace Ngubeni, Lineo Mxakaza and Zakhele Ndala will forever be remembered for they geared me through those difficult lab days, I thank you. To all my friends, your valuable support has been greatly appreciated.
- I would like to thank my family for supporting me in pursuit of my dream and for all the sacrifices you have endured. Words truly cannot express my gratitude. Ke a leboga.
- To one of my biggest supporters, my loving fiancé. I could write another thesis on what your presence and constant encouragement has meant to me during this challenging journey. Thank you for always believing in me, sometimes more than I believed in myself. You are cherished.
- Most importantly, to God my creator, thank you for hearing my prayers and being with me always.

Conference presentations

- NANOSMAT – Africa 2018

Oral presentation Nov 2018

Title: Alpha and beta polymorphism of mixed valent AuSe: effect on the order of precursor addition

- 9th International Conference of the African Materials Research Society

Oral presentation Dec 2017

Title: Structural influence of amine and thiol surfactants on AuSe synthesis

- 16th Frontiers of Electron Microscopy in Materials Science

Poster presentation Sept 2017

Title: Structural influence of amine and thiol surfactants on AuSe synthesis

- Microscopy Society of Southern Africa

Poster presentation Dec 2016

Title: Capping gold selenide: formation of nanobelts

- Falling Walls Lab Johannesburg

Oral presentation Sept 2016

Title: Breaking the wall of the energy crisis

- International School of Solid-State Physics

Poster presentation Jul 2016

Title: Capping gold selenide: formation of nanobelts

- 6th International Conference on Nanoscience and Nanotechnology in Africa (NanoAfrica)

Oral presentation Apr 2016

Title: Formation of 2-D gold selenide nanobelts

- 42nd National Convention of the South African Chemical Institute

Poster presentation Nov 2015

Title: Capping gold selenide: formation of nanobelts

- 5th Gauteng Nanosciences' Young Researchers Symposium

Oral presentation Oct 2015

Title: Capping AuSe: formation of nanobelts

- 17th South African Chemical Institute Inorganic Chemistry Conference

Poster presentation Jun 2015

Title: Gold selenide - colloidal synthesis and characterization: concentration studies

- 7th International Symposium on Macro- and Supramolecular Architectures and Materials

Poster presentation Nov 2014

Title: Colloidal synthesis and characterization of gold selenide nanomaterials

Publications

- **Lerato F.E. Machogo**, Musa Mthimunye, Rudo K. Sithole, Phumlani Tetyana, Neo Phao, Grace N. Ngubeni, Mbuso Mlambo, Phumlane S. Mdluli, Poslet M. Shumbula and Nosipho Moloto, Elucidating the structural properties of gold selenide nanostructures, *New Journal of Chemistry*, (2019), 43, 5773 – 5782. {I did all the work in the lab, wrote and corrected the manuscript and did most of the characterization including XRD, TEM, SEM and UV-Vis. Raman and XPS were ran by experts of the techniques at various institutions, and I did the data interpretation. Other people's contributions were discussions on the results and some characterization, and the supervisors conceptualized the project}

- **Lerato F.E. Machogo**, Phumlani Tetyana, Rudo Sithole, Siziwe S. Gqoba, Neo Phao, Mildred Airo, Poslet M. Shumbula, Makwena J. Moloto and Nosipho Moloto, Unravelling the structural properties of mixed-valence α- and β-AuSe nanostructures using XRD, TEM and XPS, *Journal of Applied Surface Science*, (2018), 456, 973 – 979. {I did all the work in the lab, wrote and corrected the manuscript and did most of the characterization, including XRD and TEM. XPS on the samples was run by the instrument technician and I did the data analysis. Other people's contributions were discussions on the results and some characterization, and the supervisors conceptualized the project}

- Rudo K. Sithole, **Lerato F.E. Machogo**, Mildred A. Airo, Siziwe S. Gqoba, Makwena J. Moloto, Poslet Shumbula, Juanita van Wyk and Nosipho Moloto, Synthesis and characterization of Cu_3N nanoparticles using pyrrole-2-carbaldpropyliminato Cu(II) complex and $Cu(NO_3)_2$ as single-source precursors: the search for an ideal precursor, *New J. Chem.*, (2018), 42, 3042 – 3049. {I contributed with discussions on the XPS results}

- S. Gqoba, M. Airo, N. Ntholeng, **L. Machogo**, R. Sithole, M.J. Moloto, J. van Wyk, N. Moloto, Evolution of In_2S_3 nanoplates with time, *Materials Today: Proceedings* (2015), 3901 – 3908. {I contributed with discussions and TEM analysis}

- **Lerato F.E. Machogo**, Rudo K. Sithole, Neo Phao, Tshwarela Kolokoto, Siziwe S. Gqoba, Mbuso Mlambo, Phumlane S. Mdluli, Makwena J. Moloto, Poslet M. Shumbula and Nosipho Moloto, Probing the structure and functionalized surface of colloidal AuSe, *Journal of Materials Science*, (2019), Under review (JMSC-D-19-05229). {I did all the work in the lab, wrote and corrected the manuscript and did most of the characterization, including XRD, TEM and FTIR. Raman and XPS were ran by experts of the techniques at various institutions and I interpreted the data. Other people's contributions were discussions on the results and some characterization, and the supervisors conceptualized the project}

- **Lerato F.E. Machogo**, Rudo K. Sithole, Neo Phao, Zakhele B. Ndala, Kalenga P Mubiayi, Poslet M. Shumbula and Nosipho Moloto, Electrocatalytic activity of novel AuSe for potential use as a counter electrode in dye-sensitized solar cells, *RSC Nanoscale Advances*, (2019), Under review (NA-COM-07-2019-000465). {I did all the work in the lab, wrote and corrected the manuscript and did most of the characterization, including XRD, TEM, SEM and cyclic voltammetry. Other people's contributions were discussions on the results and some characterization, and the supervisors conceptualized the project}

- R.K. Sithole, **L.F. Machogo**, Tshwarela Kolokoto, Grace N Ngubeni, M.J. Moloto, J. van Wyk, N. Moloto, Substitution of hard nitrogen ions of Cu_3N nanocrystals with soft sulfur ions of DDT via the HSAB theory to form chalcocite and digenite nanocrystals, *Journal of Materials Chemistry and Physics*, (2019), Under review (MATCHEMPHYS-D-19-00924). {I contributed with discussions on the XPS results}

- R.K. Sithole, **L.F. Machogo**, P. M. Kalenga, M.J. Moloto, P. Shumbula, J. van Wyk, N. Moloto, Elucidating the effect of time on the structural and optical properties of copper (I) nitride nanocubes, *Journal of Materials Chemistry C*, (2019), Under review (TC-ART-2019-003368). {I contributed with discussions on the XPS results}

Research visits

- **University of Malaga, Spain | Feb – Aug 2017**

  Conducted research in the catalysis laboratory under the supervision of Professor Pedro Maireles and Dr Juan A. Cecilia

  Project Title: Catalytic oxidation of furfural to furoic acid using heterogeneous catalysts based on noble metals gold, palladium and platinum nanoparticles

- **Ettore Majorana Foundation and Centre for Scientific Culture, Erice (Italy) | July 2016**

  Attended an Energy summer school at the International School of Solid-State Physics in Erice, Italy where the primary aim was to present and teach about current and prospects for materials in energy. The school focused on application of these materials for renewable and sustainable energy.

Table of contents

Abstract iv
Dedication vi
Acknowledgments vii
Conference presentations viii
Publications x
Research visits xii
List of figures xvii
Chapter 1 xvii
Chapter 2 xvii
Chapter 3 xviii
Chapter 4 xix
Chapter 5 xix
Chapter 6 xx
List of tables xxi
Chapter 3 xxi
Chapter 4 xxi
Chapter 5 xxi
Chapter 6 xxi
List of abbreviations xxii
Synopsis xxiii
Chapter 1 25
General background 25
1. Introduction 25
2. Problem statement 29
3. Rationale and motivation 30
4. Aim and objectives 31
References 31
Chapter 2 33
Literature review 33
1. Introduction to 2D-layered materials 33
1.1 The case of graphene 33
1.2 2D-layered materials beyond graphene 35

1.2.1 Transition metal chalcogenides 36
1.2.2 Gold selenide (AuSe), a 2D-layered material 38
2. Synthesis of 2D-layered materials 41
2.1 New 2D heterostructures 41
2.2 Top down methods 42
2.3 Bottom up methods 44
2.3.1 Factors affecting colloidal 2D-layered materials 46
3. Applications of 2D-layered materials 47
3.1 Dye-sensitized solar cells 48
3.1.1 Photoanode 49
3.2.2. Electrolyte 50
3.2.3. Counter electrodes 50
References 52
Chapter 3 60
Unravelling the structural properties of mixed-valence α- and β-AuSe nanostructures using XRD, TEM and XPS 60
Abstract 60
1. Introduction 61
2. Experimental 62
2.1 Chemicals 62
2.2 Synthesis of gold selenide 62
2.3 Characterization 62
3. Results and discussion 63
4. Conclusion 72
Acknowledgments 72
References 72
Chapter 4 75
Elucidating the structural properties of gold selenide nanostructures 75
Abstract 75
1. Introduction 76
2. Experimental 77
2.1 Chemicals 77
2.2 Synthesis of the different materials of gold selenide 77
2.3 Characterization 78
3. Results and discussion 80

4. Conclusion....93
Acknowledgments....94
References....94
Chapter 5....97
Probing the structure and functionalized surface of colloidal AuSe....97
Abstract....97
1. Introduction....98
2. Experimental....99
2.1 Chemicals....99
2.2 Synthesis of gold selenide....100
2.3 Numerical simulations of the interaction of the capping ligands with AuSe surfaces....100
2.4 Characterization....100
3. Results and discussion....101
4. Conclusions....119
Conflicts of interest....120
Acknowledgments....120
References....120
Chapter 6....125
Electrocatalytic activity of novel AuSe for potential use as a counter electrode in dye-sensitized solar cells....125
Abstract....125
1. Introduction....126
2. Experimental section....127
2.1 Chemicals....127
2.2 Synthesis of gold selenide....127
2.3.1 Characterization....128
2.4 Fabrication of the counter electrode thin films....128
2.4.1 Characterization of the counter electrode (CE) thin films....129
3. Results and discussion....129
4. Conclusion....135
Conflicts of interest....136
Acknowledgments....136
References....136
Chapter 7....138
Overall conclusions and recommendations....138

7.1 Conclusions 138
7.2 Recommendations 139
Appendix 141
Chapter 3: Supporting information 141
Chapter 5: Supporting information 143

List of figures

Chapter 1

Fig. 1: South African map showing the distribution of renewable power plants. ……25

Fig. 2: South African map with average annual global solar irradiation on a horizontal surface. ……...……...26

Fig. 3: The three generations of photovoltaic technologies listing the different types of solar cells. ……..27

Fig. 4: Evolution of the number of publications for dye-sensitized solar cells. Inset is the share distribution of publications for each component of DSSCs in 2012. ……...……28

Fig. 5: Schematic representation of the components and of the basic operating principle of a DSSC. ……..…….29

Chapter 2

Fig. 1: Graphene, the building block for other dimensionalities of carbon allotropes. …….33

Fig. 2: Electronic band structure of single layer graphene. ……...34

Fig. 3: Year-wise publication plots for 2D materials including MoS_2, $MoSe_2$, black phosphorus, MXenes, and total 2D transition metal chalcogenides from 2005–2016. …...…..35

Fig. 4: Summary of 2D library as at 2013. ……36

Fig. 5: Crystalline structure of layered MoS_2 where the Mo atom is sandwiched between the S atoms and the distance between two layers is 6.5 Å. ……...……..36

Fig. 6: Band structure of MoS2 in bulk, multilayer, bilayer, and monolayer forms. ……37

Fig. 7: Crystal structure of layered α-AuSe and β-AuSe. ……..……...38

Fig. 8. Crystal structures of both α-AuSe and β-AuSe indicating the presence of the different gold sites (Au^{+} and Au^{3+}). ……..…..39

Fig. 9: Band structures of (a) monolayer and (b) bilayer β-AuSe. Note that x-CBM (y -VBM) denotes the CBM (VBM) along the x (y) direction. Green solid balls indicate the global VBM or CBM. ……...…40

Fig. 10: (a) Computational band structure of β-AuSe monolayer and (b) simulated absorption spectra of AuSe monolayer. ……41

Fig. 11: Building van der Waals heterostructures. If one considers 2D crystals to be analogous to Lego blocks (right panel), the construction of a huge variety of layered structures becomes possible. ……..……42

Fig. 12: Illustration of micro-mechanical exfoliation of 2D nanostructures. (a) Adhesive tape is pressed against a 3D crystal material so that the top few layers are attached to the tape (b). (c) The tape with crystals of layered material is pressed against the surface of a target substrate. (d) Upon peeling off, the bottom layer is left on the substrate. ……..……43
Fig. 13. Liquid exfoliation technique using chemical ultrasonication. ……..…...43
Fig. 14: Chemical vapour deposition (CVD) technique. ……..44
Fig. 15: Nucleation and growth process of nanocrystals in solution as described by LaMer and Dinegar. ……...45
Fig. 16. Schematic illustration of the effect of change in precursor ratio and the multi-injection method on single- and multi-layer MoS_2 nanosheets. ……..……46
Fig. 17: Schematic representation showing the types of technologies 2D-layered materials can be applied in. …….……...47
Fig. 18: Schematic illustrating the working principle of a DSSC. ……..…..48
Fig. 19: (a) CV curves, (b) EIS Nyquist plots and (c) Tafel curves. ……50

Chapter 3

Fig. 1: Crystal structure of (a) α-AuSe and (b) β-AuSe. ……...……60
Fig. 2: XRD patterns of material synthesized in (a) 15 min and (b) 60 min for molar ratios 1:1, 1:3.5, and 1:5. ($ denotes gold, * denotes selenium, β-AuSe (black indices) and α-AuSe (blue indices)). …….……63
Fig. 3: TEM micrographs of particles synthesized in 15 min and 60 min for molar ratios 1:1, 1:3.5, and 1:5. …….…..65
Fig. 4: HRTEM images of the nanobelt synthesized at 60 min from the 1:3.5 mol ratio reaction. …….……66
Fig. 5: XPS survey spectrum of gold selenide from the 1:3.5 molar ratio reaction at 60 min……67
Fig. 6: High resolution core level spectra of AuSe with focus on C1s, O1s, Au4f and Se3d ……68
Fig. 7: XRD patterns of the particles synthesized using 1:3.5 molar ratio for 60 min at (a) 160 °C, (b) 200 °C and (c) 280 °C. ($ denotes gold, * denotes selenium, β-AuSe (black indices) and α-AuSe (blue indices)). …….……70
Fig. 8: TEM images of the particles synthesized using 1:3.5 molar ratio for 60 min at 160 °C, 200 °C and 280 °C. …….……..70

Chapter 4

Fig. 1: Standard XRD patterns of α-AuSe, β-AuSe, elemental Au and elemental Se together with XRD patterns of as-synthesised materials using the different reaction methods A - D. **(Key: α** = α-AuSe, **β** = β-AuSe**, $** = elemental Au and * = elemental Se). ……81

Fig. 2: Crystal structure of (a) α-AuSe and (b) β-AuSe. ……...……82

Fig. 3: XPS survey spectrum of gold selenide sample produced from method A. ……83

Fig. 4: High resolution core level spectra of AuSe with focus on C1s, O1s, Au4f and Se3d. ……..84

Fig. 5: Schematic representation of D_{4h} point group Raman active vibrational modes of square planar $(Au^{3+}Se_4)^-$ molecule. ……86

Fig. 6: ***(i)*** Calculated Raman spectra of α-AuSe and β-AuSe and experimental Raman spectra of as-synthesized AuSe of sample A and C. ***(ii)*** Calculated Raman spectra of α-AuSe and β-AuSe and experimental Raman spectra of as-synthesized AuSe of sample B and D. ……..…..87

Fig. 7: TEM images of as-synthesized AuSe nanocrystals using the different reaction methods A - D (insert highlighting the nanospheres deposited onto the belts). ……..……89

Fig. 8: *(i)* HAADF STEM images of single nanocrystals from each sample A-D. *(ii)* Elemental mapping of Au, *(iii)* elemental mapping of Se and *(iv)* the summed elemental mapping of both Au and Se for samples A – D. ……90

Fig. 9: SEM images of as-synthesized AuSe nanocrystals using the different reaction methods A – D. ……...91

Fig. 10: UV-Vis absorption spectra of the as-synthesized AuSe. ……...…..92

Chapter 5

Fig. 1: 2D molecular structures of capping agents (a) oleylamine (OLA), (b) 1-dodecanethiol (1DDT) and (c) oleic acid (OA). ……..98

Fig. 2: TEM images of as-synthesized OLA-AuSe, 1DDT-AuSe and OA-AuSe nanocrystals……102

Fig. 3: Standard XRD patterns of elemental Au, elemental Se, α-AuSe and β-AuSe as well as powder XRD patterns of as-synthesized OLA-AuSe, 1DDT-AuSe and OA-AuSe. (Key: α = α-AuSe, β = β-AuSe, $ = elemental Au and * = elemental Se). ……...…..103

Fig. 4: Calculated Raman spectra of α-AuSe and β-AuSe and experimental Raman spectra of as-synthesized OLA-AuSe, 1DDT-AuSe, OA-AuSe nanocrystals. ……..….105

Fig. 5: FTIR spectra of the pure capping agents OLA, 1DDT and OA in red and that of the as-synthesized AuSe nanocrystals in black. ……..……107
Fig. 6: High resolution XPS spectra with focus on core levels of C1s, O1s, N1s and S2p for OLA-AuSe, 1DDT-AuSe and OA-AuSe. ……..……109
Fig. 7: High resolution XPS spectra with focus on the Au4f core level of OLA-AuSe, 1DDT-AuSe and OA-AuSe nanocrystals. (Deconvolution colour code: red curves = Au^0, blue curves = Au^+ and green curves = Au–X; where X = S or O). ……110
Fig. 8: High resolution XPS spectra with focus on the Se3d core level of OLA-AuSe, 1DDT-AuSe and OA-AuSe nanocrystals. (Deconvolution colour code: red curves = $3d_{5/2}$, green curves = $3d_{3/2}$, blue curves = Au 5p band and purple curves = Se^0). ……...112

Chapter 6

Fig. 1: A plot showing the trend in power conversion efficiencies (PCEs) of a few 2-dimensional layered transition metal chalcogenides. ……125
Fig. 2: Powder X-ray diffraction patterns of as-synthesized AuSe matched to standard powder patterns of α-AuSe, β-AuSe, and elemental Au and elemental Se.
(Key: α = α-AuSe, β = β-AuSe, $ = elemental Au and * = elemental Se). ……...……129
Fig. 3: TEM images of the as-obtained gold selenide materials. (A) showing the α-AuSe nanobelts and (B) the β-AuSe nanoplates. ……..130
Fig. 4: (i) SEM images of (A) α-AuSe and (B) β-AuSe counter electrodes. Elemental mapping of (ii) Au, (iii) Se and (iv) summed mapping of Au and Se. ……..……..131
Fig. 5: SEM-EDS of (A) α-AuSe-CE and (B) β-AuSe-CE showing the elemental composition of the materials on the FTO glass substrates. ……..131
Fig. 6: Cyclic voltammograms of the Pt, α-AuSe and β-AuSe counter electrodes at a scan rate of 100 mV/s for the I^-/I_3^- redox couple. ……..……132
Fig. 7: Cyclic voltammograms for (a) α-AuSe and (b) β-AuSe CEs at varying scan rates from 10 mV/s to 100mV/s. Dependence of anodic and cathodic peak currents on square root of scan rates for (c) α-AuSe and (d) β-AuSe CEs. ……...133
Fig. 8: Cyclic voltammograms for, (a) α-AuSe and (b) β-AuSe CEs for 60 consecutive cycles, with inserts showing the 1st and the 60th cycle for both electrodes. ……...134

List of tables

Chapter 3

Table 1: Summary of the atomic composition stoichiometric assignments obtained from the fitting of the XPS spectra reported in Fig. 6. ……..…..69

Chapter 4

Table 1: Table showing the sequence of precursor addition (where ▲ denotes heating). ……77

Table 2: Summary of the atomic composition stoichiometric assignments obtained from the fitting of the XPS spectra reported in Fig. 4. ……..…...85

Table 3: Summary of the Raman frequencies and their vibrational assignments. ……..…...88

Chapter 5

Table 1: Summary of the Raman frequencies and their vibrational assignments. ……...…..106

Table 2: Summary of the atomic composition and stoichiometric assignments obtained from fitting of XPS spectra reported in Fig. 7, 8 and 9 for the as-synthesised capped AuSe nanocrystals. ……...…114

Table 3.1: α-AuSe simulations **……..**116

Table 3.1: β-AuSe simulations ……..117

Chapter 6

Table 1: Summary of the absolute current and peak-to-peak separation (ΔEpp) of each CE ……133

List of abbreviations

The following is a list of abbreviations used in the text:

1DDT - 1-Dodecanethiol

CBM - Conduction band minimum

CE - Counter-electrode

CV - Cyclic Voltammetry

CVD - Chemical vapour deposition

DSSC - Dye-sensitised solar cell

EDS - Energy dispersive X-ray spectroscopy

FTIR - Fourier Transform Infrared spectrophotometry

FTO - Fluorine doped tin oxide

HOMO - Highest occupied molecular orbital

HRTEM - High-resolution transmission electron microscopy

ITO - Indium-doped tin oxide

LSPR - Localized surface plasmon resonance

LUMO - Lowest unoccupied molecular orbital

NC - Nanocrystal

OA - Oleic acid

OLA - Oleylamine

PCE - Power conversion efficiency

PV - Photovoltaic

SEM - Scanning electron microscopy

TEM - Transmission electron microscopy

TMC - Transition metal chalcogenide

UV-Vis - Ultraviolet-visible spectrophotometry

VBM - Valence band maximum

XRD - X-ray diffraction

XAS - X-ray absorption spectroscopy

XPS - X-ray photoelectron spectroscopy

Synopsis

Two-dimensional materials such as graphene and other layered transition metal chalcogenides have received considerable attention recently due to their intrinsic properties. Their large surface areas and layered structures affords them highly efficient for energy storage and conversion. Their tunable electronic structures make them attractive for use in various applications such as optoelectronics, batteries, sensors and supercapacitors. Unlike many other layered materials, gold selenide (AuSe) has not been fully explored and therefore is not well understood. Due to its layered structure, it has great potential in next-generation optoelectronics. The aim of the study was to synthesize layered AuSe nanostructures via a facile colloidal method. Various characterization techniques were employed to investigate the properties of the nanomaterials and cyclic voltammetry was used to determine the materials' electrocatalytic activity, which showcased the materials' potential as a counter electrode in dye-sensitized solar cells. The outline of the thesis is therefore shown below:

Chapter 1: In this chapter a general background on energy demands, solar as a renewable energy source, use of photovoltaics and the motivation of the study are discussed. Furthermore, the chapter addresses the aim of the study and the objectives undertaken to achieve it.

Chapter 2: This chapter provides an insight into semiconductor nanocrystals and particularly on two-dimensional layered transition metal chalcogenides. A review on their methods of preparation, factors affecting their properties and their use in dye-sensitized solar cells, particularly as counter electrodes.

Chapter 3: This chapter is a peer-reviewed published journal article detailing on this first ever reported colloidal synthesis and characterization of gold selenide nanomaterials, primarily investigating the effect of gold to selenium precursor ratios as well as different temperatures on the crystal structure and morphology. *Journal of Applied Surface Science,* (2018), 456, 973 - 979

Chapter 4: This chapter is a peer-reviewed published journal article which reports on the attempt in obtaining pure phase AuSe by varying the order of precursor addition. Furthermore, Raman spectroscopy studies (theoretical and experimental) were performed to probe the

structure of AuSe in order to establish the mixed valency of gold in the system. *New Journal of Chemistry*, (2019), 43, 5773 - 5782

Chapter 5: The chapter is a journal article submitted to the Journal of Materials Science and is currently under review. The article is a surface study that aims to outline the structural, vibrational and surface properties of colloidal AuSe brought about using different surfactants. *Journal of Materials Science*, (2019), JMSC-D-19-05229

Chapter 6: The chapter is a journal article submitted to RSC Advances and is currently under review. The article reports for the first time, electrocatalytic properties of AuSe in the redox reaction of the iodide-triiodide system to propose this layered material as an alternative counter electrode for the corrosion prone platinum metal in dye-sensitized solar cells. *RSC Nanoscale Advances*, (2019), (A-COM-07-2019-000465)

Chapter 7: In this chapter a summary and overall conclusion of the study are presented. In addition, recommendations for future work are provided.

Chapter 1

General background

1. Introduction

With an increase in global population, there has been a subsequent increase in energy (electricity) demand. In many cases, energy forms an integral part of a country's sustainable socio-economic development, food production, poverty eradication, health, peace and security [1]. Much of Africa's energy generation is through the burning of fossil fuels such as wood, oil and coal. One of the continent's leading developing country, South Africa, obtains most of its electricity from the state-owned powerhouse enterprise, Eskom, which produces 80% of its electricity from burning coal and in turn ranks South Africa high in the world's topmost contributors of carbon emissions [2-4].

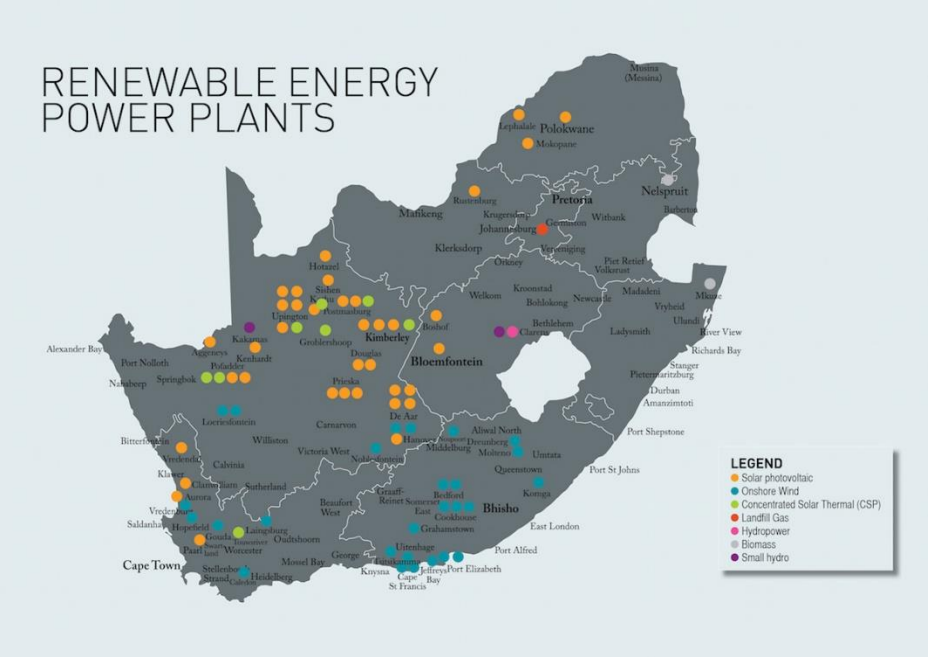

Fig. 1: South African map showing the distribution of renewable power plants [5].

Due to the adverse environmental implications of this process together with the thought and possibility of fossil fuel depletion, there have been tremendous efforts to transition to more renewable, abundant and sustainable energy sources such as wind, hydro and solar as shown in Fig. 1. With South Africa experiencing plenty of sunshine throughout most parts of the year,

the harnessing of solar energy has seen substantial growth in research and development of photovoltaics or solar cells to generate electricity [1, 6]. Fig. 2 presents the average annual global solar irradiation across South Africa [6] and therefore shows potential growth for the renewable and sustainable energy sector in the country.

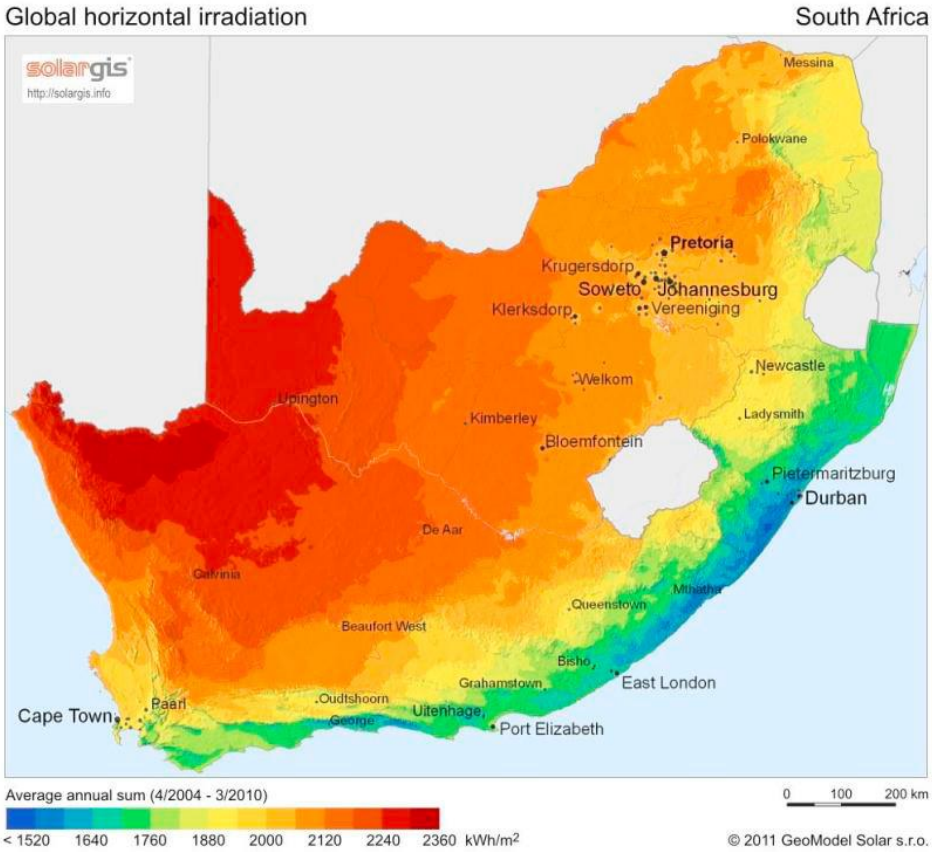

Fig. 2: South African map with average annual global solar irradiation on a horizontal surface [6].

While substantial progress has been made in transitioning to renewable energy as shown in Fig. 1, great potential exists in developing photovoltaics for portable applications in order to service the northern and central parts of South Africa which are characterized by mushrooms of informal settlements in the metropolis central regions and rural dwellings in the northern parts. Perhaps one of the most basic usages of electrical energy is in lighting however this is still a major hurdle in rural households and informal settlements. For lighting, the use of candles and kerosene lamps is commonplace. However, these present health risks due to fumes released especially in kerosene lamps and vulnerability to the breakout of fires which have been commonly observed in informal settlements in South Africa. To circumvent this, the use of

locally produced miniature solar panels for small power applications such as in lighting and in powering small devices such as mobile phones and radios is increasingly desirable.

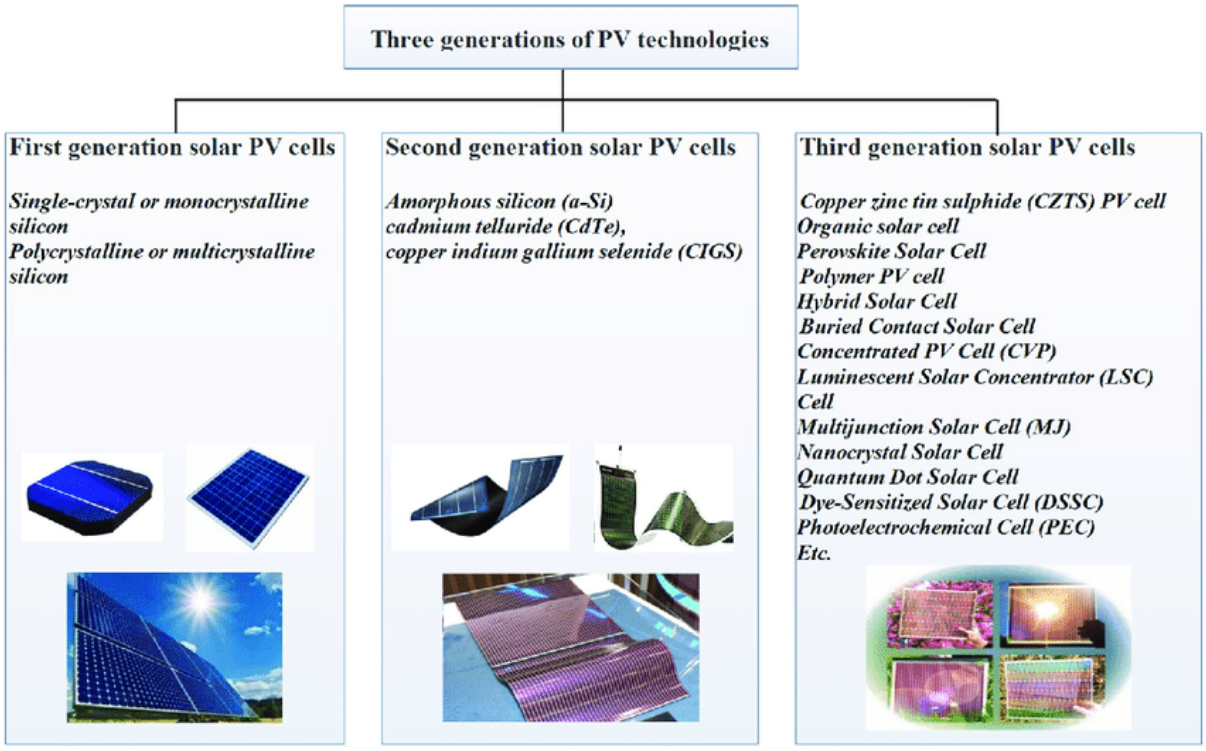

Fig. 3: The three generations of photovoltaic technologies listing the different types of solar cells [7].

Photovoltaic devices have mechanisms that absorbs and convert solar energy into electrical energy. Since the inception and implementation of solar cells, there have been considerable improvements from the 1st generation single-crystalline silicon based solar cells, which have the highest power conversion efficiency on the market but are on the expensive side of the manufacturing scale. In an attempt to overcome the high production costs, 2nd generation solar cells were developed. These use materials such as amorphous-silicon, gallium arsenide, cadmium telluride and copper indium gallium selenide through thin film processing technologies, however, they resulted in lower efficiencies. Due to the benefits of cheaper processing technologies that thin films provide, intensive research to improve their power conversion efficiencies by use of novel materials gave birth to 3rd generation solar cells. These include amongst many others, inorganic solar cells, organic solar cells and dye- sensitized solar cells (DSSCs) [7]. Fig. 3 gives a summary of the three generations of photovoltaic technologies and their types of solar cells [8]. DSSCs are the more favourable for portable applications due

to their low-cost, simple fabrication, flexibility (meaning they can be integrated in many products) as well as their environmental friendliness, thus drawing considerable attention [9].

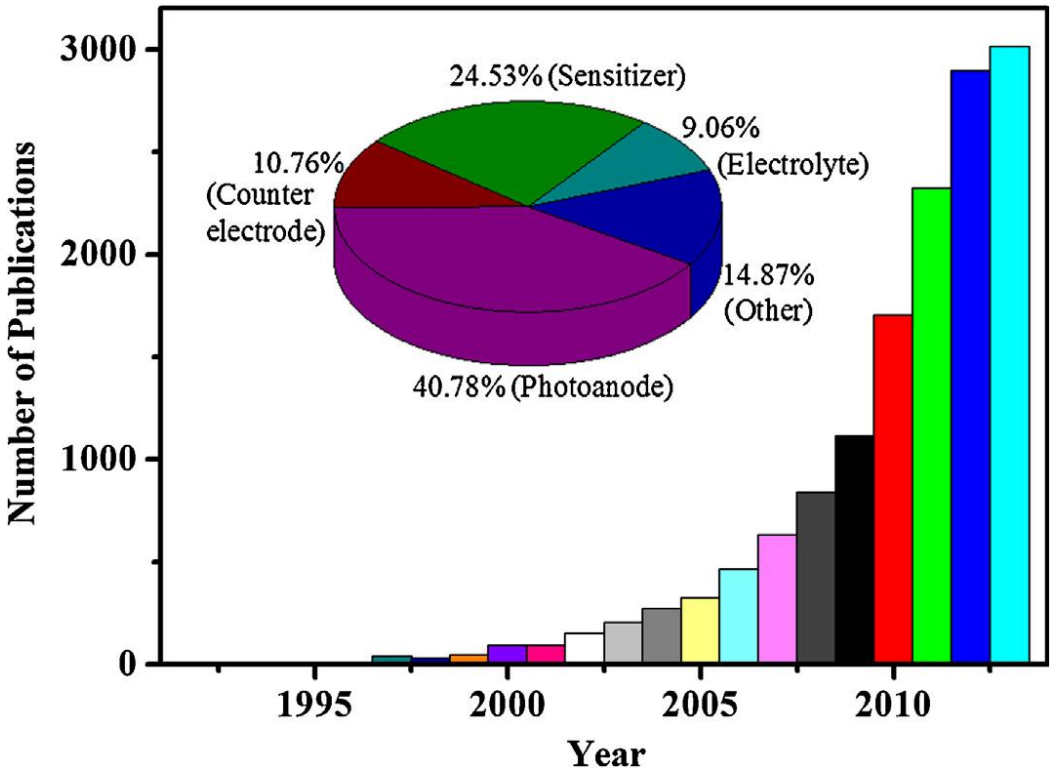

Fig. 4: Evolution of the number of publications for dye-sensitized solar cells. Inset is the share distribution of publications for each component of DSSCs in 2012 [11].

In just about 3 decades from the first assembled DSSC [10], great efforts have been invested into improving its technology. Its multicomponent structure gives it an added advantage as it allows for easy modification of individual parts of the device. There has been a rising interest and increased reports on research for the different components as seen in Fig. 4. Their simple fabrication process speaks to their simplistic principle of operation which they lend from the idea of natural photosynthesis in plants. When visible light illuminates the anode of the device, the absorbed dye molecules (sensitizer) get photo-excited and release high energy electrons. These excited electrons are transported to the conducting glass substrate (FTO or ITO) by the semiconducting TiO_2 molecules. The glass substrate then shuttles these electrons to the external circuit creating and electrical current (constant electron flow). The cathode receives electrodes from the external circuit where the counter electrode (usually platinum metal) assists in the regeneration of the dye by catalysing the redox reactions of the I^-/I_3^- electrolyte i.e. reduction of the triiodide ions to iodide which then ultimately donate electrons to the dye molecules

which were previously oxidized [11, 12]. A schematic representation of the working principle of DSSCs is provided in Fig. 5. Despite efforts in research on the counter electrode component, Pt metal is still widely used due to its excellent electrocatalytic activity even though it tends to corrode in the presence of the iodide-based electrolyte.

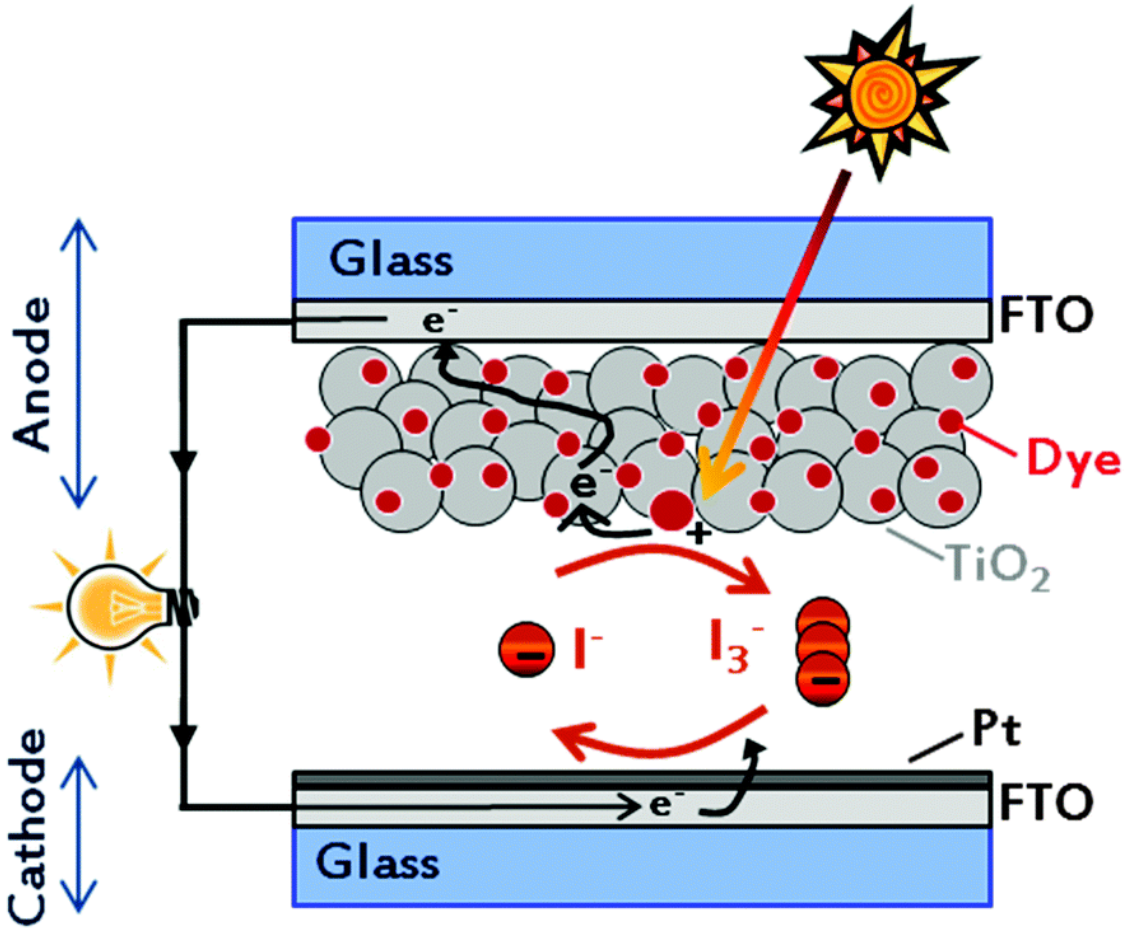

Fig. 5: Schematic representation of the components and of the basic operating principle of a DSSC [12].

2. Problem statement

Electricity plays a pivotal role in a country's development and economy. Relying on one source of electricity generation like the burning of coal (a finite resource with possible depletion overtime) poses a serious threat to its development. More natural and abundant resources such solar energy offer more environmentally friendly and sustainably viable options. First and second-generation solar cells have in the past shown to successfully produce electricity but the need to obtain better power conversion efficiencies at low manufacturing costs and this is still a concern. Dye-sensitized solar cells, through simple and cost-effective production methods, prove to be serious competitors in the energy sector. Improving the quality and stability of

these DSSCs in order to enhance their efficiencies is a matter of research interest. Finding alternative materials for components such as the corrosion susceptible platinum counter electrode (an important component for the regeneration of the dye) will greatly improve on current DSSCs and help progress the DSSC technology.

3. Rationale and motivation

Dye-sensitized solar cells have over the past couple of years gained much attention as a result of their promising efficiencies and cost-effective fabrication process. The latest report presented a 13% power conversion efficiency [13], which is a modest value however, there is still room for improvement in comparison to the 26% silicon based expensive solar cells [14]. DSSCs are multicomponent devices and therefore there are many aspects to it that can be altered to enhance the overall performance of the device. Herein, we propose the use of 2D layered gold selenide nanomaterials as a counter electrode in replacement of the commonly used Pt. As Pt tends to corrode in the presence of the iodine-triiodide electrolyte [15], the aim is to improve on the stability of the device by use of an alternative, electron rich counter electrode material without compromising on the catalytic efficiency. Furthermore, to keep to the cost-effectiveness of DSSCs, herein, we report on cheaper colloidal synthetic method that uses mild conditions and inexpensive chemistry apparatuses to produce 2D AuSe nanomaterials. Moreover, South Africa is one of the world's top producers of gold, and it is therefore in the country's best interest to explore the beneficiation of this mineral in the energy sector which could ultimately boost the economy. To emphasize on the previous point, Frank Holmes from U.S. Global Investors wrote the following statement about South Africa, "Once the top gold-producer in the world by a wide margin, South Africa's gold mines have been slowing every year since 2008, except for 2013 when production rose by a few tonnes. The nation is struggling with rising costs for electricity and labour, with many mines closing due to unprofitability. South Africa is, however, still home to the world's deepest gold mine, the Mponeng mine, extending 2.5 miles underground" [16]. It is, therefore, imperative that the country starts to focus on mineral beneficiation not only to make the mining sector more profitable but to also combat its energy crisis. Nosipho Moloto and Siyabonga P. Ngubane wrote an interesting article around this topic and their closing remarks were as follow, "South Africa has a real opportunity to kill two birds with one stone. The country can reinvent the now seemingly frail mining sector through beneficiation. It can also create a new sector encompassing energy production through photovoltaics and energy storage through batteries. This will not only cater for all our energy needs but also create new jobs" [17].

4. Aim and objectives

The aim was to use a facile colloidal method to synthesize gold selenide (AuSe) nanomaterials and to fully explore and understand the relatively understudied layered transition metal chalcogenide using various characterization techniques. Furthermore, to investigate the electrocatalytic properties of the as-obtained AuSe nanomaterials for application as a counter electrode in DSSCs.

As such, the following objectives were identified:

- To obtain the optimum reaction conditions for the synthesis of AuSe nanomaterials by varying the mole ratios of precursors, reaction time and reaction temperature.
- To investigate the effect of the sequence of precursor addition on the properties of AuSe.
- To investigate the structural and surface properties of AuSe when using various capping agents.
- To investigate the electrocatalytic properties of AuSe for potential use as a counter electrode in DSSCs.

References

[1] R. Prăvălie, C. Patriche, G. Bandoc, Journal of Cleaner Production, 209 (2019) 692-721.

[2] T. Dhansay, C. Musekiwa, T. Ntholi, L. Chevallier, D. Cole, M.J. de Wit, South African Journal of Science, 113 (2017) 1-7.

[3] I.M. Bugaje, Renewable and Sustainable Energy Reviews, 10 (2006) 603-612.

[4] A. Pegels, Energy Policy, 38 (2010) 4945-4954.

[5] http://aidc.org.za/renewable-energy-south-africa-electricity-power-plants/ Date cited: 23 July 2019

[6] S. Jain, P.K. Jain, Energy Procedia, 143 (2017) 721-726.

[7] J. Wu, Z. Lan, J. Lin, M. Huang, Y. Huang, L. Fan, G. Luo, Chemical Reviews, 115 (2015) 2136-2173.

[8] T. Zhang, M. Wang, H. Yang, Energies, 11 (2018).

[9] J. Gong, K. Sumathy, Q. Qiao, Z. Zhou, Renewable and Sustainable Energy Reviews, 68 (2017) 234-246.

[10] B. O'Regan, M. Grätzel, Nature, 353 (1991) 737-740.

[11] M. Ye, X. Wen, M. Wang, J. Iocozzia, N. Zhang, C. Lin, Z. Lin, Materials Today, 18 (2015) 155-162.

[12] F. Bella, C. Gerbaldi, C. Barolo, M. Grätzel, Chemical Society reviews, 44 (2015) 3431-3473.
[13] S. Mathew, A. Yella, P. Gao, R. Humphry-Baker, B.F.E. Curchod, N. Ashari-Astani, I. Tavernelli, U. Rothlisberger, M.K. Nazeeruddin, M. Grätzel, Nature Chemistry, 6 (2014) 242.
[14] M.A. Green, K. Emery, Y. Hishikawa, W. Warta, E.D. Dunlop, Progress in Photovoltaics: Research and Applications, 23 (2015) 1-9.
[15] E. Olsen, G. Hagen, S. Eric Lindquist, Solar Energy Materials and Solar Cells, 63 (2000) 267-273.
[16] http://www.usfunds.com/investor-library/frank-talk/top-10-gold-producing countries/#.XTcbFegzbIV Date cited: 23 July 2019
[17] https://www.bizcommunity.com/Article/196/693/141073.html Date cited: 23 July 2019

Chapter 2

Literature review

1. Introduction to 2D-layered materials

1.1 The case of graphene

For many years most research on dimensionality controlled synthesis was focused on zero-dimensional (0D) nanospheres and one-dimensional (1D) materials such as nanorods and nanowires [1-3]. However, since the discovery of two-dimensional (2D) single layered graphene [4], there has been a complete paradigm shift and a growing interest in other 2D-layered materials.

Graphene is a single layer (atomically thin) material consisting of sp^2-hybridised carbon atoms covalently bonded and arranged in a honeycomb lattice [5]. It is a building block for the other dimensional carbon allotropes, i.e. it can be wrapped up into 0D fullerenes, rolled into 1D nanotubes or stacked into 3D graphite [6] as shown in Fig. 1.

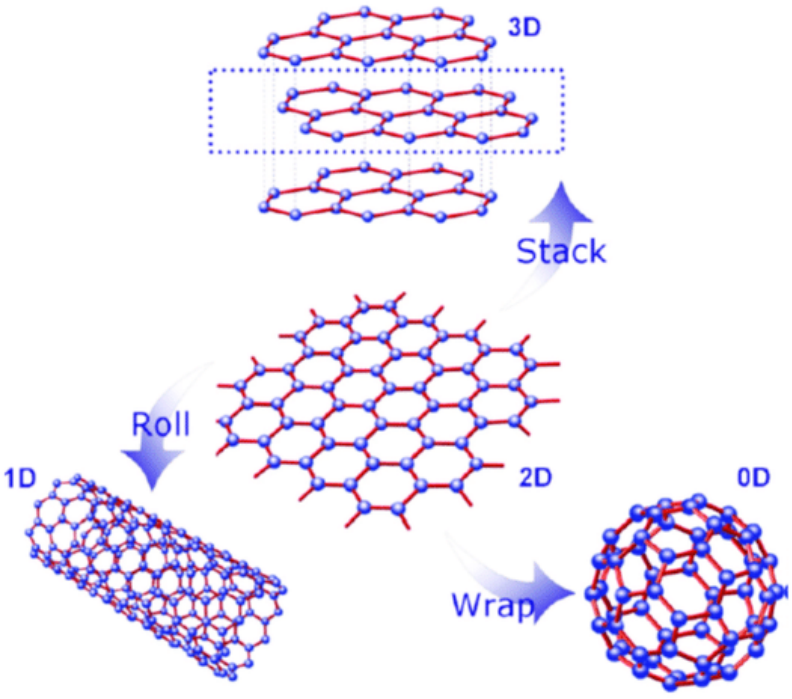

Fig. 1: Graphene, the building block for other dimensionalities of carbon allotropes [7].

The electronic properties of graphene are of a unique nature. It is a zero-bandgap material, that is, the conduction band and the valence band in pristine graphene meet at a single point around which the wave functions of electrons are described by the Dirac equation [6]. Its band structure, seen in Fig. 2, shows band-overlap in two conical points (K and K′) in the Brillouin zone [8]. The charge carriers in this structure, known as mass-less Dirac fermions, are electrons losing their rest mass, m_0 and can best be described by (2 + 1)-dimensional Dirac equations [9-11]. Due to its exceptionally unique electronic, thermal and mechanical properties, it has provided fertile ground for numerous applications such as ballistic transistors, field emitter, components of integrated circuits, transparent conducting electrodes and sensors [9, 12]. Graphene exhibits high thermal conductivity of 3 000 $W.m^{-1}K^{-1}$, almost ten times that of copper [13, 14]. It has a high optical transparency of 97.7% in the visible and IR spectra making it an excellent candidate for solar cell applications [15, 16].

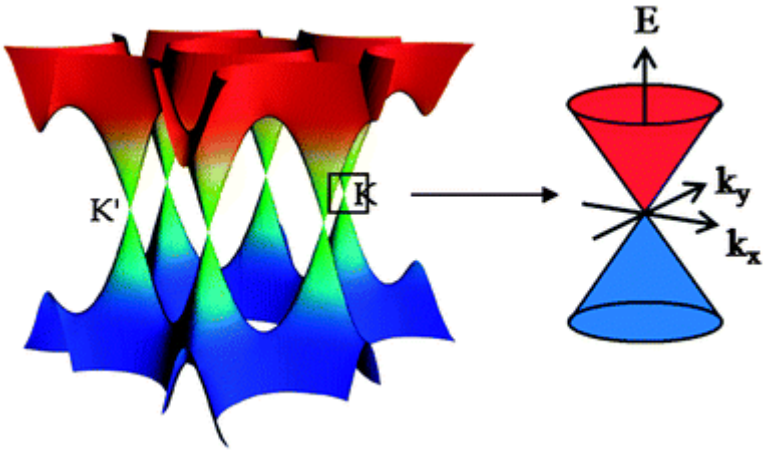

Fig. 2: Electronic band structure of single layer graphene [8].

Graphene has for many years been used in various kinds of solar cell devices for different purposes. In 2008, Wu *et al.* demonstrated that solution-processed graphene thin films could serve as transparent conductive anodes for organic photovoltaic cells [17]. Graphene layers have also been used as transparent top electrodes and electron collecting layers in perovskite solar cells [18, 19]. Graphene films have been employed as hole transport electrode in copper indium gallium sulfide (CIGS) solar cells [20] and graphene quantum dots investigated for down conversion effect in quantum dot sensitized solar cells [21]. Of interest is the use of graphene materials in dye-sensitized solar cells (DSSCs). Their initial application in DSSCs was as a transparent electrode to replace fluorine doped tin oxide (FTO) at the photoanode and

the device showed an overall power conversion efficiency (PCE) of 0.26% [22]. With this outcome, other properties such as light harvesting abilities, enhancing ion transport through both the TiO_2 layer and the electrolyte, and replacing platinum at the cathode have since been investigated [23-27]. It was when Kavan *et al.* reported a PCE of 9.40% using graphene nanoplates as the counter electrode in DSSC that the true potential of 2D-layered materials as a platinum replacement was realized [28].

1.2 2D-layered materials beyond graphene

Over the years, the impressive surge in research and development on other 2D materials has drastically increased as indicated by the number of reports per year in Fig. 3 [29]. Fig. 4 shows a table by Geim and Grigorieva giving a summary on discoveries of the different types of 2D materials colour coded according to their stabilities under various conditions [30]. Monolayers that are stable under ambient conditions are shaded blue; those stable in air are shaded green; and those unstable in air but may show some stability in an inert atmosphere are shaded pink. Grey shading indicates 3D compounds that have been successfully exfoliated down to monolayers, but for which there is little further information. This library includes among many others, transition metal chalcogenides (e.g. molybdenum disulfide (MoS_2), molybdenum diselenide ($MoSe_2$), tungsten disulfide (WS_2), and tungsten diselenide (WSe_2)), hexagonal boron nitride (h-BN), borophene (2D boron), MXenes (2D carbides/nitrides) and black phosphorous [31-37].

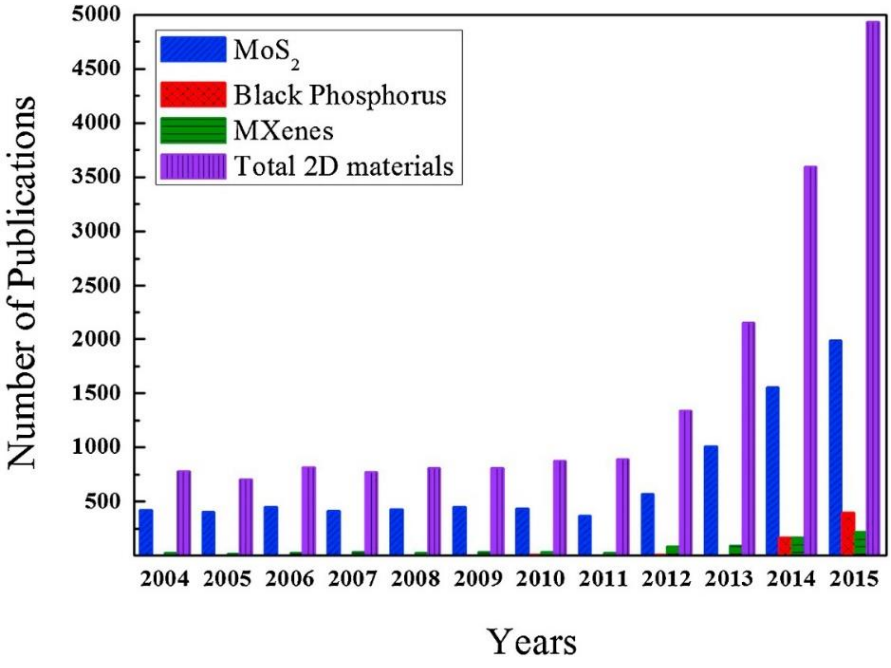

Fig. 3: Year-wise publication plots for 2D materials including MoS_2, $MoSe_2$, black phosphorus, MXenes, and total 2D transition metal chalcogenides from 2005–2016 [29].

<table>
<tr><td>Graphene family</td><td>Graphene</td><td colspan="2">hBN
'white graphene'</td><td>BCN</td><td>Fluorographene</td><td>Graphene oxide</td></tr>
<tr><td rowspan="2">2D chalcogenides</td><td colspan="2" rowspan="2">MoS_2, WS_2,$MoSe_2$, WSe_2</td><td colspan="2" rowspan="2">Semiconducting dichalcogenides:
$MoTe_2$, WTe_2,
ZrS_2, $ZrSe_2$, and so on</td><td colspan="2">Metallic dichalcogenides:
$NbSe_2$, NbS_2, TaS_2, TiS_2, $NiSe_2$ and so on</td></tr>
<tr><td colspan="2">Layered semiconductors:
GaSe, GaTe, InSe, Bi_2Se_3 and so on</td></tr>
<tr><td rowspan="2">2D oxides</td><td>Micas, BSCCO</td><td colspan="2">MoO_3, WO_3</td><td rowspan="2" colspan="2">Perovskite-type:
$LaNb_2O_7$, $(Ca,Sr)_2Nb_3O_{10}$,
$Bi_4Ti_3O_{12}$,$Ca_2Ta_2TiO_{10}$ and so on</td><td>Hydroxides: $Ni(OH_2)$, $Eu(OH)_2$ and so on</td></tr>
<tr><td>Layered Cu oxides</td><td colspan="2">TiO_2, MnO_2, V_2O_2,
TaO_2, RuO_2 and so on</td><td>Others</td></tr>
</table>

Fig. 4: Summary of 2D library as at 2013 [30].

1.2.1 Transition metal chalcogenides

Many of these 2D materials are derivatives from bulk 3D materials which commonly crystalize in a layered structure. For transition metal chalcogenides, each layer is described as a composition of metal atoms sandwiched between two layers of chalcogen atoms where the intralayer bonding is due to strong in-plane covalent bonding. These layers are then held together by weak van der Waals interactions which can be easily cleaved during mechanical exfoliation to produce monolayers, bilayers or even few layered 2D materials [38-41]. Fig. 5 is a crystal structure diagram of layered transition metal chalcogenide MoS_2 which aims to pictorially describe the points mentioned above.

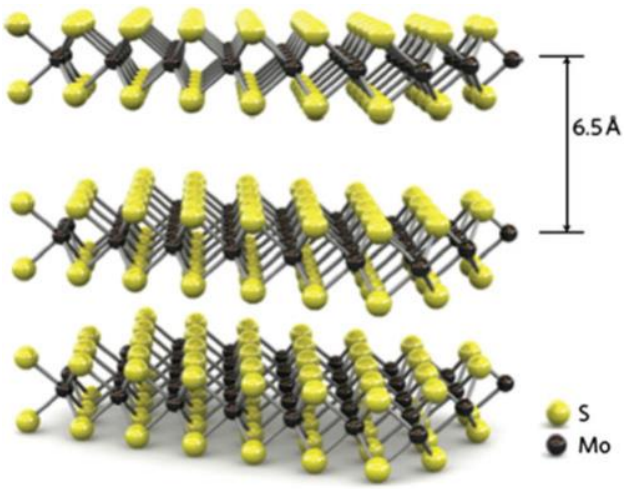

Fig. 5: Crystalline structure of layered MoS_2 where the Mo atom is sandwiched between the S atoms and the distance between two layers is 6.5 Å [41].

Some of the favourable qualities of these so-called "exotic" 2D materials include; being atomically thin which affords them high transparency [42] and good mechanical flexibility giving them the ability to be deposited onto flexible substrates as well as to survive the stress and strain compliance of flexible supports [43, 44]. They have large surface area-to-volume ratios and of particular interest are their electrical and optical properties as a result of downsizing from their 3D bulk counterparts, causing a dimensionality confinement effect and modulation in their band structure [45-47]. One such interesting example is that of MoS_2, when its band structure changes from the bulk to the atomically thinned monolayer. Shown in Fig. 6 is the band structure of MoS_2 where the dashed red lines indicate the Fermi level, the top valence band is indicated in blue, the lowest-energy conduction band in green and the arrows indicate the fundamental band gap (direct or indirect) for a given system.

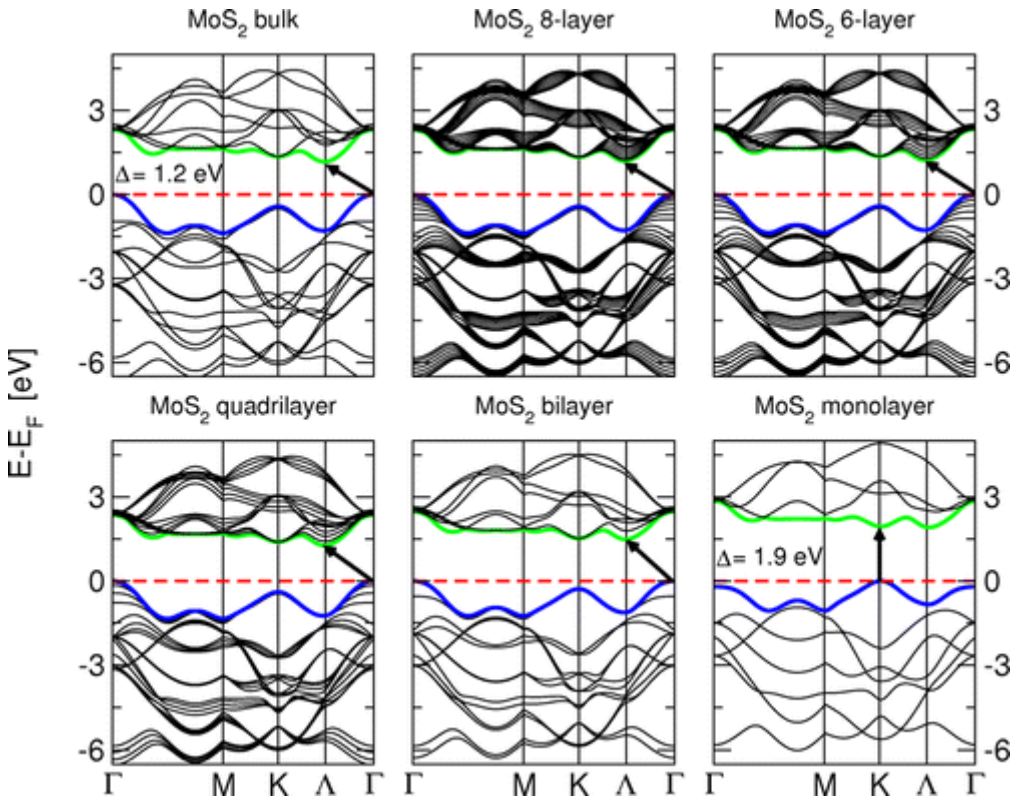

Fig. 6: Band structure of MoS_2 in bulk, multilayer, bilayer, and monolayer forms [48].

In its bulk form, MoS_2, has an indirect band gap with an electron transition between the Γ and a point located halfway between K and Γ, known as the Λ point. All other multi-layered structures also exhibit this indirect band gap trait although the valence band valley at the Γ

point decreases and the conduction band valley at the Λ point increases. An intriguing turn is when the material reaches monolayer state, the valence band maximum (VBM) point and the conduction band minimum (CBM) point are both located at the K point, leading to a direct band gap semiconductor [48, 49]. All these attractive properties offer 2D-layered materials as perfect candidates for applications such as chemical and gas sensing, supercapacitance for energy storage, as superconductors, as catalyst supports and in photovoltaics to name a few [50-53]. However, with the evolving technology market, there is need to develop novel materials with excellent properties to take this sector to new heights. The field of 2D-layered materials is far from being fully explored, for there are ample materials which are still to be discovered and thoroughly investigated.

1.2.2 Gold selenide (AuSe), a 2D-layered material

Gold selenide (AuSe) is another potential 2D material that crystalizes in a layered structure. This material is relatively unexplored but has promising semiconductor properties. AuSe exists in two phases; α-AuSe known to be the metastable phase and β-AuSe the thermodynamically stable form [54, 55]. Fig. 7 illustrates the layered crystal structures of the two phases of AuSe. The two polymorphs can easily be distinguished by their most intense XRD reflections, (003) for α-AuSe and (111) for β-AuSe. Gold selenide crystallizes in the space group C2/m with lattice parameters, a=12.202(2) and 8.355(2) Å, b=3.690(7) and 3.663(1) Å and c=8.433(2) and 6.262(1) Å for α-AuSe and β-AuSe, respectively [56]. Both polymorphs contain Au^{1+} and Au^{3+} ions. The Au^{1+} ion is coordinated linearly to two Se atoms whilst Au^{3+} is surrounded by four Se atoms in square planar geometry as seen in images of the zoomed in crystal structures in Fig. 8.

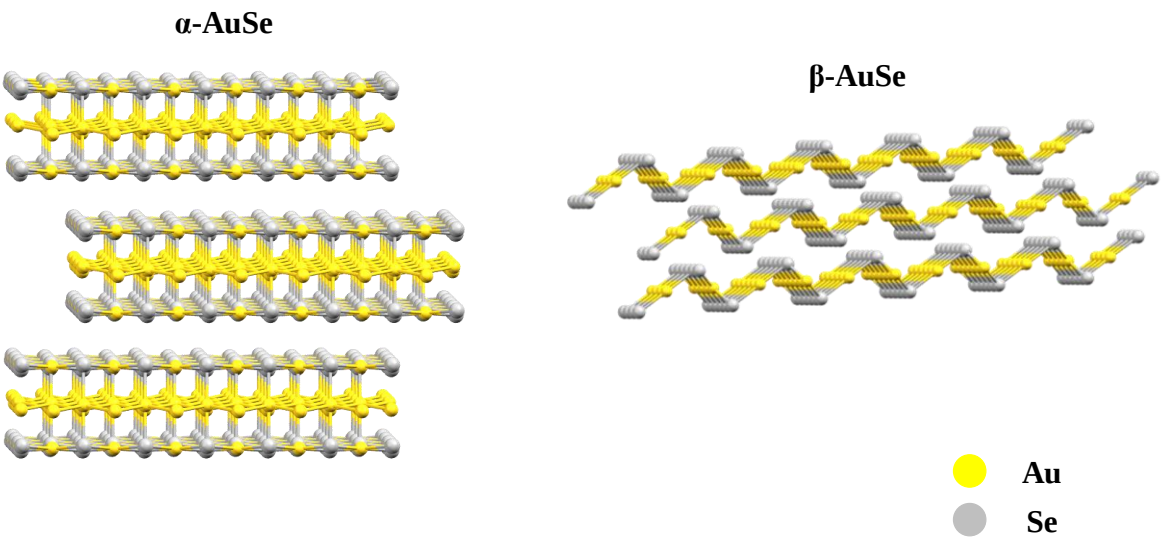

Fig. 7: Crystal structure of layered α-AuSe and β-AuSe.

Its complex structure due to its mixed valent and polymorphic nature could be the reason this striking material has for so many years been ignored, understudied and not well reported. Needless to say, for the very few reports we've found in our literature search, its electronic structure has been of much controversy. From the chemical formula "AuSe", one would assume that Au is in a valency state of II whereas in fact there are two types of Au ions in the system; one with valence I and the other III. However, X-ray absorption spectroscopy (XAS) and X-ray photoelectron spectroscopy (XPS) experiments have failed on numerous accounts to display this mixed valency [57, 58]. Nevertheless, Wagner *et al*. confirmed this detail using ^{197}Au Mössbauer studies of gold selenide [59]. With very little knowledge on other properties of gold selenide, the AuSe nanoalloys' optical properties studies, opened up a new scope for experimentation in photoelectric, semiconducting and catalytic applications for this material [60].

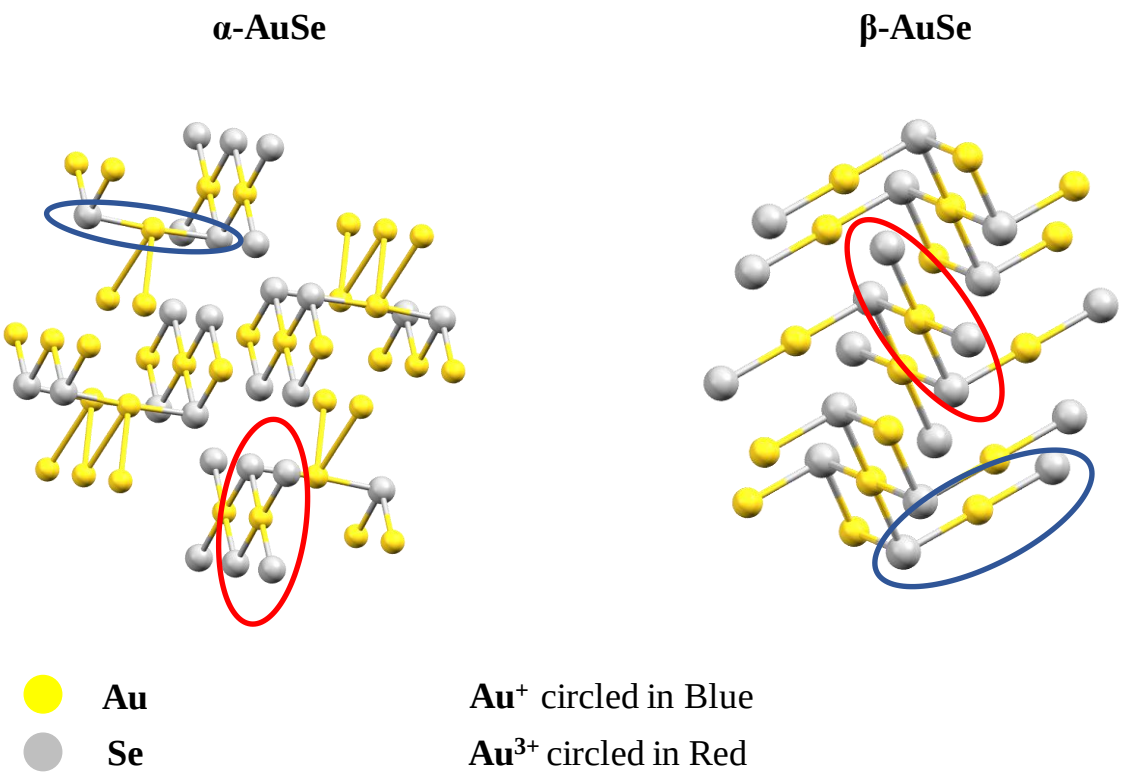

Fig. 8. Crystal structures of both α-AuSe and β-AuSe indicating the presence of the different gold sites (Au^{+} and Au^{3+}).

It's only very recently that the electronic properties of AuSe have been determined. Two independent groups performed and reported theoretical calculations on 2D monolayer β-AuSe for the first time in July 2019. *Gong et al.* reported an indirect band gap of 1.66 eV for the monolayer and 1.28 eV for the bilayer. The band structures are shown in Fig. 9 [61]. These results were corroborated by investigations performed by Bai *et al.* which reported the monolayer indirect band gap of 2.0 eV. The absorption spectrum of the material was also simulated, the results are shown in Fig. 10 together with the band structure [62]. Monolayer β-AuSe absorbed stronger in the deep ultra-violet (UV) region below 200 nm, which the authors suggest that future application of the material could be in C-type deep-UV (below 240 nm) optoelectronic devices like some III-borides including AlN (aluminium nitride) and (boron nitride) BN. Both groups mention that the material shows superior dynamic and thermodynamic stability, moreover, it has a high carrier mobility and a strong light absorption coefficient giving β-AuSe excellent properties for application in field-effect transistors and solar cells.

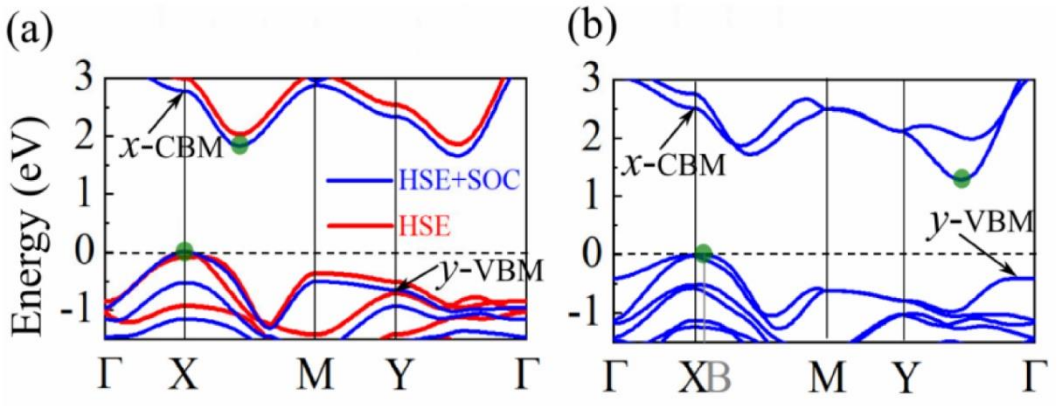

Fig. 9: Band structures of (a) monolayer and (b) bilayer β-AuSe. Note that x-CBM (y - VBM) denotes the CBM (VBM) along the x (y) direction. Green solid balls indicate the global VBM (valence band maximum) or CBM (conduction band minimum) [61].

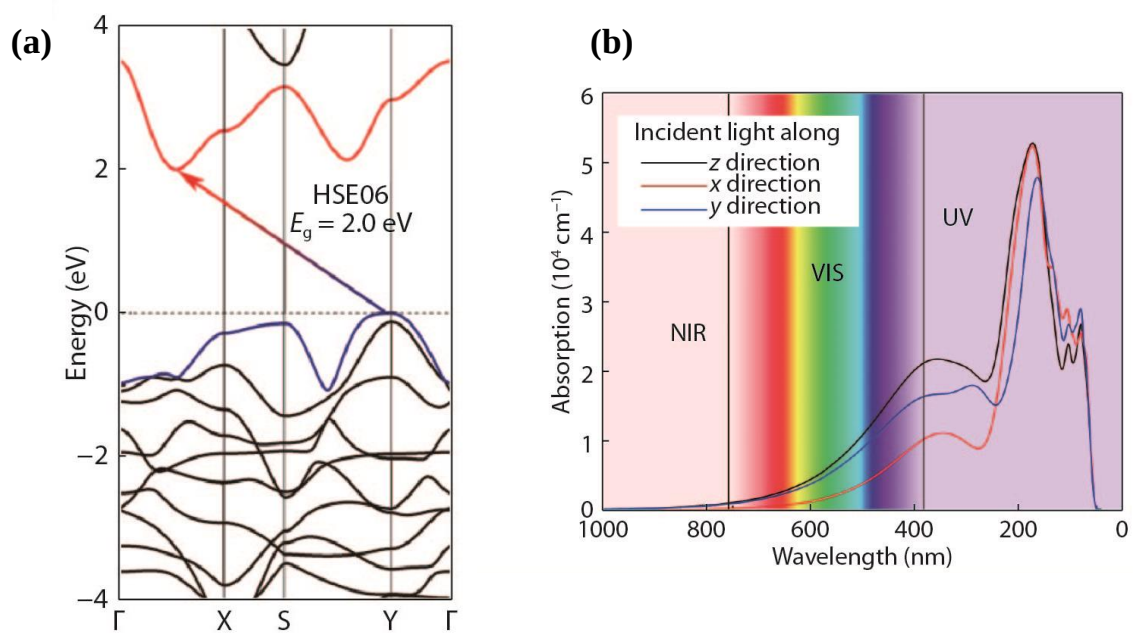

Fig. 10: (a) Computational band structure of β-AuSe monolayer and (b) simulated absorption spectra of AuSe monolayer [62].

2. Synthesis of 2D-layered materials

2.1 New 2D heterostructures

A new field of study focusing on heterostructures is currently emerging and is gaining tremendous interest and momentum [63]. It deals with devices made up by stacking different layers of different types of 2D materials on top of each other, resulting in an entirely "new material" with undoubtedly improved electronic and photonic properties. For example,

simulations predicted that stacked monolayers of MoS_2 and WSe_2 would exhibit a heterostructure with a new direct band gap of 0.6 eV [64, 65], such heterogeneous stacking significantly reduces the bandgap energy. The simple stacking phenomenon is explained at length by Geim and Grigorieva making an analogy to building with Lego blocks, with one block defined as one atomically thin layer of a specific 2D material and the van der Waals interactions are still at play, holding the multi-layered stack in place [30]. Shown in Fig. 11 is the heterostructure analogy to Lego building blocks presented. This idea of van der Waals heterostructures reinforces the notion of developing new 2D-layered materials and ultimately finding simpler ways of mass production.

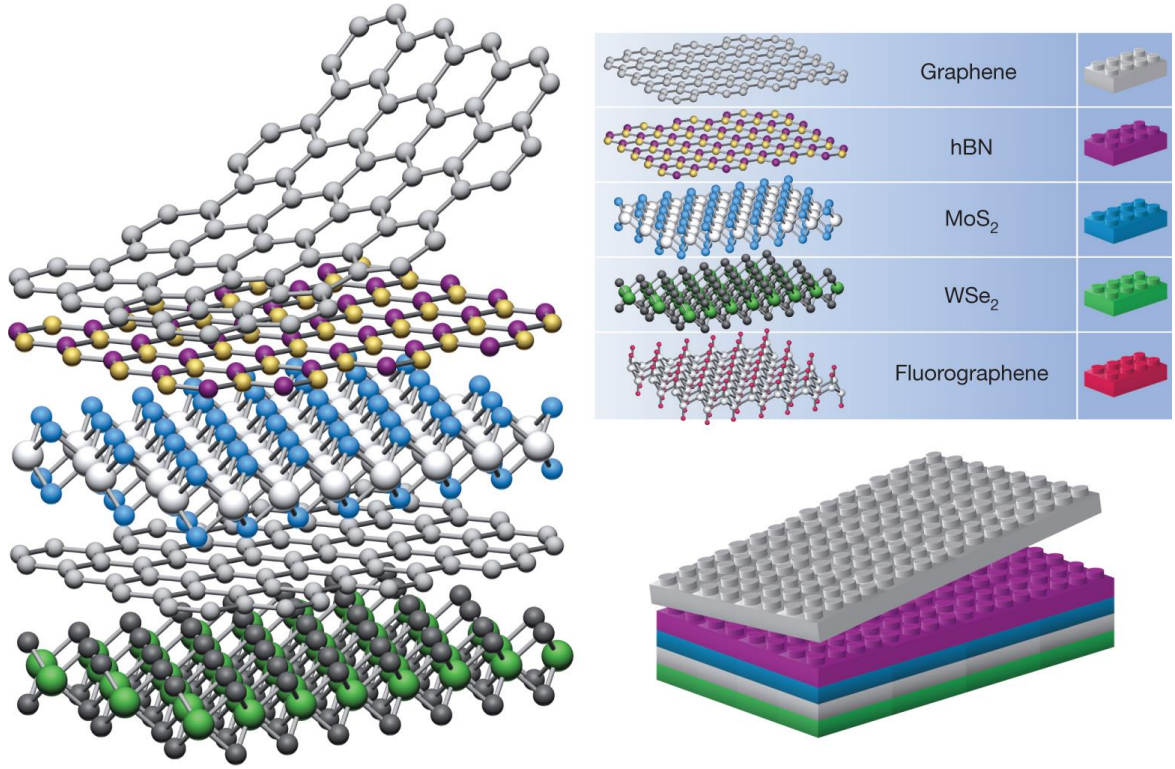

Fig. 11: Building van der Waals heterostructures. If one considers 2D crystals to be analogous to Lego blocks (right panel), the construction of a huge variety of layered structures becomes possible [30].

2.2 Top down methods

To afford these atomically thin 2D materials, generally there are two routes that can be explored; the top-down method and the bottom-up method. Top down methods involve taking the 3D layered structure and breaking it down into its 2D derivatives. These include the micro-mechanical and the liquid exfoliation techniques. Mechanical exfoliation simply uses adhesive

Scotch tape to peel off either one layer or few layers from the 3D bulk crystals. This is then followed by bringing the freshly cleaved thin layers still on the Scotch tape into contact with the target substrate, they are then rubbed or pressed off using tools such as plastic tweezers to assist in placing them onto the substrate [66-68]. This process poses advantages such as simplicity and reliability, where it is devoid of any chemical procedures and costly equipment, [69], Fig. 12 is the illustration. Liquid exfoliation is a process whereby the bulk 3D layered materials are ultra-sonicated in a solvent, breaking the weak van Waals interactions and giving the desired 2D monolayer materials [70-72]. Fig. 13 gives an animation of this simple process and also shows two possible outcomes that could be due to solvent choice. With a poor solvent, reaggregation might occur whereas a good solvent results in nanosheets formation with appropriate surface energies and are therefore stabilized against reaggregation. One of the biggest drawbacks of these top-down methods is scalability of the 2D materials.

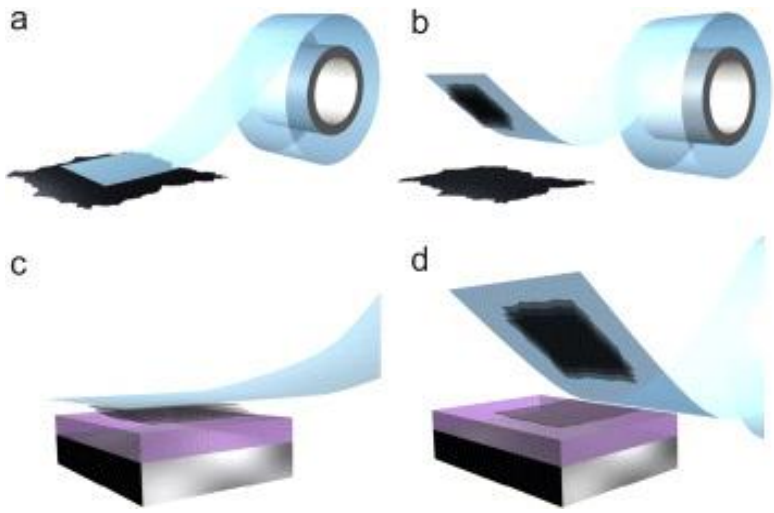

Fig. 12: Illustration of micro-mechanical exfoliation of 2D nanostructures. (a) Adhesive tape is pressed against a 3D crystal material so that the top few layers are attached to the tape (b). (c) The tape with crystals of layered material is pressed against the surface of a target substrate. (d) Upon peeling off, the bottom layer is left on the substrate [68].

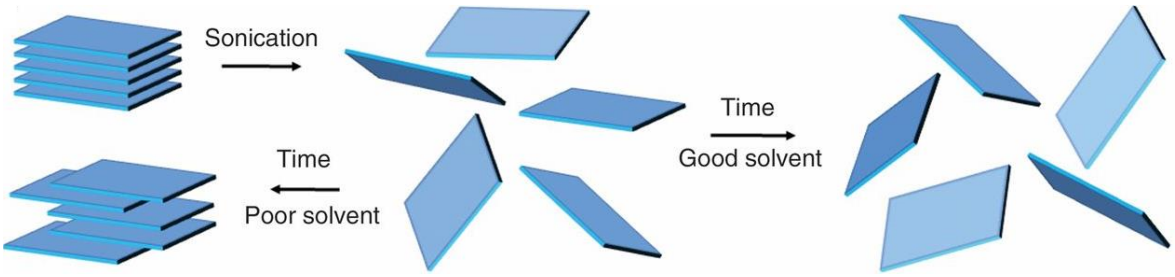

Fig. 13: Liquid exfoliation technique using chemical ultrasonication [72].

2.3 Bottom up methods

The bottom up methods involve synthesis of these 2D materials from the elemental constituents into their monolayer form. This includes techniques such as the chemical vapour deposition (CVD) method and one pot colloidal synthesis. For the CVD approach, catalytically active substrates are most effective. Generally, the synthesis can be performed at pressures ranging from atmospheric to ultra-high vacuum and at elevated temperatures. Growth of the 2D materials occurs when the substrate is heated enough to activate sublimation or diffusion processes of the precursors, producing a surface layer enriched with the precursor vapour that ultimately condenses forming the desired 2D materials [73-76]. Fig. 14 illustrates the CVD synthesis technique. Although there has been great success in using the CVD method, limitations such as size precision and difficulty to control the number of layers have been a concern [77].

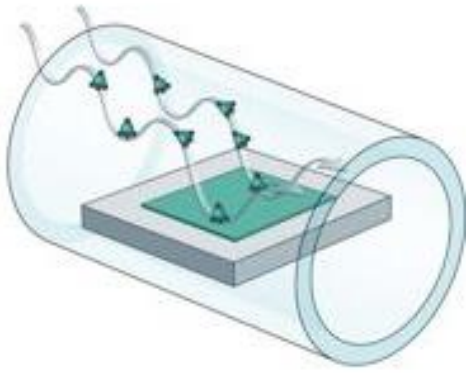

Fig. 14: Chemical vapour deposition (CVD) technique [75].

Solution-based colloidal synthesis gives the advantage of controlling the composition, size and morphology of the desired 2D materials [78]. The use of solvents or capping agents with this method, can be selectively chosen together with changing and adjusting reaction parameters

such as time and temperature, skilfully manipulating the nucleation and growth processes. These processes are best described by the LaMer and Dinegar mechanism of colloid formation shown in Fig. 15 [79]. This mechanism describes precursors dissolved or dispersed in a solvent, chemically reacting to form monomers. With time, as the concentration of monomers increase to the supersaturation level, these aggregate and self-nucleation occurs. The growth process of the pre-existing nuclei continues until the concentration of the monomers is below a critical level, slowing and ultimately terminating growth of the nanocrystal [80]. The anisotropic growth of 2D layered materials is mainly attributed to the surface energy difference between edge and planar facets [81]. The nanocrystals grow in the direction of facets with high surface energy, due to the growth rate being exponentially correlated to surface energy [82]. This bottom up approach produces high quality atomically thin 2D materials in appreciable yields. In addition, colloidal synthesis does not make use of harsh conditions such as elevated temperatures, high pressures, high-end expensive equipment but rather uses simple benchtop laboratory apparatus which makes production economical [83-85]. Taking into account all these added advantages, the selected method of synthesis for AuSe 2D-layered materials was thus the colloidal synthetic method.

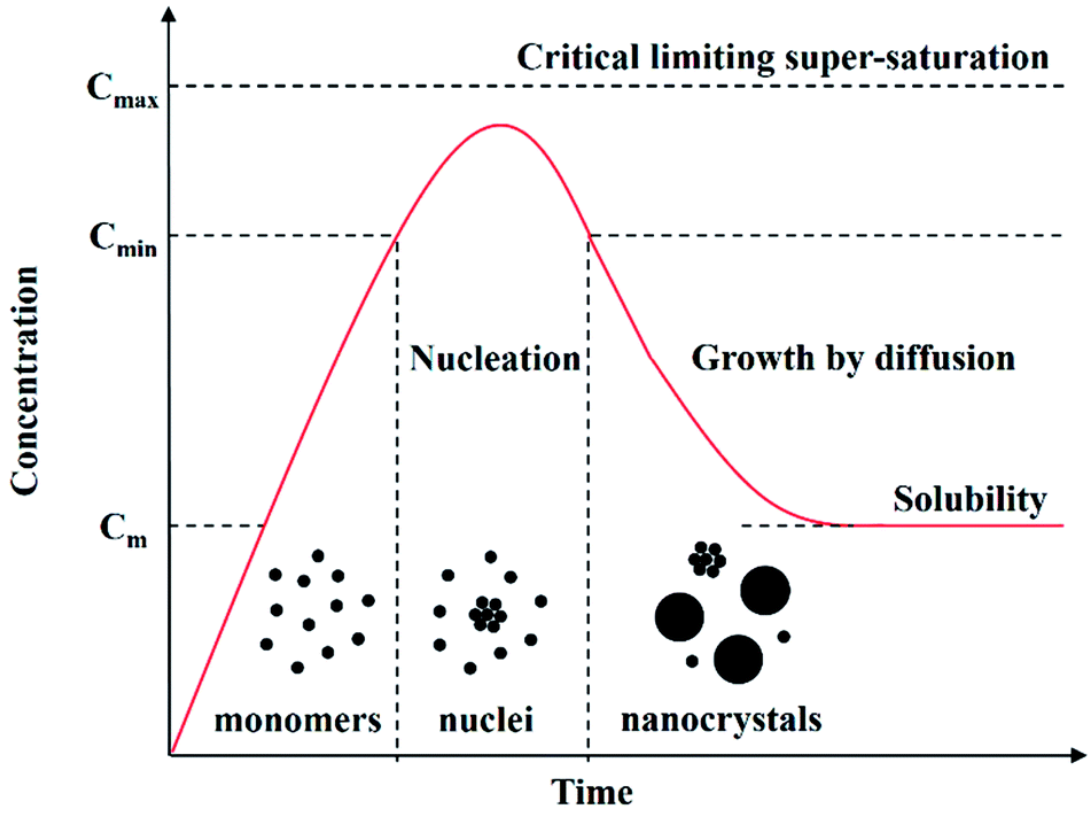

Fig. 15: Nucleation and growth process of nanocrystals in solution as described by LaMer and Dinegar [80].

2.3.1 Factors affecting colloidal 2D-layered materials

Various factors can influence the outcome, nature and properties of the synthesized materials. These generally include reaction parameters such as temperature, time (duration of the synthesis), type of precursors used and their respective amounts, solvents or capping agents etc. Below, is a brief description of a few influencing factors and their impact; take for example colloidal synthesis of single-layer and multi-layer MoS_2 reported by Zhou *et al.* [86]. They were able to exclusively manipulate the anisotropic growth of the material by changing the precursor ratio of Mo to S and tuned the lateral size of the single-layer MoS_2 in a range of 8 to 25 nm, while the number of MoS_2 layers, consisting of 1, 3, 5 and 7 layers was influenced by a multi-injection approach. The layer-dependence of the materials were revealed by Raman spectroscopy which showed that with an increase in the number of layers, the frequencies of Raman modes gradually shifted to the values of bulk MoS_2. Fig. 16 is an illustration of the influence of precursor ratio and multi-injection approach in MoS_2 synthesis.

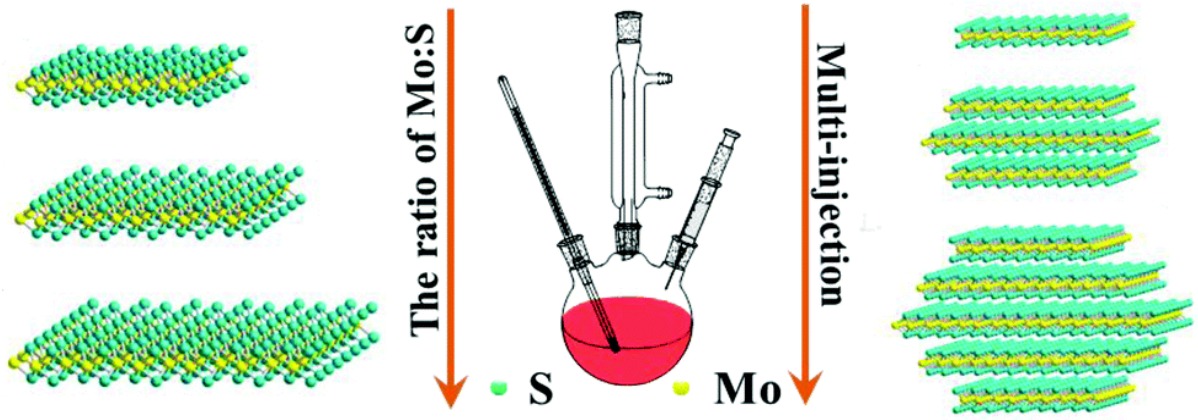

Fig. 16: Schematic illustration of the effect of change in precursor ratio and the multi-injection method on single- and multi-layer MoS_2 nanosheets [86].

An interesting phenomenon is the effect due to alterations in the sequence of precursor addition. Previously, Ntholeng *et al*. showed that the order in which the precursors were added afforded formation of pure $CuInTe_2$, thus showing the positive influence of this parameter change in order to eliminate impurities [87]. Capping/stabilizing agents are known to be the biggest contributors of morphology control. These stabilizers are normally large organic molecules with functional groups having different affinities to specific chemical environments. This affinity leads them to preferentially bind to certain crystal facets on the nanostructure, producing structures with distinct shapes [88]. For example, ligands having shorter chain

lengths result in more branched nanostructures while those with longer chains allow for growth in the lateral direction [89]. In this study we present the effects of, precursor ratios (i.e. Au: Se), temperature, the sequence of precursor addition as well as capping agents on the colloidal synthesis of AuSe.

3. Applications of 2D-layered materials

Two-dimensional layered materials have very interesting properties which make them find use in a variety of applications such as for energy storage, catalysis [90-92] and photovoltaics [93-96] to name just a few as shown in Fig. 17.

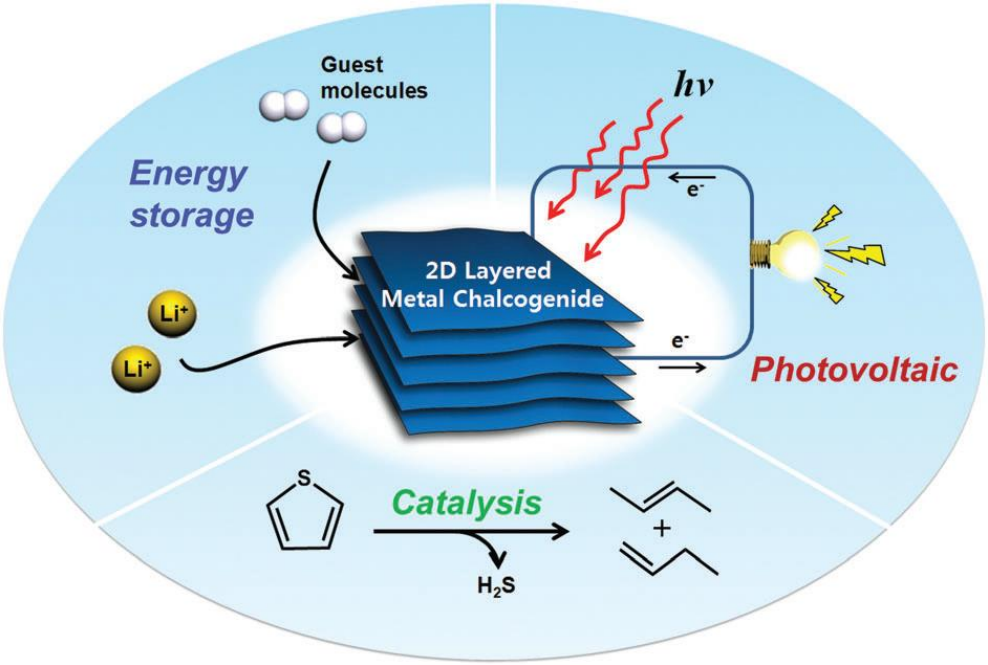

Fig. 17: Schematic representation showing the types of technologies 2D-layered materials can be applied in [81].

Many of these 2D-layered materials as a result of their large surface area and high sensitivity to light, are excellent candidates for solar cell applications. Much has been achieved on harnessing solar energy and researchers continually seek materials to improve on the current technologies to fully exploit this abundant, sustainable and renewable resource. Harnessing of solar energy has gone through generational progressive stages starting from the 1st generation of solar cells (based on single crystalline silicon) to the 2nd generation which are thin film processed to currently, the 3rd generation solar cells which showcase competitive PCEs to the other generations. Amongst many types in the 3rd generation, are the dye-sensitized solar cells (DSSCs) [97-99]. Due to their promising PCEs, environmental friendliness and their simple

fabrication process which make them cost-effective, DSSC and its derivatives have been the most preferred and intensely researched of late [100].

3.1 Dye-sensitized solar cells

The most recent report presented a 13% power conversion efficiency in DSSC technology [101], although this is a promising value, it is still lacking from the 26% reported for the current silicon-based solar cells in the market [102]. Numerous studies are under way that aim to improve on this, and this involves carefully investigating the properties of the DSSCs constituents/components and making alterations where necessary. First assembled and demonstrated in 1991 [103], a dye-sensitized solar cell consists of five components namely; the conducting glass substrate, the semiconductor, the dye (sensitizer), the electrolyte and the counter electrode. This multicomponent set-up gives an advantage of making selective changes on individual components to be independently investigated. Depicted in Fig. 18 is a schematic that illustrates the operating principle of DSSCs, and the subsequent paragraph details this process.

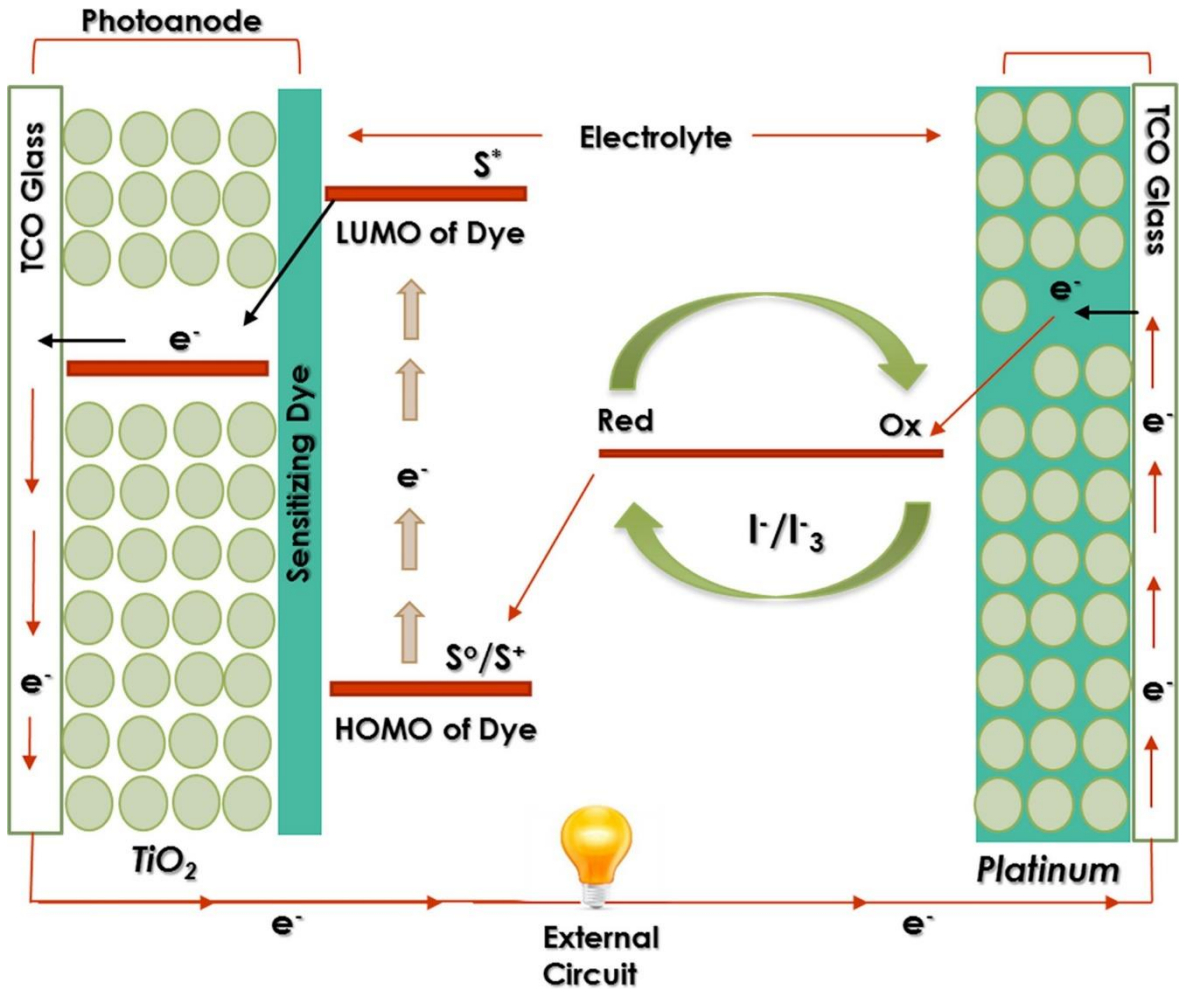

Fig. 18: Schematic illustrating the working principle of a DSSC [104].

Upon illumination by visible light, the dye absorbs energy (photon energy) and gets oxidized. The excited electrons move from the dye's valence band to its conduction band. With the correct alignment in energy levels (dye conduction band higher in energy than semiconductor conduction band), these electrons then flow into the conduction band of the semiconductor and finally to the external circuit via the conducting substrate (either fluorine doped tin oxide (FTO) or indium doped tin oxide (ITO)). This constant flow of electrons generates current to power-up electrical appliances. The counter electrode (CE) then receives electrons from the external circuit which ultimately move toward the dye through the electrolyte. By receiving electrons, the dye gets reduced and is regenerated to its original state [104-106].

3.1.1 Photoanode

There have been several comprehensive studies investigating the different DSSC components such as the photoanode which is responsible for the conversion of photons into electrical energy

and consists of the conducting glass substrate, semiconductor and dye. These reports have looked at possibilities of using alternative fabrication methods for TiO_2 that avoid the use of high annealing temperatures however still maintaining the properties, and replacement of TiO_2 (or ZnO) with other high surface area materials with wide band gaps [107, 108]. The high surface area of the semiconductor allows for high loading of the dye molecules, thereby affording improved efficiencies of the devices [109]. A number of dyes have also been investigated from naturally occurring molecules extracted from certain plant components [110, 111] to chemically synthesized organic dyes some of which incorporate ruthenium metal in the complex [112-114].

3.2.2 Electrolyte

The electrolyte is responsible for the inner carrier charge transfer between the photoanode and cathode while continuously regenerating the dye and itself during DSSC operation. Different electrolytes have also been researched, where suggestions to use alternatives such as polysulfide rather than an iodine-based electrolyte, or use of solids instead of liquid electrolytes have been proposed [98, 115-117].

3.2.3 Counter electrodes

The counter electrode is a key component which assists in the regeneration of the dye by reducing triiodide ions during redox electrocatalytic activity occurring in the electrolyte. To date, platinum metal (Pt) has been used and this is due to its metallic nature and willingness to donate electrons, however, it is susceptible to corrosion by the commonly used liquid iodide-triiodide (I^-/I_3^-) electrolyte as a result of PtI_4 formation [118, 119]. Materials with a high surface area could serve as excellent CE as this allows for faster redox activity. Efforts to find alternatives as CE replacements have been made and materials such as different carbonaceous materials, carbon-metal composites, polymers and inorganic materials such as metal oxides and high surface area 2D-layered transition metal chalcogenides have been duly explored [104, 120 - 122]. Recent reports with promising PCEs on 2D-layered materials as counter electrodes include but are not limited to; graphene (PCE = 6.23%) [123], composite $WS_2/MoTe_2$ (7.99%) [124], MoS_2 (8.4 %) [125], $NbSe_2$ nanosheets (7.34%), $NbSe_2$ nanorods (6.78%) [126], FeSe (7.64%) [127], $FeSe_2$ nanosheets (8.39%) [128], $CoSe_2$ (6.60%) and $NiSe_2$ (7.60%) [129] and titanium disulphide nanosheets assembled and decorated on graphene, TiS_2-G (8.80%) [121].

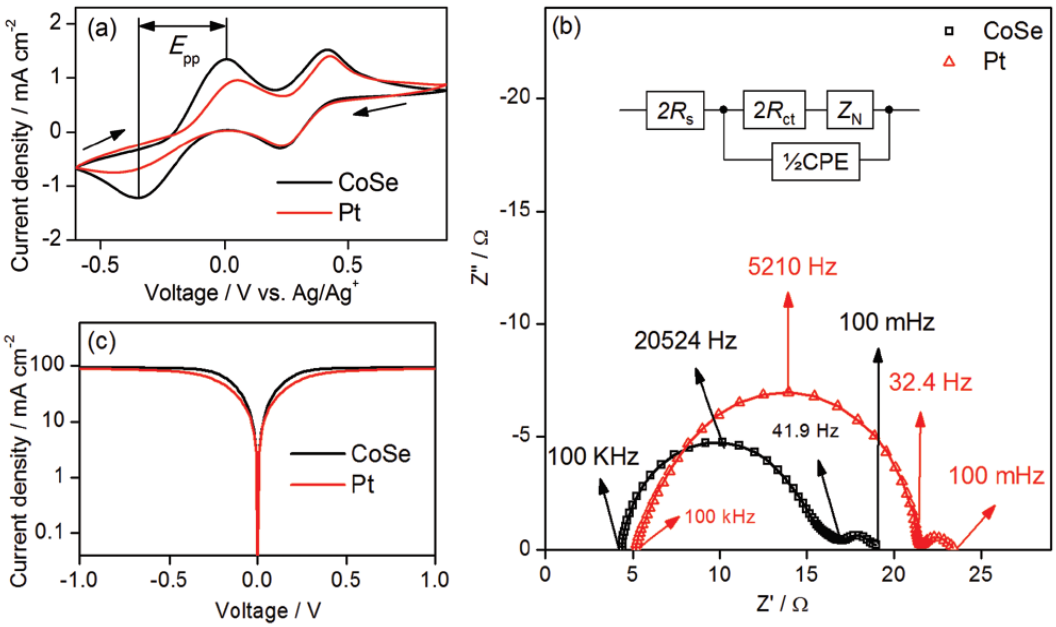

Fig. 19: (a) CV curves, (b) EIS Nyquist plots and (c) Tafel curves [131].

To measure the catalytic activity of a material, electrochemical characterization techniques can be employed such as cyclic voltammetry (CV) and impedance spectroscopy. CV is an important technique that helps to evaluate the electrocatalytic activity of the counter electrode in the (I^-/I_3^-) electrolyte. Fig. 19 gives an example of typical cyclic voltammograms by counter electrode materials. In the redox couple, the reduction of the I_3^- ions is the most significant aspect in the operation of a DSSC. The reduction reaction with the equation $I_3^- + 2e^- \rightarrow I^-$ is characterized by the negative current cathodic peak and the oxidation with equation $I^- \rightarrow I_3^- + 2e^-$, is associated with the positive current anodic peak and the change in the peak potential is known as the peak-to-peak separation, ΔEpp. The cathodic peak gives information about the reduction velocity whereas the ΔEpp gives information about the reversibility of the redox reaction. The smaller the ΔEpp, the better the reversibility [130].

The electrical conductivity of the CE is often investigated using electrochemical impedance spectroscopy (EIS) using symmetric cells where the Nyquist plot and Tafel polarization curve can be obtained. A typical example of a Nyquist plot is shown in Fig. 19. The high frequency region of the Nyquist plot provides information about the series resistance (Rs), the charge transfer resistance at the electrode/electrolyte interface (Rct) and the double layer capacitance (Cm), while the information about the Nernst diffusion impedance (ZN) of the redox couple in

the electrolyte is obtained from the low frequency regime. These values are determined by fitting an equivalent circuit. The Tafel polarization curve (shown in Fig. 19) gives information regarding the exchange current density (J_o) which is dependent on the charge carrier resistance (Rct) and is given by the following equation:

$$J_O = RT/nFRct$$

Where R is the gas constant, T is the temperature, n is the number of electrons involved in the reduction of triiodide to iodide [130-132].

References

[1] D. Bera, L. Qian, T.-K. Tseng, P.H. Holloway, Materials, 3 (2010).

[2] Y. Xia, P. Yang, Y. Sun, Y. Wu, B. Mayers, B. Gates, Y. Yin, F. Kim, H. Yan, Advanced Materials, 15 (2003) 353-389.

[3] T. Zhai, L. Li, Y. Ma, M. Liao, X. Wang, X. Fang, J. Yao, Y. Bando, D. Golberg, Chemical Society reviews, 40 (2011) 2986-3004.

[4] K.S. Novoselov, A.K. Geim, S.V. Morozov, D. Jiang, Y. Zhang, S.V. Dubonos, I.V. Grigorieva, A.A. Firsov, Science, 306 (2004) 666.

[5] Y. Zhu, S. Murali, W. Cai, X. Li, J.W. Suk, J.R. Potts, R.S. Ruoff, Advanced Materials, 22 (2010) 3906-3924.

[6] A.K. Geim, K.S. Novoselov, The rise of graphene, in: Nanoscience and Technology, Co-Published with Macmillan Publishers Ltd, UK, 2009, pp. 11-19.

[7] X. Wan, Y. Huang, Y. Chen, Accounts of Chemical Research, 45 (2012) 598-607.

[8] C.N.R. Rao, K. Biswas, K.S. Subrahmanyam, A. Govindaraj, Journal of Materials Chemistry, 19 (2009) 2457-2469.

[9] W. Choi, I. Lahiri, R. Seelaboyina, Y.S. Kang, Critical Reviews in Solid State and Materials Sciences, 35 (2010) 52-71.

[10] A.H. Castro Neto, F. Guinea, N.M.R. Peres, K.S. Novoselov, A.K. Geim, Reviews of Modern Physics, 81 (2009) 109-162.

[11] J. Hass, W.A. de Heer, E.H. Conrad, Journal of Physics: Condensed Matter, 20 (2008) 323202.

[12] Y. Bleu, F. Bourquard, T. Tite, A.-S. Loir, C. Maddi, C. Donnet, F. Garrelie, Front Chem, 6 (2018) 572-572.

[13] A.A. Balandin, Nature Materials, 10 (2011) 569.

[14] A.A. Balandin, S. Ghosh, W. Bao, I. Calizo, D. Teweldebrhan, F. Miao, C.N. Lau, Nano Letters, 8 (2008) 902-907.
[15] F. Bonaccorso, L. Colombo, G. Yu, M. Stoller, V. Tozzini, A.C. Ferrari, R.S. Ruoff, V. Pellegrini, Science, 347 (2015) 1246501.
[16] R.R. Nair, P. Blake, A.N. Grigorenko, K.S. Novoselov, T.J. Booth, T. Stauber, N.M.R. Peres, A.K. Geim, Science, 320 (2008) 1308.
[17] J. Wu, H.A. Becerril, Z. Bao, Z. Liu, Y. Chen, P. Peumans, Applied Physics Letters, 92 (2008) 263302.
[18] P. You, Z. Liu, Q. Tai, S. Liu, F. Yan, Advanced Materials, 27 (2015) 3632-3638.
[19] M. Batmunkh, C.J. Shearer, M.J. Biggs, J.G. Shapter, Journal of Materials Chemistry A, 4 (2016) 2605-2616.
[20] J.-K. Sim, S. Kang, R. Nandi, J.-Y. Jo, K.-U. Jeong, C.-R. Lee, Solar Energy, 162 (2018) 357-363.
[21] H. Teymourinia, M. Salavati-Niasari, O. Amiri, M. Farangi, Journal of Molecular Liquids, 251 (2018) 267-272.
[22] X. Wang, L. Zhi, K. Müllen, Nano Letters, 8 (2008) 323-327.
[23] X. Yan, X. Cui, B. Li, L.-s. Li, Nano Letters, 10 (2010) 1869-1873.
[24] T. Chen, W. Hu, J. Song, G.H. Guai, C.M. Li, Advanced Functional Materials, 22 (2012) 5245-5250.
[25] Y.H. Ng, I.V. Lightcap, K. Goodwin, M. Matsumura, P.V. Kamat, The Journal of Physical Chemistry Letters, 1 (2010) 2222-2227.
[26] P. Zhu, A.S. Nair, P. Shengjie, Y. Shengyuan, S. Ramakrishna, ACS Applied Materials & Interfaces, 4 (2012) 581-585.
[27] J.D. Roy-Mayhew, D.J. Bozym, C. Punckt, I.A. Aksay, ACS Nano, 4 (2010) 6203-6211.
[28] L. Kavan, J.-H. Yum, M. Grätzel, Nano Letters, 11 (2011) 5501-5506.
[29] W. Choi, N. Choudhary, G.H. Han, J. Park, D. Akinwande, Y.H. Lee, Materials Today, 20 (2017) 116-130.
[30] A.K. Geim, I.V. Grigorieva, Nature, 499 (2013) 419.
[31] S.-Y. Chen, C. Zheng, M.S. Fuhrer, J. Yan, Nano Letters, 15 (2015) 2526-2532.
[32] J.C. Shaw, H. Zhou, Y. Chen, N.O. Weiss, Y. Liu, Y. Huang, X. Duan, Nano Research, 7 (2014) 511-517.
[33] W. Zhao, Z. Ghorannevis, L. Chu, M. Toh, C. Kloc, P.-H. Tan, G. Eda, ACS Nano, 7 (2013) 791-797.

[34] M. Chhowalla, H.S. Shin, G. Eda, L.-J. Li, K.P. Loh, H. Zhang, Nature Chemistry, 5 (2013) 263.
[35] A.J. Mannix, X.-F. Zhou, B. Kiraly, J.D. Wood, D. Alducin, B.D. Myers, X. Liu, B.L. Fisher, U. Santiago, J.R. Guest, M.J. Yacaman, A. Ponce, A.R. Oganov, M.C. Hersam, N.P. Guisinger, Science, 350 (2015) 1513.
[36] B. Anasori, Y. Xie, M. Beidaghi, J. Lu, B.C. Hosler, L. Hultman, P.R.C. Kent, Y. Gogotsi, M.W. Barsoum, ACS Nano, 9 (2015) 9507-9516.
[37] F. Xia, H. Wang, Y. Jia, Nature Communications, 5 (2014) 4458.
[38] C. Xie, C. Mak, X. Tao, F. Yan, Advanced Functional Materials, 27 (2017) 1603886.
[39] M.-Y. Li, C.-H. Chen, Y. Shi, L.-J. Li, Materials Today, 19 (2016) 322-335.
[40] S. Das, M. Kim, J.-w. Lee, W. Choi, Critical Reviews in Solid State and Materials Sciences, 39 (2014) 231-252.
[41] A.B. Kaul, Journal of Materials Research, 29 (2014) 348-361.
[42] M. Buscema, J.O. Island, D.J. Groenendijk, S.I. Blanter, G.A. Steele, H.S.J. van der Zant, A. Castellanos-Gomez, Chemical Society reviews, 44 (2015) 3691-3718.
[43] D. Akinwande, N. Petrone, J. Hone, Nature Communications, 5 (2014) 5678.
[44] R. Cheng, S. Jiang, Y. Chen, Y. Liu, N. Weiss, H.-C. Cheng, H. Wu, Y. Huang, X. Duan, Nature Communications, 5 (2014) 5143.
[45] A. Gupta, T. Sakthivel, S. Seal, Progress in Materials Science, 73 (2015) 44-126.
[46] Y. Shi, H. Li, L.-J. Li, Chemical Society reviews, 44 (2015) 2744-2756.
[47] R. Mas-Balleste, C. Gomez-Navarro, J. Gomez-Herrero, F. Zamora, Nanoscale, 3 (2011) 20-30.
[48] A. Kuc, N. Zibouche, T. Heine, Physical Review B, 83 (2011) 245213.
[49] T. Heine, Accounts of Chemical Research, 48 (2015) 65-72.
[50] S. Das, J.A. Robinson, M. Dubey, H. Terrones, M. Terrones, Annual Review of Materials Research, 45 (2015) 1-27.
[51] K.S. Kumar, N. Choudhary, Y. Jung, J. Thomas, ACS Energy Letters, 3 (2018) 482-495.
[52] M. Pumera, A.H. Loo, TrAC Trends in Analytical Chemistry, 61 (2014) 49-53.
[53] A. Kumar, Q. Xu, ChemNanoMat, 4 (2017) 28-40.
[54] G.E. Cranton, R.D. Heyding, Canadian Journal of Chemistry, 46 (1968) 2637-2640.
[55] A. Rabenau, H. Rau, G. Rosenstein, Journal of the Less Common Metals, 24 (1971) 291-299.
[56] A. Rabenau, H. Schulz, Journal of the Less Common Metals, 48 (1976) 89-101.
[57] A.R.H.F. Ettema, T.A. Stegink, C. Haas, Solid State Communications, 90 (1994) 211-213.

[58] S. Vorobyev, M. Likhatski, A. Romanchenko, N. Maksimov, S. Zharkov, A. Krylov, Y. Mikhlin, Minerals, 8 (2018).
[59] F.E. Wagner, P. Palade, J. Friedl, G. Filoti, N. Wang, Journal of Physics: Conference Series, 217 (2010) 012039.
[60] S. Nath, S.K. Ghosh, T. Pal, Chemical Communications, (2004) 966-967.
[61] P.-L. Gong, F. Zhang, L. Li, B. Deng, H. Pan, L.-F. Huang, X.-Q. Shi, Journal of Physics: Condensed Matter, 31 (2019) 395501.
[62] P. Bai, S. Guo, S. Zhang, H. Qu, W. Zhou, H. Zeng, Journal of Semiconductors, 40 (2019) 062004.
[63] K.S. Novoselov, A. Mishchenko, A. Carvalho, A.H. Castro Neto, Science, 353 (2016) aac9439.
[64] R. Lv, J.A. Robinson, R.E. Schaak, D. Sun, Y. Sun, T.E. Mallouk, M. Terrones, Accounts of Chemical Research, 48 (2015) 56-64.
[65] H. Fang, C. Battaglia, C. Carraro, S. Nemsak, B. Ozdol, J.S. Kang, H.A. Bechtel, S.B. Desai, F. Kronast, A.A. Unal, G. Conti, C. Conlon, G.K. Palsson, M.C. Martin, A.M. Minor, C.S. Fadley, E. Yablonovitch, R. Maboudian, A. Javey, Proceedings of the National Academy of Sciences, 111 (2014) 6198.
[66] H. Li, J. Wu, Z. Yin, H. Zhang, Accounts of Chemical Research, 47 (2014) 1067-1075.
[67] H. Li, G. Lu, Y. Wang, Z. Yin, C. Cong, Q. He, L. Wang, F. Ding, T. Yu, H. Zhang, Small, 9 (2012) 1974-1981.
[68] K.S. Novoselov, A.H. Castro Neto, Physica Scripta, T146 (2012) 014006.
[69] Y. Chen, G. Jiang, S. Chen, Z. Guo, X. Yu, C. Zhao, H. Zhang, Q. Bao, S. Wen, D. Tang, D. Fan, Opt. Express, 23 (2015) 12823-12833.
[70] S. Chae, J.A. Siddiqa, S. Oh, J.B. Kim, H.K. Choi, W.-S. Jang, Y.-M. Kim, K.H. Yu, J.-Y. Choi, Nanomaterials, 8 (2018).
[71] J.N. Coleman, M. Lotya, A. O'Neill, S.D. Bergin, P.J. King, U. Khan, K. Young, A. Gaucher, S. De, R.J. Smith, I.V. Shvets, S.K. Arora, G. Stanton, H.-Y. Kim, K. Lee, G.T. Kim, G.S. Duesberg, T. Hallam, J.J. Boland, J.J. Wang, J.F. Donegan, J.C. Grunlan, G. Moriarty, A. Shmeliov, R.J. Nicholls, J.M. Perkins, E.M. Grieveson, K. Theuwissen, D.W. McComb, P.D. Nellist, V. Nicolosi, Science, 331 (2011) 568.
[72] V. Nicolosi, M. Chhowalla, M.G. Kanatzidis, M.S. Strano, J.N. Coleman, Science, 340 (2013) 1226419.
[73] Y.-H. Lee, X.-Q. Zhang, W. Zhang, M.-T. Chang, C.-T. Lin, K.-D. Chang, Y.-C. Yu, J.T.-W. Wang, C.-S. Chang, L.-J. Li, T.-W. Lin, Advanced Materials, 24 (2012) 2320-2325.

[74] J. Xia, X. Huang, L.-Z. Liu, M. Wang, L. Wang, B. Huang, D.-D. Zhu, J.-J. Li, C.-Z. Gu, X.-M. Meng, Nanoscale, 6 (2014) 8949-8955.
[75] A.J. Mannix, B. Kiraly, M.C. Hersam, N.P. Guisinger, Nature Reviews Chemistry, 1 (2017) 0014.
[76] G. Ye, Y. Gong, S. Lei, Y. He, B. Li, X. Zhang, Z. Jin, L. Dong, J. Lou, R. Vajtai, W. Zhou, P.M. Ajayan, Nano Research, 10 (2017) 2386-2394.
[77] G. Su, V.G. Hadjiev, P.E. Loya, J. Zhang, S. Lei, S. Maharjan, P. Dong, P. M. Ajayan, J. Lou, H. Peng, Nano Letters, 15 (2015) 506-513.
[78] S. Jeong, D. Yoo, J.-t. Jang, M. Kim, J. Cheon, Journal of the American Chemical Society, 134 (2012) 18233-18236.
[79] V.K. LaMer, R.H. Dinegar, Journal of the American Chemical Society, 72 (1950) 4847-4854.
[80] J. Chang, E.R. Waclawik, RSC Advances, 4 (2014) 23505-23527.
[81] J.H. Han, S. Lee, J. Cheon, Chemical Society reviews, 42 (2013) 2581-2591.
[82] Y.-w. Jun, J.-s. Choi, J. Cheon, Angewandte Chemie International Edition, 45 (2006) 3414-3439.
[83] M.-R. Gao, Y.-F. Xu, J. Jiang, S.-H. Yu, Chemical Society reviews, 42 (2013) 2986-3017.
[84] S. Huang, V.N. Mochalin, Inorganic Chemistry, 58 (2019) 1958-1966.
[85] J.S. Son, J.H. Yu, S.G. Kwon, J. Lee, J. Joo, T. Hyeon, Advanced Materials, 23 (2011) 3214-3219.
[86] M. Zhou, Z. Zhang, K. Huang, Z. Shi, R. Xie, W. Yang, Nanoscale, 8 (2016) 15262-15272.
[87] N. Ntholeng, B. Mojela, S. Gqoba, M. Airo, S. Govindraju, M.J. Moloto, J. Van Wyk, N. Moloto, New Journal of Chemistry, 40 (2016) 10259-10266.
[88] M.S. Bakshi, Crystal Growth & Design, 16 (2016) 1104-1133.
[89] M. Green, Journal of Materials Chemistry, 20 (2010) 5797-5809.
[90] B. Anasori, M.R. Lukatskaya, Y. Gogotsi, Nature Reviews Materials, 2 (2017) 16098.
[91] X. Zhang, L. Hou, A. Ciesielski, P. Samorì, Advanced Energy Materials, 6 (2016) 1600671.
[92] Y. Zhu, L. Peng, Z. Fang, C. Yan, X. Zhang, G. Yu, Advanced Materials, 30 (2018) 1706347.
[93] M. Bernardi, M. Palummo, J.C. Grossman, Nano Letters, 13 (2013) 3664-3670.
[94] S.J. McDonnell, R.M. Wallace, Thin Solid Films, 616 (2016) 482-501.

[95] Y. Tsuboi, F. Wang, D. Kozawa, K. Funahashi, S. Mouri, Y. Miyauchi, T. Takenobu, K. Matsuda, Nanoscale, 7 (2015) 14476-14482.
[96] S. Lei, A. Sobhani, F. Wen, A. George, Q. Wang, Y. Huang, P. Dong, B. Li, S. Najmaei, J. Bellah, G. Gupta, A.D. Mohite, L. Ge, J. Lou, N.J. Halas, R. Vajtai, P. Ajayan, Advanced Materials, 26 (2014) 7666-7672.
[97] T. Zhang, M. Wang, H. Yang, Energies, 11 (2018).
[98] J. Wu, Z. Lan, J. Lin, M. Huang, Y. Huang, L. Fan, G. Luo, Chemical Reviews, 115 (2015) 2136-2173.
[99] W.A. Badawy, Journal of Advanced Research, 6 (2015) 123-132.
[100] J. Gong, K. Sumathy, Q. Qiao, Z. Zhou, Renewable and Sustainable Energy Reviews, 68 (2017) 234-246.
[101] S. Mathew, A. Yella, P. Gao, R. Humphry-Baker, B.F.E. Curchod, N. Ashari-Astani, I. Tavernelli, U. Rothlisberger, M.K. Nazeeruddin, M. Grätzel, Nature Chemistry, 6 (2014) 242.
[102] M.A. Green, K. Emery, Y. Hishikawa, W. Warta, E.D. Dunlop, Progress in Photovoltaics: Research and Applications, 23 (2015) 1-9.
[103] B. O'Regan, M. Grätzel, Nature, 353 (1991) 737-740.
[104] U. Ahmed, M. Alizadeh, N.A. Rahim, S. Shahabuddin, M.S. Ahmed, A.K. Pandey, Solar Energy, 174 (2018) 1097-1125.
[105] Y. Cao, Y. Liu, S.M. Zakeeruddin, A. Hagfeldt, M. Grätzel, Joule, 2 (2018) 1108-1117.
[106] F. Bella, C. Gerbaldi, C. Barolo, M. Grätzel, Chemical Society reviews, 44 (2015) 3431-3473.
[107] M. Shakeel Ahmad, A.K. Pandey, N. Abd Rahim, Renewable and Sustainable Energy Reviews, 77 (2017) 89-108.
[108] D. Sengupta, P. Das, B. Mondal, K. Mukherjee, Renewable and Sustainable Energy Reviews, 60 (2016) 356-376.
[109] C.C. Raj, R. Prasanth, Journal of Power Sources, 317 (2016) 120-132.
[110] N.A. Ludin, A.M. Al-Alwani Mahmoud, A. Bakar Mohamad, A.A.H. Kadhum, K. Sopian, N.S. Abdul Karim, Renewable and Sustainable Energy Reviews, 31 (2014) 386-396.
[111] G. Richhariya, A. Kumar, P. Tekasakul, B. Gupta, Renewable and Sustainable Energy Reviews, 69 (2017) 705-718.
[112] A. Mahmood, Solar Energy, 123 (2016) 127-144.
[113] C.-Y. Chen, M. Wang, J.-Y. Li, N. Pootrakulchote, L. Alibabaei, C.-h. Ngoc-le, J.-D. Decoppet, J.-H. Tsai, C. Grätzel, C.-G. Wu, S.M. Zakeeruddin, M. Grätzel, ACS Nano, 3 (2009) 3103-3109.

[114] F. Gao, Y. Wang, D. Shi, J. Zhang, M. Wang, X. Jing, R. Humphry-Baker, P. Wang, S.M. Zakeeruddin, M. Grätzel, Journal of the American Chemical Society, 130 (2008) 10720-10728.
[115] M.S. Su'ait, M.Y.A. Rahman, A. Ahmad, Solar Energy, 115 (2015) 452-470.
[116] B. Li, L. Wang, B. Kang, P. Wang, Y. Qiu, Solar Energy Materials and Solar Cells, 90 (2006) 549-573.
[117] Y.-L. Lee, C.-H. Chang, Journal of Power Sources, 185 (2008) 584-588.
[118] S.S. Nemala, P. Kartikay, R.K. Agrawal, P. Bhargava, S. Mallick, S. Bohm, Solar Energy, 169 (2018) 67-74.
[119] E. Olsen, G. Hagen, S. Eric Lindquist, Solar Energy Materials and Solar Cells, 63 (2000) 267-273.
[120] M. Ye, X. Wen, M. Wang, J. Iocozzia, N. Zhang, C. Lin, Z. Lin, Materials Today, 18 (2015) 155-162.
[121] X. Meng, C. Yu, B. Lu, J. Yang, J. Qiu, Nano Energy, 22 (2016) 59-69.
[122] X. Li, J. Bai, B. Zhou, X. Yuan, X. Zhang, L. Liu, Chemistry – A European Journal, 24 (2018) 11444-11450.
[123] S.S. Nemala, P. Kartikay, S. Prathapani, H.L.M. Bohm, P. Bhargava, S. Bohm, S. Mallick, Journal of Colloid and Interface Science, 499 (2017) 9-16.
[124] S. Hussain, S.F. Shaikh, D. Vikraman, R.S. Mane, O.-S. Joo, M. Naushad, J. Jung, RSC Advances, 5 (2015) 103567-103572.
[125] A. Antonelou, G. Syrrokostas, L. Sygellou, G. Leftheriotis, V. Dracopoulos, S.N. Yannopoulos, Nanotechnology, 27 (2015) 045404.
[126] J. Guo, Y. Shi, C. Zhu, L. Wang, N. Wang, T. Ma, Journal of Materials Chemistry A, 1 (2013) 11874-11879.
[127] Y. Duan, Q. Tang, J. Liu, B. He, L. Yu, Angewandte Chemie International Edition, 53 (2014) 14569-14574.
[128] S. Huang, Q. He, W. Chen, J. Zai, Q. Qiao, X. Qian, Nano Energy, 15 (2015) 205-215.
[129] I.A. Ji, H.M. Choi, J.H. Bang, Materials Letters, 123 (2014) 51-54.
[130] Z. Huang, X. Liu, K. Li, D. Li, Y. Luo, H. Li, W. Song, L. Chen, Q. Meng, Electrochemistry Communication, 9 (2007), 596-598.
[131] H. Sun, L. Zhang, G. Zhou, Z-S. Wang, Particle & Particle Systems Characterization, 33, (20160, 729-733.
[132] H.K. Mulmudi, S.K. Batabyal, M. Rao, R.R. Prabhakar, N. Mathews, X.M. Lam, S.G. Mhaisalkar, Physical Chemistry Chemical Physics, 13, (2011), 19307-19309.

Chapter 3

Unravelling the structural properties of mixed-valence α- and β-AuSe nanostructures using XRD, TEM and XPS

Abstract

2D materials have received much attention recently as they can potentially offer new routes to electronics and other technologies. Gold selenide is a relatively unexplored 2D material with a complex mixed-valence crystal structure similar to that of AgO. Apart from 1960s and 1970s reports on the solid-state synthesis and crystal structure respectively, little is known about gold selenide. Herein, we report for the first time, the colloidal synthesis of α- and β-AuSe nanostructures by varying the Au:Se ratio and temperature in order to tailor the properties. We probe the structural properties using XRD, TEM, and XPS. The XRD results confirmed the mixed-valence crystal structure where Au^{1+} and Au^{3+} co-exist in a unit cell, however, there was co-crystallization of both the α- and β-phase. The TEM showed belt-like nanostructures indicative of the 2D-type material. The Au4f core level spectrum of the XPS, showed only the Au^{+1} oxidation state, however, using the Se3d core level spectrum, the formation of AuSe ($Au^{+1}Au^{+3}Se_2$) was evident. The colloidal method, nonetheless, resulted in impurities in a form of unreacted selenium and reduced Au^0 due to the reducing capping agent irrespective of the attempted stoichiometric ratios. In an attempt to minimize the impurities and be selective to a single crystal phase, the temperature was varied from 160 ℃ to 280 ℃. The lower temperature resulted in a single phase of β-AuSe with some unreacted Se. As the temperature was increased, a mixture of α- and β-AuSe, as well as elemental gold, was obtained.

Keywords: gold selenide; nanostructures; mixed valence; structural properties

1. Introduction

Two-dimensional (2D) materials have recently received much attention owing to materials such as graphene, phosphorenes and boron nitride [1-3]. These materials offer routes to new electronics, optoelectronics, and other applications [4, 5]. 2D materials are characterized by a layered crystal structure with strong chemical bonds along one plane and relatively weak Van der Waals forces along the perpendicular plane. This characteristic structure, therefore, makes it possible to produce materials of varying thicknesses [6]. The properties of 2D materials are highly depended on the thickness [7]. Gold selenide is an interesting and unexplored material that possesses a layered crystal structure in bulk form similar to graphite [8]. Gold selenide exists in two forms, namely α- and β-AuSe which both crystallizes in the space group C2/m with lattice parameters, a = 12.202(2) and 8.355(2) Å, b = 3.690(7) and 3.663(1) Å and c = 8.433(2) and 6.262(1) Å respectively [9]. Both crystal phases of AuSe contain Au^{1+} and Au^{3+}. The Au^{1+} is coordinated linearly to two Se atoms whilst Au^{3+} is surrounded by four Se atoms in a square planar geometry as shown in Fig. 1. These essential bonds form infinite rods parallel to the monoclinic b axis in α-AuSe and waved sheets parallel to (100) in β-AuSe. Rods and sheets are connected by weak Au-Au and Se-Se bonds in α-AuSe and by weak Au-Se bonds in β-AuSe [9].

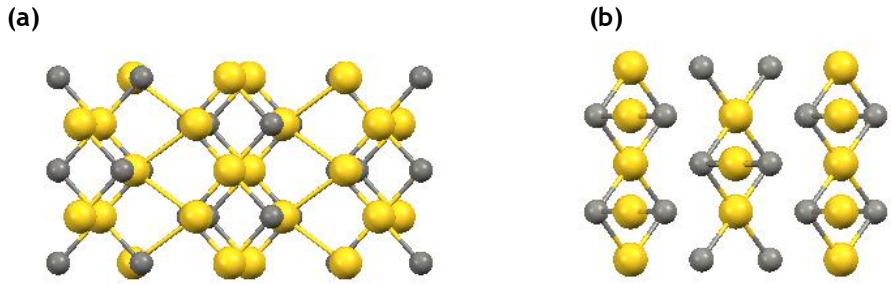

Fig. 1: Crystal structure of (a) α-AuSe and (b) β-AuSe [9].

The layered structure of AuSe, therefore, makes it possible to synthesize 2D nanostructures with tailored thicknesses and properties. Synthesis of 2D nanomaterials from 3D layered structures is often done using a top-down synthetic method such as exfoliation [10]. Exfoliation results in nanosheets with thicknesses as small as one atom thick, however, these nanosheets are often damaged and scaling up on the yield is often difficult [10, 11]. Others have reported on the synthesis of 2D nanomaterials using deposition techniques [12-17]. Deposition techniques often require expensive equipment and operate at harsh reaction conditions such as high temperatures [14]. Colloidal synthesis, a bottom-up approach involves the synthesis of 2D nanomaterials from molecular precursors [6, 7]. Colloidal synthesis uses mild conditions,

inexpensive equipment, and scaling-up is easily achievable [18]. The reaction conditions such as time, temperature, concentration, type of precursors and surfactants can be systematically adjusted thereby allowing for the manipulation of the structure and morphology of the resultant nanomaterials hence resulting in tailored properties [19-22]. Herein, we report for the first time, on the colloidal synthesis and characterization of gold selenide nanomaterials, primarily investigating the effect of gold to selenium precursor ratios as well as different temperatures on the crystal structure and morphology.

2. Experimental

2.1 Chemicals

Gold (III) chloride trihydrate, 99% elemental selenium powder, 70% oleylamine (OLA), toluene and 96% ethanol were obtained from Sigma Aldrich and used without any further processing.

2.2 Synthesis of gold selenide

For the molar ratio studies, a 1:1, 1:3.5 and 1:5 molar ratios of $HAuCl_3.3H_2O$:Se (Au:Se) were studied. In a three neck round bottom flask, under strong magnetic stirring and reflux, 15 mL of OLA was heated to 100 °C followed by the addition of 1 mmol selenium dissolved in 5 mL of OLA, the temperature was further raised to 200 °C and at this point 1 mmol of gold chloride dissolved in 5 mL of OLA was then added. The reaction was carried out at 200 °C; inert conditions were achieved by passing nitrogen gas 20 min before precursor addition and continued until the reaction was terminated. Aliquots were collected every 15 min and they were allowed to cool naturally. Ethanol was then added to flocculate the particles as well was to wash off any impurities. The materials were then collected by centrifugation at 5000 rpm and the products were washed several times and then left to dry at room temperature. For the temperature experiments, the same protocol was followed using 1:3.5 molar ratio of Au:Se and 60 min reaction time however, the temperature was varied to 160 °C and 280 °C.

2.3 Characterization

X-ray diffraction

A Bruker D2 phaser (D2-205530) diffractometer using secondary graphite monochromated CoKα radiation (λ 1.78897 Å) at 30 kV/30 mA was used to measure powder X-ray diffraction (XRD) patterns on the as-synthesized material. Measurements were taken using a glancing

angle of incidence detector at an angle of 2°, for 2θ values over 20 - 110° in steps of 0.026° with a step time of 37 s and at room temperature.

Electron microscopy

Transmission electron microscopy (TEM) was carried out on a FEI Technai T12 TEM microscope operated at an acceleration voltage of 120 kV with a beam spot size of 3 in TEM mode and an EDS detector, operated at 120 kV. The samples were initially suspended in toluene this was followed by placing a drop of the suspended nanomaterials, on a lacey-carbon copper grid.

X-ray photoelectron spectroscopy

X-ray photoelectron spectroscopy (XPS) measurements were performed with a Physical Electronics PHI 5700 spectrometer with a multi-channel hemispherical electron analyzer. Non-monochromatic MgKα X-ray (300 W, 15 kV, 1253.6 eV) was used as excitation source. The spectrometer energy scale was calibrated using Cu 2p3/2, Ag 3d5/2, and Au 4f7/2 photoelectron lines at 932.7, 368.3, and 84.0 eV, respectively. Samples were mounted on a sample holder without adhesive tape and kept overnight at high vacuum in the preparation chamber before being transferred to the analysis chamber for testing. The spectra were collected in the constant pass energy mode at 29.35 eV. The residual pressure in the analysis chamber was maintained below 1.33×10^{-7} Pa during the spectra acquisition.

3. Results and discussion

X-ray diffraction was used to identify the crystal phase and purity of the synthesized materials. Shown in Fig. 2 are the XRD patterns of particles synthesized at 15 min and 60 min using varying amounts of the gold precursor to the selenium precursor. For the 1:1 molar ratio, after 15 min into the reaction, the predominant peaks were those of gold (JCP2.2CA:00-004-0784) with β-AuSe (JCP2.2CA:01-081-2227) peaks showing relatively low intensities. The enhancement of gold selenide peaks relative to those of gold was observed after 60 min. This, therefore, suggests that for a 1:1 reaction, there is an excess of gold. To balance the amount of gold, the amount of selenium was increased to 2 moles, however, this resulted in no change in the XRD pattern. The amount of selenium was therefore further increased giving a molar ratio of 1:3.5 (Au:Se). After 15 min of synthesis, no substantial evidence of the formation of AuSe was observed. For the 60 min sample, both α and β gold selenide were observed with the main peaks (Miller indices) of α-AuSe being at 38.8° (310), 52.2° (-511) and 60.1° (313) using card

number: JCP2.2CA:01-081-2226. The presence of both α and β- AuSe suggests that two crystal growth processes were taking place in the reaction media. Unfortunately, gold impurities were still observed after 60 min, however, the peaks depicted were of relatively low intensity in comparison to those of gold selenide. In order to completely remove the excess gold, the amount of selenium was once again increased. Increasing the amount of selenium to 5 moles, resulted in presence of unreacted selenium as shown in the XRD patterns of both the 15 min and 60 min samples (JCP2.2CA:00-051-1389). Nevertheless, β-AuSe with a trace amount of the α-phase was obtained however impurities of gold were still observed. Cranton *et al.* reported that a gold-rich environment favoured the formation of β-phase while the α-phase was favoured in selenium-rich mixtures [8]. Herein, the β-phase was also obtained at low selenium concentration (1:1) however a mixture of both α and β-AuSe was observed as the concentration of selenium was increased.

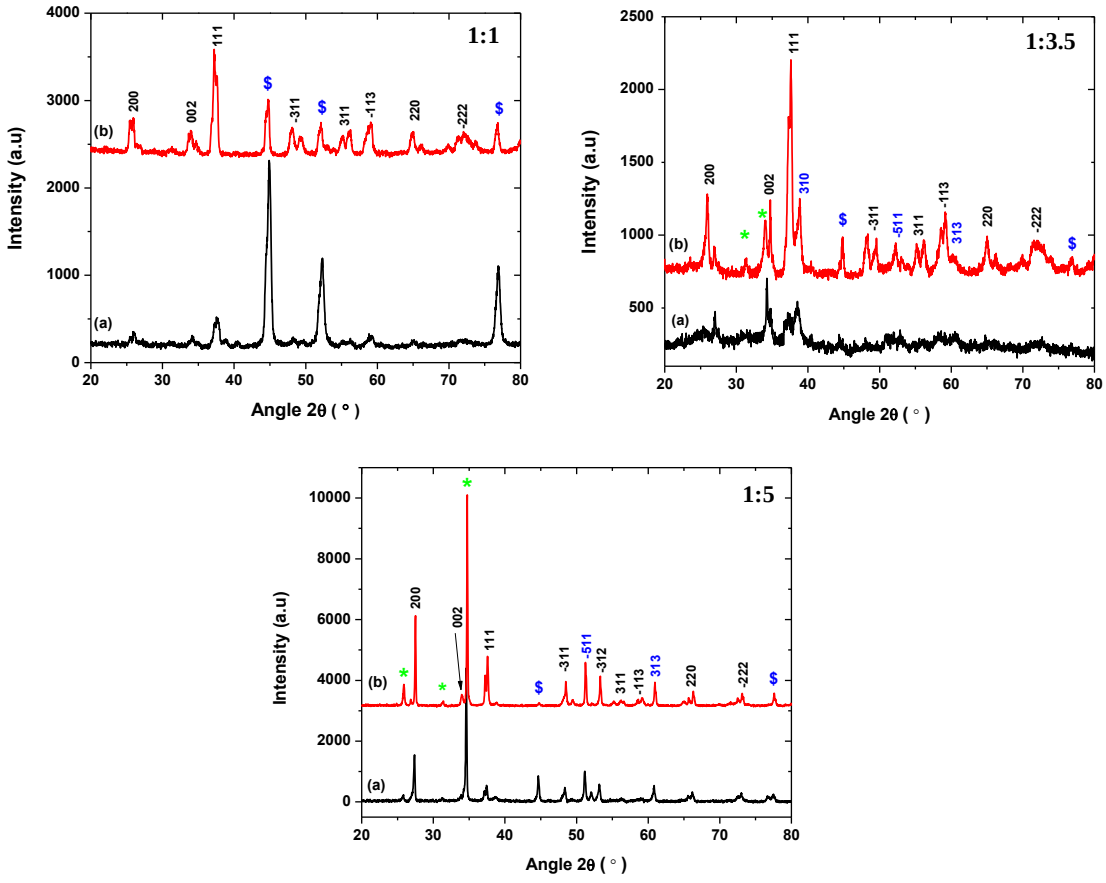

Fig. 2: XRD patterns of material synthesized in (a) 15 min and (b) 60 min for molar ratios 1:1, 1:3.5, and 1:5. ($ denotes gold, * denotes selenium, β-AuSe (black indices) and α-AuSe (blue indices)).

To further investigate the structural properties of the materials, transmission electron microscopy was performed. Fig. 3 shows the micrographs of samples prepared at different molar ratios with aliquots taken at 15 min and 60 min respectively. At 15 min, all ratios showed predominantly fused polydispersed spheres. The fused spheres were identified as selenium nanoparticles (Fig. 1S). These agglomerates were mostly observed in the 1:5 molar ratio, followed by the 1:1 and then to a lesser extent in the 1:3.5 which mostly depicted long, narrow, flexible/bendable and lightly contrasted belt-like structures. Also evident from the 15 min sample of the 1:1 ratio, was the presence of tiny particles on the nanobelts. The belt-like structures were gold selenide nanobelts and were observed again at the 60 min aliquots across all three reactions. These gold selenide nanobelts show very distinct lattice fringes which are indicative of their crystalline nature and this is also corroborated by the intensely sharp peaks in their respective XRD patterns. Moire fringes observed in the 60 min sample of 1:3.5 ratio are due to the overlapping of the nanobelts. As the time was increased to 60 min, less evidence of the fused particles was observed, however, the tiny particles were now also observed in 1:3.5 sample.

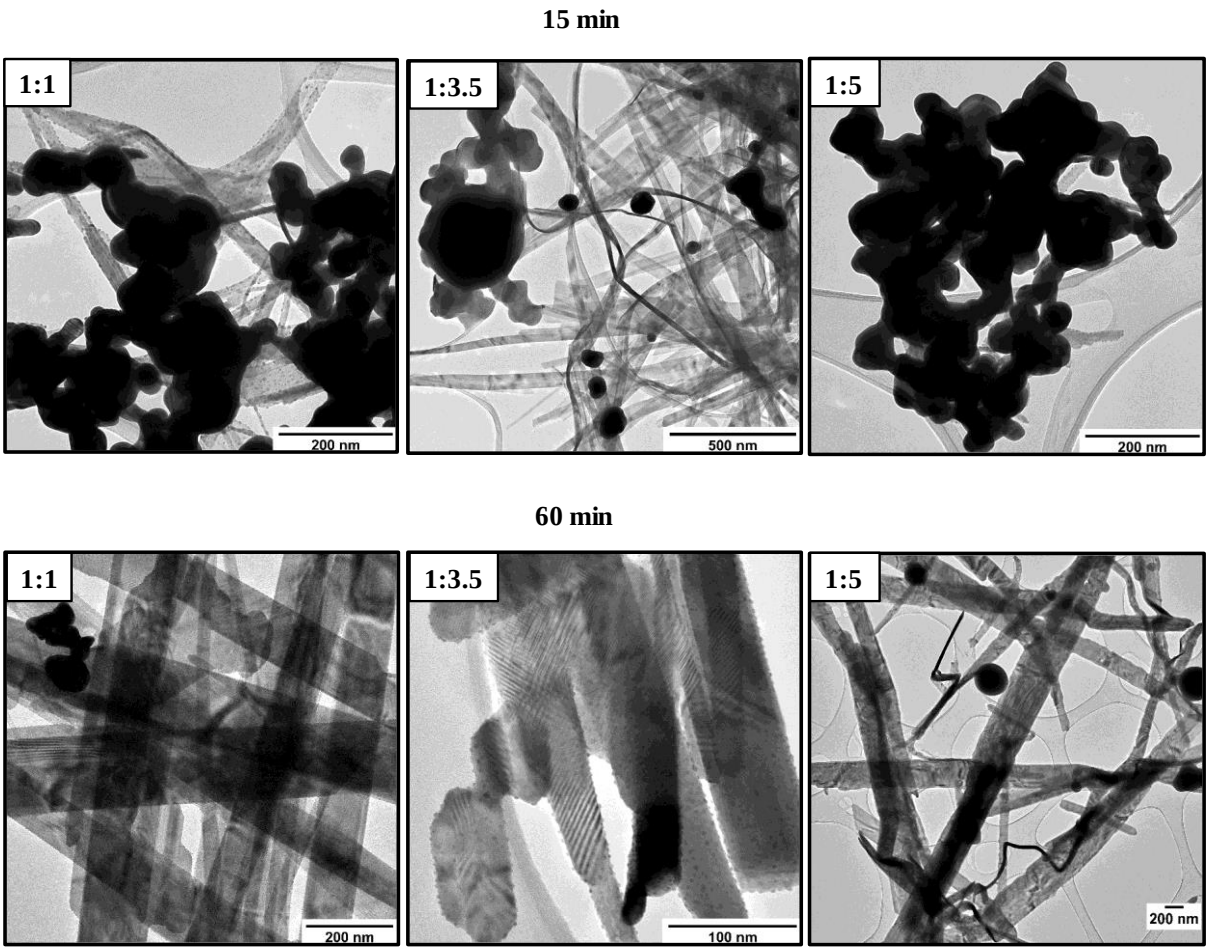

Fig. 3: TEM micrographs of particles synthesized in 15 min and 60 min for molar ratios 1:1, 1:3.5, and 1:5.

To further investigate on the tiny particles on belts, HRTEM analysis of the 60 min, 1:3.5 sample was done as shown in Fig. 4. The belt-structure showed distinctively clear lattice fringes with a d-spacing of 0.60 nm which suggests that the belts were growing in a 200 direction (α-AuSe, pattern number: 01-081-2226). Also visible on the surface of the nanobelts are small spherical deposits which also possess their own lattice fringes, with a d-spacing of 0.27 nm corresponding to the (111) peak of β-AuSe (pattern number 01-081-2227). This then suggests that during synthesis, β-AuSe nucleates on top of α-AuSe as no evidence of the dots on their own has been observed. The average particle size is 3.4 nm (Fig. 3S).

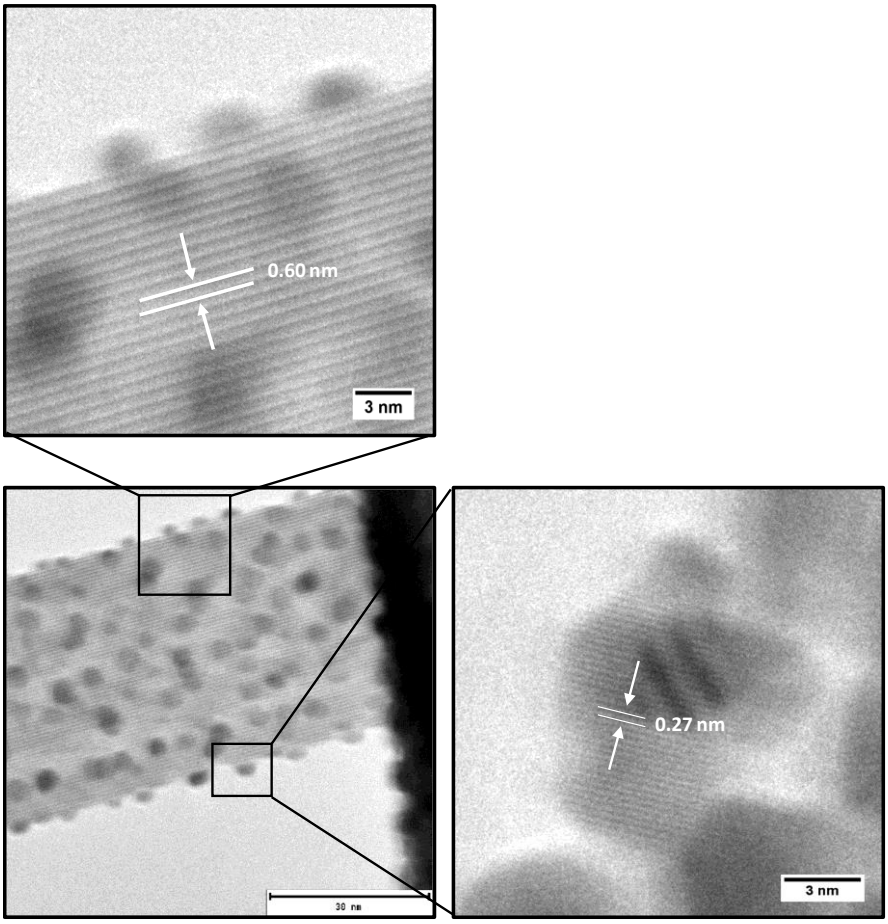

Fig. 4: HRTEM images of the nanobelt synthesized at 60 min from the 1:3.5 mol ratio reaction.

To study the properties of the spheres on belts further, XPS was performed. Shown in Fig. 5 is the XPS survey spectrum of the 60 min sample of the1:3.5 molar ratio. The spectrum shows a strong C1s peak confirming the presence of carbon due to the capping agent on the surface of the nanostructures. The attribution of the carbon peak to the capping agent is consistent with other reported work on capped nanoparticles and XPS has in fact been used to trace ligand exchange on the surface of the nanocrystals [23, 24]. The O 1s peak is attributed to the oxidation of the capping agent due to the adsorption of oxygen from the atmosphere. Also observed were the selenium and gold peaks attributed to gold selenide.

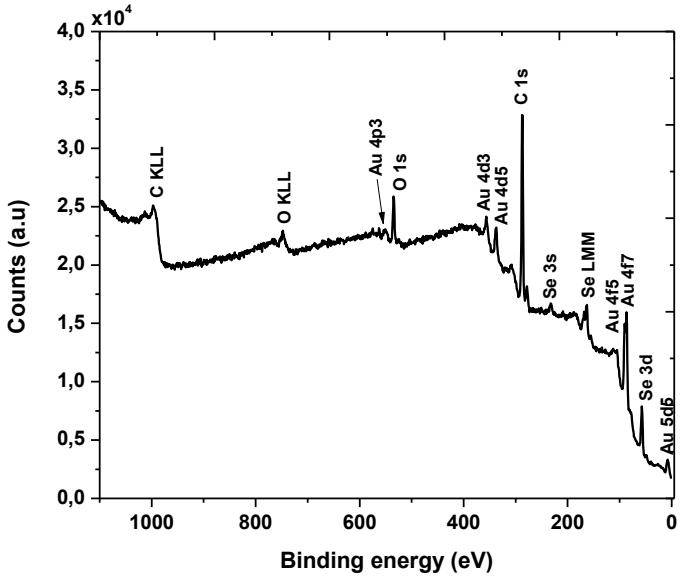

Fig. 5: XPS survey spectrum of gold selenide from the 1:3.5 molar ratio reaction at 60 min.

The high resolution XPS spectra with the focus on C1s, O1s, Au4f, and Se3d were done to evaluate the surface in more details (Fig. 6). The C1s core level spectrum showed a single C-C peak attributed to the oleylamine. The O1s peak also showed a single peak ascribed to the oxidation of the capping agent. Shown in Table 1 is the atomic % composition and peak area %. The large amount of carbon, 79.5%, is of course expected and is attributed to the capping agent that forms a large organic shell around each particle. The relatively low amount of oxygen (8.9%) further suggests that the AuSe core is protected from oxidation by the thick capping agent shell. The Au4f core level spectrum is characterized by four components composed of the $4f_{7/2}$ peaks at 83.7 eV and 84.9 eV attributed to Au^0 and Au^{1+} respectively. In addition, $4f_{5/2}$ peaks were also observed for Au^0 and Au^{1+} oxidation states at 87.4 and 88.7 eV. The presence of Au^0 suggests the formation of gold nanoparticles. The presence of zerovalent gold was detected by XRD, however, the particles were not observed in the TEM. α-AuSe and β-AuSe as previously stated are mixed-valent compounds comprising of Au^{1+} and Au^{3+} ions, however, the XPS results only shows the presence of Au^{1+} species. No work has been previously reported on the XPS of AuSe nevertheless the complexities of probing both the +1 and +3 states of mixed-valent compounds has also been observed in AgO [25]. AgO has an identical crystal structure to AuSe where Ag^{1+} is coordinated linearly to two oxygens and Ag^{3+} is coordinated to four oxygens in a square planar geometry [26]. The XPS studies of AgO has been a subject of controversy where a number of explanations have been suggested as indicative of the presence of the Ag^{3+} peak. Observations of small peak shifts and large FWHM of the Ag^{1+}

peaks as compared to the Ag^0 peaks have been attributed to the presence of the Ag^{3+} [27, 28]. These conclusions are however not quite accurate for AuSe as the Au^{3+} shows a distinct peak at ≈ 87 eV as previously reported in $HAuCl_4$ [29] and therefore does not overlap closely with the Au^{1+} peak as opposed to Ag^{1+} and Ag^{3+} peaks.

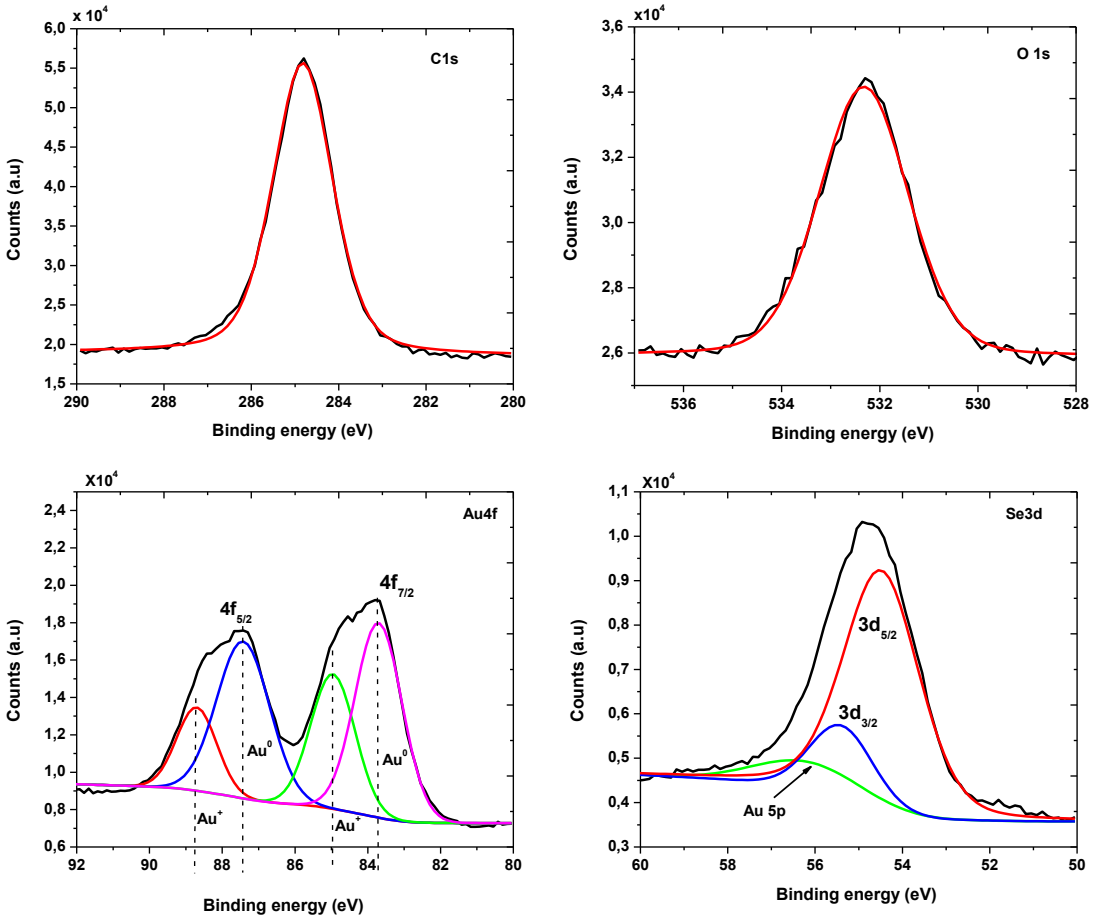

Fig. 6: High resolution core level spectra of AuSe with focus on C1s, O1s, Au4f and Se3d.

To ascertain whether indeed gold is bonded to selenium, a Se3d core level spectrum is shown in Fig. 6. The spectrum can be deconvoluted to three peaks attributed to the $3d_{5/2}$ (54.50 eV), $3d_{3/2}$ (55.42 eV) and Au5p (56.40 eV). The negative shift in the binding energies of the selenium peaks as compared to Se^0 can be attributed to the charge transfer from Au to the more electronegative selenium (Allred-Rochow electronegativity of Se is 2.48 versus 1.42 for Au) [30]. This, therefore, suggests the formation of AuSe. In addition, the presence of the Au5p peak, further suggests the bonding of the selenium to gold. Therefore, the Se core level spectrum strongly suggests the formation of AuSe and is thus in agreement with the observed XRD data.

Table 1: Summary of the atomic composition stoichiometric assignments obtained from the fitting of the XPS spectra reported in Fig. 6

Element	Atomic %	Peak Binding energy (eV)	Assignments	Peak area %
C	79.5	284.8	C-C	100
O	8.9	532.3	C-O	100
Au	2.7	83.7	Au^0 ($4f_{7/2}$)	34.1
		84.9	Au^{1+} ($4f_{7/2}$)	22.3
		87.4	Au^0 ($4f_{5/2}$)	31.1
		88.7	Au^{1+} ($4f_{5/2}$)	12.4
Se	7.6	54.5	$3d_{5/2}$	73.9
		55.4	$3d_{3/2}$	16.2
		56.4	$Au5p_{3/2}$	9.9

Temperature studies can be used to manipulate and modify phases of crystals. In addition, the purity of the products can also be affected by changes in temperature. Herein, the temperature was varied from 160 °C to 280 °C. The range of the temperature is largely dependent on the solvent used; OLA has a boiling point of 364 °C, however, it has a relatively low flash point 154 °C. In addition, as the temperature is elevated to 300 °C or above, a higher degree of the solvent exists in the vapour form, therefore, affecting the overall concentration of the solution. Shown in Fig. 7 are the XRD patterns of samples synthesized using 1:3.5 molar ratio for 60 min at 160 °C, 200 °C (reported above) and 280 °C. At 160 °C, the reactivity of selenium is quite poor as shown by the presences of the selenium peaks. Nevertheless, only α-AuSe was formed as opposed to the mixture of α- and β-AuSe previously seen for the 200 °C sample. At 280 °C, the mixture persists however strong gold peaks start to emerge suggesting that higher temperatures result in a more reductive environment (Au^{3+} reduced to Au^0).

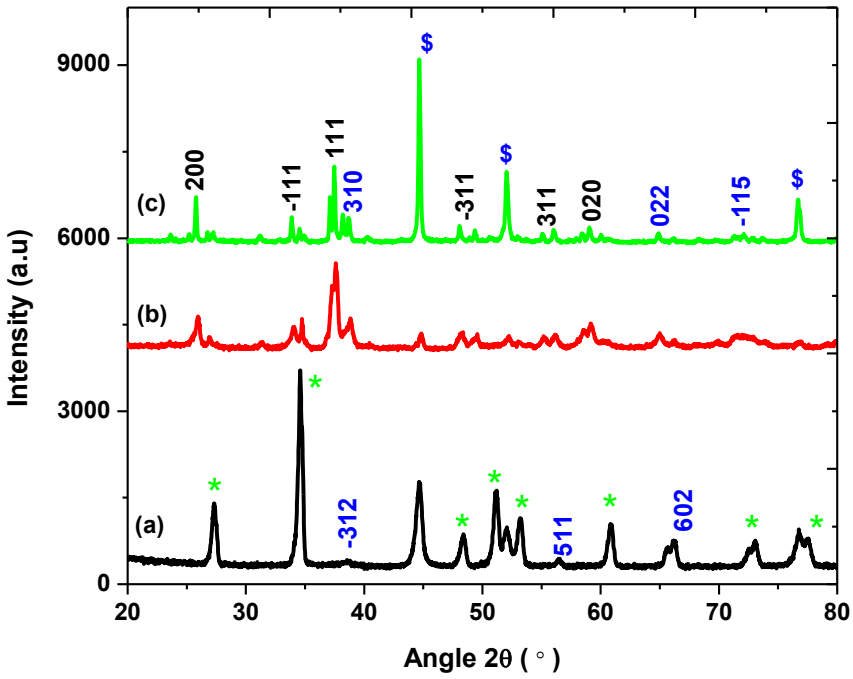

Fig. 7: XRD patterns of the particles synthesized using 1:3.5 molar ratio for 60 min at (a) 160 °C, (b) 200 °C and (c) 280 °C. ($ denotes gold, * denotes selenium, β-AuSe (black indices) and α-AuSe (blue indices)).

To evaluate the morphologies of the resultant materials, TEM was done. Shown in Fig. 8 are the TEM images of the samples synthesized at different temperatures. The particles produced at 160 °C, show small agglomerated nanorods identified as AuSe using EDS (Fig. 2S). At 200 °C, a mixture of spherical β-AuSe on top of α-AuSe nanobelts is observed. At 280 °C, big and broad gold selenide nanosheets/belts form similar to those obtained in a 1:1 reaction at 60 min shown in Fig. 3. The drastic change in size is due to the Ostwald ripening process.

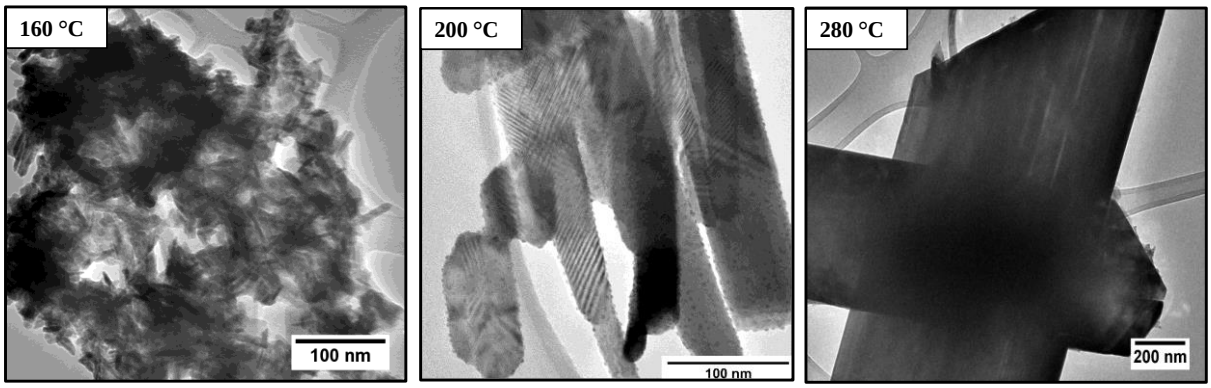

Fig. 8: TEM images of the particles synthesized using 1:3.5 molar ratio for 60 min at 160 °C, 200 °C and 280 °C.

4. Conclusion

Herein, α-AuSe and β-AuSe have been synthesized using a colloidal method for the first time. The β-AuSe was the predominant phase in the molar ratio studies, however, the α-phase was also observed. The resultant materials had interesting morphologies; long flexible or bendable nanobelts (α-AuSe) with β-AuSe nanospheres deposited on their surfaces. There was no evidence of the mixed valence (Au^{1+} and Au^{3+}) in the XPS as suggested by the crystal structures of both the phases of AuSe. However, there was strong evidence of the formation of the AuSe using the Se3d core level spectrum. The negative shift in the binding energies of the selenium peaks as compared to Se^0 was attributed to the charge transfer from Au to the more electronegative selenium, this suggested the formation of AuSe. In addition, the presence of the Au5p peak further suggested the bonding of the selenium to gold. These results were therefore in agreement with the observed XRD data. Varying the temperature did not improve the purity of the samples as unreacted selenium was observed at lower temperatures and reduced gold was observed at higher temperatures. Evident from the obtained results is the complexity of the Au-Se system hence the lack of reports in the literature. Strategies to remove the impurities are being pursued. Nonetheless, Au-Se is an interesting system as it adds to the class of 2D materials and due to its metallic conductivity, it can find use in applications similar to those of graphene such as being electrode materials in batteries, supercapacitors, and solar cells.

Acknowledgments

The authors would like to thank the University of the Witwatersrand, the Wits Microscopy and Microanalysis Unit (MMU), University of Malaga, Spain for their XPS facility and MINTEK for their HRTEM facility as well as their financial support.

References

[1] E.S. Reich, Nature 506 (2014) 19.

[2] H.O.H. Churchill, P. Jarillo-Herrero, Nat. Nanotechnol. 9 (2014) 330-331.

[3] K. Li, Y. Yu, G.J. Ye, Q. Ge, X. Ou, H. Wu, D. Feng, X.H. Cheng, Y. Zhang, Nat. Nanotechnol. 9 (2014) 372-377.

[4] O. Amiri, N. Mir, F. Ansari, M. Salavati-Niasari, Electrochimica Acta 252 (2017) 315-321.

[5] M. Mahdiani, F. Soofivand, F. Ansari, M. Salavati-Niasari, J. Clean. Prod. 176 (2018) 1185-1197.

[6] M.A. Airo, S. Gqoba, F. Otieno, M.J. Moloto, N. Moloto, RSC Adv. 6(47) (2016) 40777-40784.
[7] S. Gqoba, M. Airo, N. Ntholeng, L. Machogo, R. Sithole, M.J. Moloto, J. Van Wyk, N. Moloto, Materials Today: Proceedings 2(7) (2015) 3901-3908.
[8] G.E. Cranton, R.D. Heydin, Can. J. Chem. 46 (1968) 2637-2640.
[9] A. Rabeneu, Heinz Schulz, J. Less-Common Met. 48 (1976) 89-101.
[10] X. Fan, P. Xu, Y.C. Li, D. Zhou, Y. Sun, M.A.T. Nguyen, M. Terrones, T.E. Mallouk, J. Am. Chem. Soc. 138(15) (2016) 5143-5149.
[11] D. Voiry, H. Yamaguchi, J.W. Li, R. Silva, D.C.B. Alves, T. Fujita, M.W. Chen, T. Asefa, V.B. Shenoy, G. Eda, M. Chhowalla, Nature Mater. 12 (2013) 850-855.
[12] S. Tongay, W. Fan, J. Kang, J. Park, U. Koldemir, J. Suh, D.S. Narang, K. Liu, J. Ji, J. Li, R. Sinclair, J. Wu, Nano Lett., 14(6) (2014) 3185-3190.
[13] X.-Q. Zhang, W. Zhang, M.-T. Chang, C.-T. Lin, K.-D. Chang, Y.-C. Yu, J.T-W. Wang, C.-S. Chang, L.-J. Li, T.-W. Lin, Adv. Mater. 24(17) (2012) 2320-2325.
[14] Y.J. Zhan, Z. Liu, S. Najmaei, P.M. Ajayan, J. Lou, Small 8(7) (2012) 966-971.
[15] F. Ansari, A. Sobhani, M. Salavati-Niasari, J. Colloid Interface Sci. 514 (2018) 723-732.
[16] M. Mahdian, A. Sobhani, F. Ansari, M. Salavati-Niasari, J. Mater. Sci. Mater. Electron. 28 (2017) 17627-17634.
[17] M. Ghanbari, F. Ansari, M. Salavati-Niasari, Inorganica Chim. Acta 455 (2017) 88-97.
[18] M. Nath, A. Govindaraj, C.N.R. Rao, Adv. Mater. 13(4) (2001) 283-286.
[19] N. Moloto, M.J. Moloto, N.J. Coville, S. Sinha Ray, J. Cryst. Growth 324(1) (2011) 41-52.
[20] S.S. Nelwamondo, M.J. Moloto, R.W. Krause, N. Moloto, Mater. Res. Bull. 47(12) (2012) 4392-4397.
[21] T. Xaba, M.J. Moloto, N. Moloto, Mater. Lett. 146 (2015) 91-95.
[22] N. Moloto, M.J. Moloto, N.J. Coville, S.S. Ray, J. Cryst. Growth 311(15) 3924-3932.
[23] A. Atewologun, W. Ge, A.D. Stiff-Roberts, Journal of Elec. Materi. 42 (2013) 809-814.
[24] I-S. Liu, H-H. Lo, C-T. Chien, Y-Y. Lin, C-W. Chen, Y-F. Chan, W-F. Sue, S-C. Liou, J. Mater. Chem. 18 (2008) 675-682.
[25] A.M. Ferraria, A.P. Carapeto, A.M. Botelho do Rego, Vacuum 86 (2012) 1988-1991.
[26] J.P. Allen, D.O. Scanlon, G.W. Watson, Phys. Rev. B 81 (2010) 161103(R).
[27] J.F. Weaver, G.B. Hoflund, J. Phys. Chem. 98 (1994) 8519-8924.
[28] G.B. Hoflund, Z.F. Hazos, Phys. Rev. B 62 (2000) 11126.
[29] X. Zhang, H. Shi, B.-Q. Xu, Angew. Chem. Int. Ed. 44 (2005) 7132-7135.

[30] A.L. Allred, E.G. Rochow, J. lnorg. Nucl. Chem. 5 (1958) 264-268.

Chapter 4

Elucidating the structural properties of gold selenide nanostructures

Abstract

Noble transition metal chalcogenide gold selenide is a relatively unexplored layered material. Herein, we report on the synthesis and characterization of polymorphic mixed-valent AuSe ($Au^{1+}Au^{3+}Se_2$) by varying the sequence of the addition of the precursors in a colloidal synthesis. Despite the variations, all produced materials showed the co-existence of α- and β-AuSe. Although both polymorphs were observed, XRD showed that the addition of the gold precursor at higher temperatures resulted in α-AuSe being the dominant phase while the addition at lower temperatures resulted in β-AuSe being preferred. The crystal structures of both α- and β-AuSe consist of repeating units of linearly bonded Au^{1+} ion to two Se atoms and Au^{3+} ion bonded to four Se atoms in a square planar geometry. The Au4f core level spectrum of the XPS, showed only the Au^{+1} oxidation state, however, using the Se3d core level spectrum, the formation of AuSe ($Au^{+1}Au^{+3}Se_2$) was evident. Using DFT calculations, the Raman spectra of α- and β-AuSe were simulated and only the square planar geometry was found to be Raman active. The square planar geometry $(Au^{3+}Se_4)^-$ ions belonging to the D_{4h} point group produced three Raman active vibrational modes, namely, a symmetric stretch (A_{1g}), a planar bending (B_{1g}) and an asymmetric stretch (B_{2g}) for α-AuSe as well as A_{1g} and B_{1g} for β-AuSe. Experimentally, all samples showed Raman vibrational lines from both phases. Moreover, Raman spectroscopy confirmed the presence of Au^{3+} in AuSe which was not detected using XPS. From the TEM and SEM results, it was evident that the morphologies of the predominantly α-AuSe samples were nanobelts while the predominantly β-AuSe samples showed plate-like structures. The predominantly α-AuSe samples showed a broad absorption band with a maximum at 853 nm while the predominantly β-AuSe samples showed evidence of absorption however with no defined excitonic peak.

Keywords: Gold selenide; structural properties; optical properties

1. Introduction

The discovery of graphene and its benefits in the early 2000s brought much interest to this two-dimensional material and opened new avenues into the investigations of similar materials and their potential in various applications. It revolutionized the way in which bulk layered materials were perceived, i.e. they could now exist as low-dimensional structures (zero-, one- and two-dimensional) with completely different physical, chemical, and optical properties. These layered materials consist of monolayers of covalently bonded atoms held together by relatively weak van der Waals forces [1]. Most emerging 2D materials are derived from structures that are layered in the bulk [2]. When determining material properties, dimensionality is a defining parameter because restrictions in one or more dimensions can alter the properties of the material. For example, the optical and electronic properties of the transition metal dichalcogenide MoS_2 change from indirect to direct bandgap when transitioning from a multilayer structure to a monolayer, a behaviour arising from d-orbital related interactions [3, 4]. Some qualities and properties of these 2D materials that have made them advantageous include (i) being atomically thin and providing a larger surface area due to the complete exposure of surface atoms, (ii) having the edge sites chemically more reactive than basal planes and the open van der Waals gaps enabling the intercalation and (iii) the mechanical strength and flexibility at atomic dimensions allowing them to be used in next-generation wearable electronics [5].

A reasonable amount of research has been conducted and reported on some layered transition metal chalcogenides such as MoS_2, InSe, In_2S_3, $CuSe_2$ [6-8] however, very little information is available on the noble metal chalcogenide gold selenide (AuSe), a layered material in the bulk. Due to its metallic conductivity, it can find use in applications similar to those of graphene such as being electrode materials in batteries, supercapacitors, and solar cells. The mixed valent inorganic compound $Au^{+}Au^{3+}Se_2$, simplified/reduced as AuSe, has a highly crystalline structure and belongs to the C2/m space group with two known phase modifications α- and β-AuSe [9, 10]. The two polymorphs can be easily distinguished by their most intense reflections along the (310) crystal plane for α-AuSe and the (111) crystal plane for β-AuSe. In a recent publication, Machogo *et al.* detailed the first colloidal synthesis of AuSe and noted the co-existence of both alpha and beta phase in the material regardless of the Au/Se mole ratios or time or temperature employed [11]. In addition to co-crystallization of both the alpha and beta form, elemental gold and selenium have also been found to readily crystallize out as impurities. Finally, the last of the crystallization challenges is the conundrum of the oxidation state of gold

in gold selenide. As previously mentioned, using crystallography, AuSe has been shown to be a mixed valence compound with gold present at oxidation state +1 and +3 [12]. However, a few studies using X-ray photoelectron spectroscopy have shown only the existence of Au^{1+} oxidation state, therefore making it difficult to corroborate the crystallography results [11]. Herein, in an added attempt to produce pure phase AuSe, the order of precursor addition was varied. Previously, Ntholeng *et al.* showed that the sequence of adding the precursor can result in the elimination of impurities as the result on the influence on the nucleation and growth process [13]. In addition, XPS and Raman (theoretical and experimental) spectroscopy studies were performed to further probe the structure of AuSe in order to establish the mixed valency of gold.

2. Experimental

2.1 Chemicals

Gold (III) chloride hydrate 99%, 99% elemental selenium powder, 70% oleylamine (OLA), toluene and 96% absolute ethanol were obtained from Sigma Aldrich and used without any further processing.

2.2 Synthesis of the different materials of gold selenide

A. In a three-neck round bottom flask, inert conditions were achieved by passing nitrogen gas 20 min before precursor addition and continued until the reaction was terminated. Under strong magnetic stirring and reflux, 15 mL of clear OLA was heated to 100 °C followed by the addition of 0.28 g selenium dissolved in 5 mL of OLA which turned the solution light grey, the temperature was further raised to 200 °C and at this point 0.17 g gold chloride dissolved in 5 mL of OLA was subsequently added turning the reaction mixture black. The reaction was carried out at 200 °C and aged for 1 hour.

B. Reaction B was a reverse to the one mentioned in A above; in a three-neck flask, under strong magnetic stirring, 15 mL of clear OLA was heated to 100 °C followed by the addition of gold chloride in 5 mL OLA upon which the solution turned orange, the temperature was raised to 200 °C and 5 mL Se-OLA was then added finally changing the colour of the solution to black. The reaction was carried out at 200 °C under inert conditions and aged for 1 hour.

C. In a simultaneous addition reaction; 25 mL clear OLA was placed in a three-neck flask and heated to 200 °C under inert and strong magnetic stirring conditions. At this temperature both selenium powder and gold chloride crystals were added turning the

mixture to black as a result of the immediate nucleation. The reaction was maintained at 200 °C, stirred and aged for 1 hour.

D. In a gradual heating reaction, oleylamine, selenium powder and gold chloride were all placed in a three-neck flask and the temperature was raised to 200 °C over a period of 20 min. The reaction mixture was initially light grey in colour but gradually turned black during the heating process. Once the temperature was reached the reaction was aged for 1 hour. The mixture was subjected to strong magnetic stirring and inert conditions during the heating as well as aging processes. The different addition sequences are summarised in Table 1.

After aging, the samples collected and allowed to cool naturally. Ethanol was added to flocculate the particles as well was to wash off any excess OLA. Following, the particles were collected by centrifugation at 7000 rpm and the black resultant powders were left to dry at room temperature.

Table 1: Table showing the sequence of precursor addition (where ▲ denotes heating)

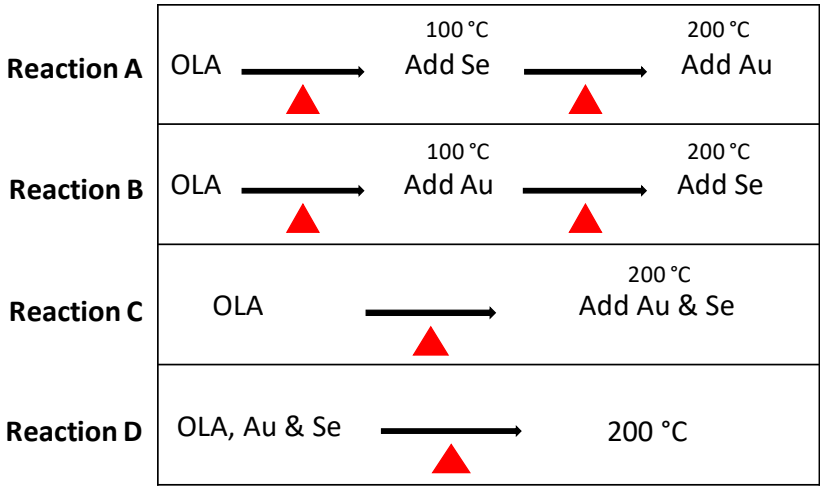

2.3 Characterization

X-ray diffraction

A Bruker D2 phaser (D2-205530) diffractometer using secondary graphite monochromated CuKα radiation (λ 1.5418 Å) at 30 kV and 10 mA was used to measure powder XRD patterns on the as-synthesized material. Measurements were taken using a glancing angle of incidence detector at an angle of 2˚, for 2θ values over 5 - 90˚ in steps of 0.036˚ with a step time of 0.5s and at a temperature of 294 K.

X-ray photoelectron spectroscopy

X-ray photoelectron spectroscopy (XPS) measurements were performed with a Physical Electronics PHI 5700 spectrometer with a multi-channel hemispherical electron analyzer. Non-monochromatic MgKα X-ray (300 W, 15 kV, 1253.6 eV) was used as excitation source. The spectrometer energy scale was calibrated using Cu $2p_{3/2}$, Ag $3d_{5/2}$, and Au $4f_{7/2}$ photoelectron lines at 932.7, 368.3, and 84.0 eV, respectively. Samples were mounted on a sample holder without adhesive tape and kept overnight at high vacuum in the preparation chamber before being transferred to the analysis chamber for testing. The spectra were collected in the constant pass energy mode at 29.35 eV. The residual pressure in the analysis chamber was maintained below 1.33×10^{-7} Pa during the spectra acquisition.

Raman spectroscopy

Raman analysis was performed using a T64000 series II triple spectrometer system from HORIBA scientific, Jobin Yvon Technology. The Raman spectra were obtained using 514.5 nm argon laser, through an Olympus microscope with a 50 X objective lens and laser power of 1.5 mW.

Computational calculations

The first-principles calculations based on density functional theory (DFT) [12] was executed using CASTEP module in Materials Studio developed by Accelrys Software Inc. The generalized gradient approximation with the scheme of Perdew–Bruke–Ernzerhof (GGA–PBE) [13] was utilized to represent the exchange-correlation functional in the DFT formalism. The α- and β-AuSe were generated using the crystal data reported by Rabenau *et al*. [14] as the initial structure and was optimized using CASTEP. Norm conserving pseudopotential was employed to describe the electron–ion interactions and plane-wave basis sets were used to represent electronic wave functions. The custom energy cut-off of plane wave basis was set to 990 eV, and the convergence criterion of electronic self-consistency was set to 5.

Electron microscopy

Transmission electron microscopy (TEM) was carried out on a FEI Technai T12 TEM microscope operated at an acceleration voltage of 120 kV with a beam spot size of 2 in TEM mode and an EDX detector, operated at 120 kV. The samples were initially suspended in toluene this was followed by placing a drop of the suspended nanomaterials, on a lacey-carbon copper grid. The grid with the sample was then allowed to dry at room temperature before

analysis. Scanning electron microscopy (SEM) was carried out on a FEI Nova Nanolab 600 FIB/SEM microscope. The powder samples were mounted on aluminium stubs with carbon tape and coated with one-layer (5nm) chromium. High angle annular dark field (HAADF) scanning transmission electron microscope (STEM) images and energy dispersive X-ray (EDX) mapping images were acquired using a JEOL JEM 2100 instrument operated at 200 kV.

Ultra Violet-Visible spectroscopy

A Specord 50 AnalytikJena UV-Vis spectrophotometer was used to carry out the absorption measurements. The nanomaterials were dispersed in toluene and placed in a quartz cuvette of 1 cm path length for absorption analyses.

3. Results and discussion

Colloidal synthesis is a favourable approach in that it is convenient and reproducible for fabricating nanocrystals with controlled size and shape using simple inexpensive and less energy-demanding processes and equipment [15]. During synthesis, various parameters such as time, temperature, solvent and starting materials can be altered thereby producing nanomaterials of a desired nature. Herein, the sequence in which the precursors were added was altered, thus, obtaining the following results. The black powdered samples were characterized by X-ray diffraction and the diffractograms are shown in Fig. 1. All four reactions showed the presence of both α-AuSe (JCPDS card 00-020-0457), and β-AuSe (JCPDS card 00-020-0458). Nevertheless, it was evident that the addition of gold at 200 °C (reaction A and C) resulted in the α-phase being more predominant whilst the β-phase became more dominant when the gold source was added at lower temperatures (reaction B and D). The formation of particles in a colloidal synthesis is thought to be governed by the nucleation and growth process described by Lamer and Dinegar [17]. The formation of the nuclei is a critical step and determines the overall properties of the resultant particles. In reaction A and C, initially, selenium nuclei are formed and upon the addition of the gold precursor at 200 °C, α-AuSe is produced. The concentration of selenium ions thereafter drops and this favour the formation of β-AuSe as there is excess of gold ions. The excess gold nuclei then form gold nanoparticles hence the observed gold peaks (JCPDS card 00-004-0784) with relatively high intensities.

On the contrary, the addition of the gold precursor at low temperatures results in a gold-rich environment and favours the formation of β-AuSe as previously reported by Rabenau *et al.* [18].

However small traces of gold are still observed in reaction B; previously Machogo *et al.* showed that regardless of the Au:Se ratio, gold still persists [11]. In addition, there's a large excess of selenium (JCPDS card 00-006-0362) observed for the reaction D. The heating up of both precursors from room temperature (reaction D) is evidently a less desirable route as it produces both Se and Au impurities at significant amounts.

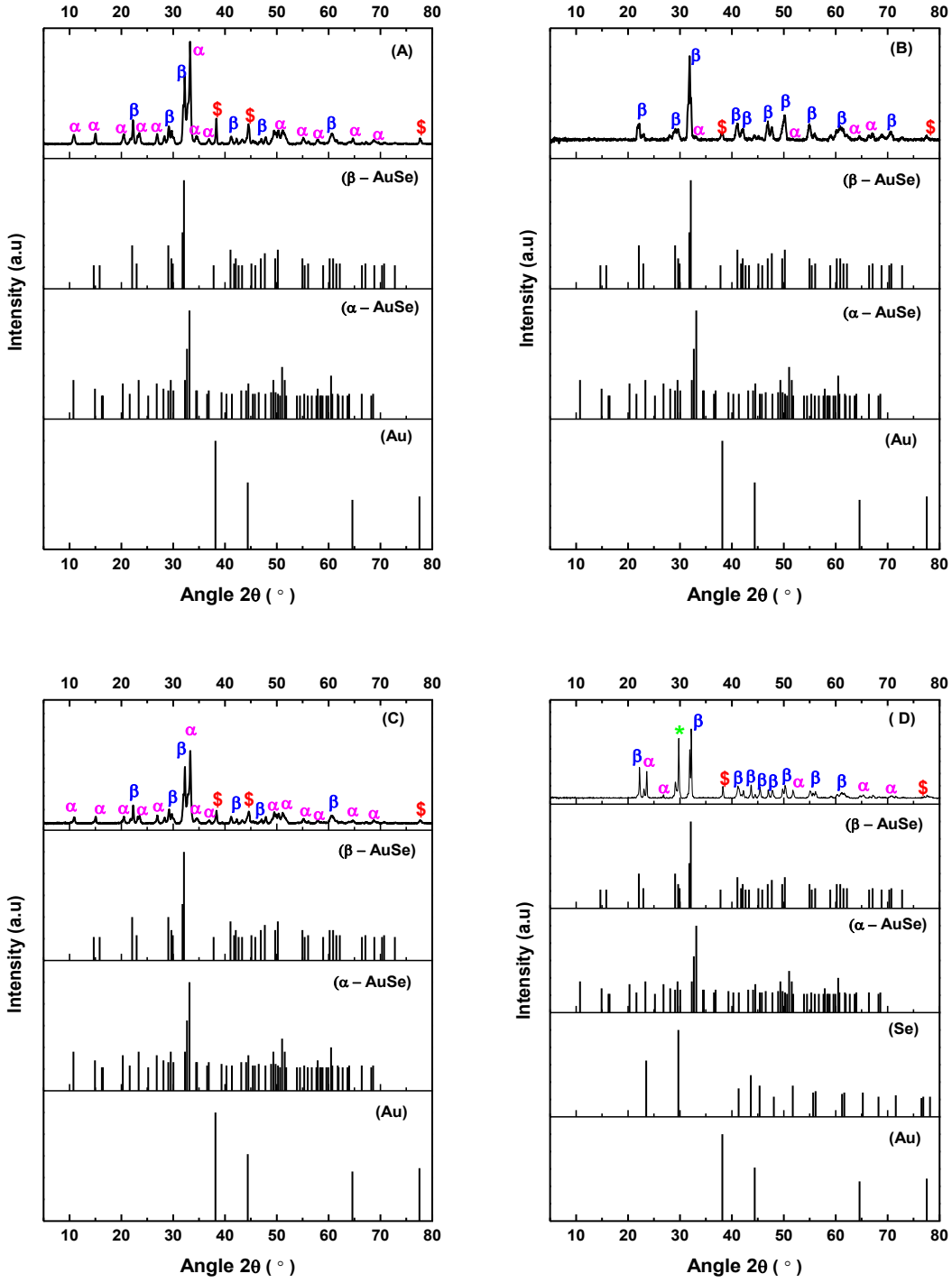

Fig. 1: Standard XRD patterns of α-AuSe, β-AuSe, elemental Au and elemental Se together with XRD patterns of as-synthesised materials using the different reaction methods A - D.

(Key: α = α-AuSe, β = β-AuSe, $ = elemental Au and * = elemental Se)

To further probe the structure of the nanomaterials, XPS was performed. The structure of gold selenide has presented some controversy as previously articulated by Machogo *et al.* and most recently by Vorobyev *et al.*; in particular, the presence of both Au^{+} and Au^{3+} in the crystal structure [11, 19]. The crystal structures of the two α- and β-AuSe polymorphs consists of Au^{1+} ions coordinated linearly by two selenium atoms while Au^{3+} ions are bonded to four selenium atoms in square planar geometry as shown in Fig. 2 [12]. Aside from the reported crystallographic data, there is no other confirmation of the existence of both oxidation states.

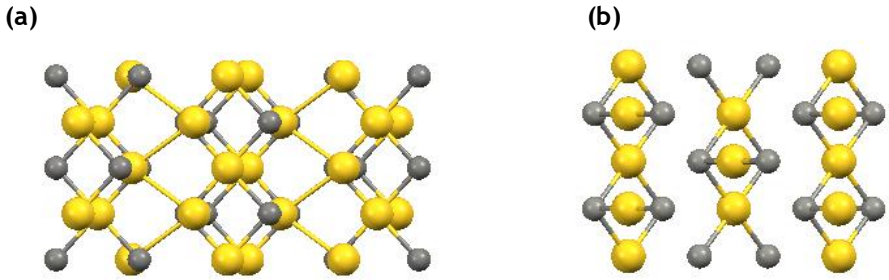

Fig. 2: Crystal structure of (a) α-AuSe and (b) β-AuSe [12].

Shown in Fig. 3 is the XPS survey spectrum of sample A. The spectrum shows a strong C1s peak confirming the presence of carbon due to the capping agent on the surface of the nanostructures. The attribution of the carbon peak to the capping agent is consistent with other reported work on capped nanoparticles and XPS has in fact been used to trace ligand exchange on the surface of the nanocrystals [20, 21]. The O1s peak is attributed to the oxidation of the capping agent due to the adsorption of oxygen from the atmosphere. Also observed were the selenium and gold peaks attributed to gold selenide.

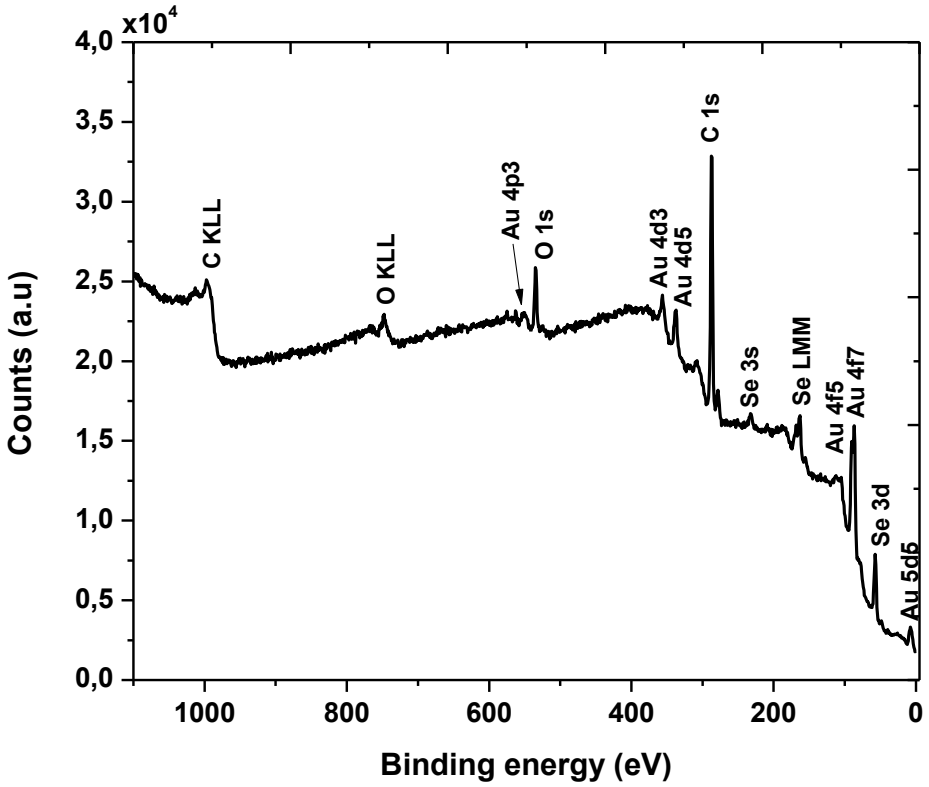

Fig. 3: XPS survey spectrum of gold selenide sample produced from method A.

The high resolution XPS spectra with the focus on C1s, O1s, Au4f, and Se3d were done to evaluate the surface in more detail (Fig. 4). The C1s core level spectrum showed a single C-C peak attributed to the oleylamine. The O1s peak also showed a single peak ascribed to the oxidation of the capping agent. Shown in Table 2 is the atomic % composition and peak area %. The large amount of carbon, 79.5%, is of course expected and is attributed to the capping agent that forms a large organic shell around each particle. The relatively low amount of oxygen (8.9%) further suggests that the AuSe core is protected from oxidation by the thick capping agent shell. The Au4f core level spectrum is characterized by four components composed of the $4f_{7/2}$ peaks at 83.7 eV and 84.9 eV attributed to Au^0 and Au^{1+} respectively. In addition, $4f_{5/2}$ peaks were also observed for Au^0 and Au^{1+} oxidation states at 87.4 and 88.7 eV. The presence of Au^0 suggests the formation of gold nanoparticles. The presence of zerovalent gold was detected by XRD, however, the particles were not observed in the TEM. α-AuSe and β-AuSe as previously stated are mixed-valent compounds comprising of Au^{1+} and Au^{3+} ions, however, the XPS results only shows the presence of Au^{1+} species. The complexities of probing both the +1 and +3 states of mixed-valent compounds have also been observed in AgO [22]. AgO has

an identical crystal structure to AuSe where Ag^{1+} is coordinated linearly to two oxygens and Ag^{3+} is coordinated to four oxygens in a square planar geometry [23]. The XPS studies of AgO have been a subject of controversy where a number of explanations have been suggested as indicative of the presence of the Ag^{3+} peak. Observations of small peak shifts and large FWHM of the Ag^{1+} peaks as compared to the Ag^{0} peaks have been attributed to the presence of the Ag^{3+} [24, 25]. These conclusions are however not quite accurate for AuSe as the Au^{3+} shows a distinct peak at ≈ 87 eV as previously reported in $HAuCl_4$ [26] and therefore does not overlap closely with the Au^{1+} peak as opposed to Ag^{1+} and Ag^{3+} peaks.

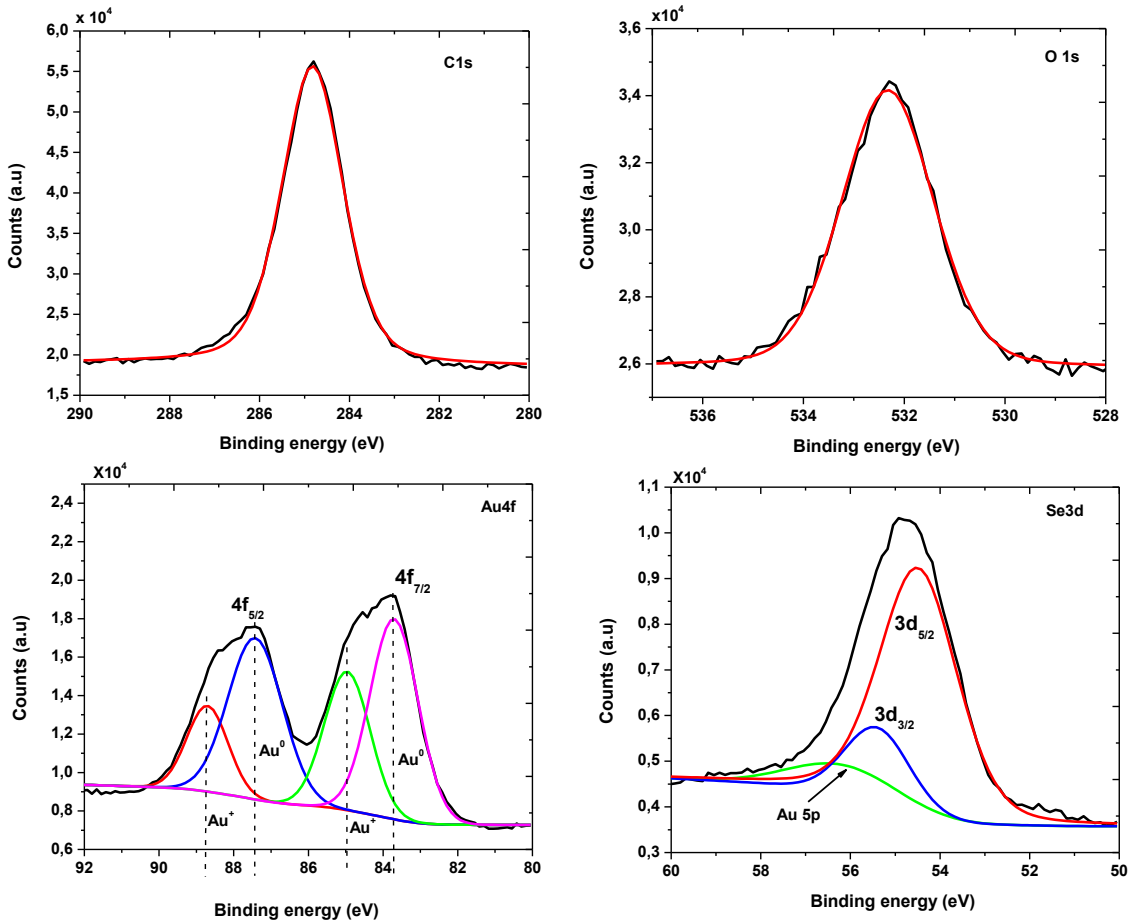

Fig. 4: High resolution core level spectra of AuSe with focus on C1s, O1s, Au4f and Se3d.

To ascertain whether indeed gold is bonded to selenium, a Se3d core level spectrum is shown in Fig. 4. The spectrum can be deconvoluted to three peaks attributed to the $3d_{5/2}$ (54.50 eV), $3d_{3/2}$ (55.42 eV) and Au5p (56.40 eV). The negative shift in the binding energies of the selenium peaks as compared to Se^0 can be attributed to the charge transfer from Au to the more

electronegative selenium (Allred-Rochow electronegativity of Se is 2.48 versus 1.42 for Au) [27]. This, therefore, suggests the formation of AuSe. In addition, the presence of the Au5p peak, further suggests the bonding of the selenium to gold. Therefore, the Se core level spectrum strongly suggests the formation of AuSe and is thus in agreement with the observed XRD data.

Table 2: Summary of the atomic composition stoichiometric assignments obtained from the fitting of the XPS spectra reported in Fig. 4.

Element	**Atomic %**	**Peak Binding energy (eV)**	**Assignments**	**Peak area %**
C	79.5	284.8	C-C	100
O	8.9	532.3	C-O	100
Au	2.7	83.7	Au^0 ($4f_{7/2}$)	34.1
		84.9	Au^{1+} ($4f_{7/2}$)	22.3
		87.4	Au^0 ($4f_{5/2}$)	31.1
		88.7	Au^{1+} ($4f_{5/2}$)	12.4
Se	7.6	54.5	$3d_{5/2}$	73.9
		55.4	$3d_{3/2}$	16.2
		56.4	$Au5p_{3/2}$	9.9

Raman spectroscopy was used as an additional tool to further probe the structure of gold selenide. Calculations of the Raman spectra of both α-AuSe and β-AuSe were executed using crystal data emanating from the crystal structure in Fig. 2 [12]. Using the data, only the square planar geometry showed Raman activity.

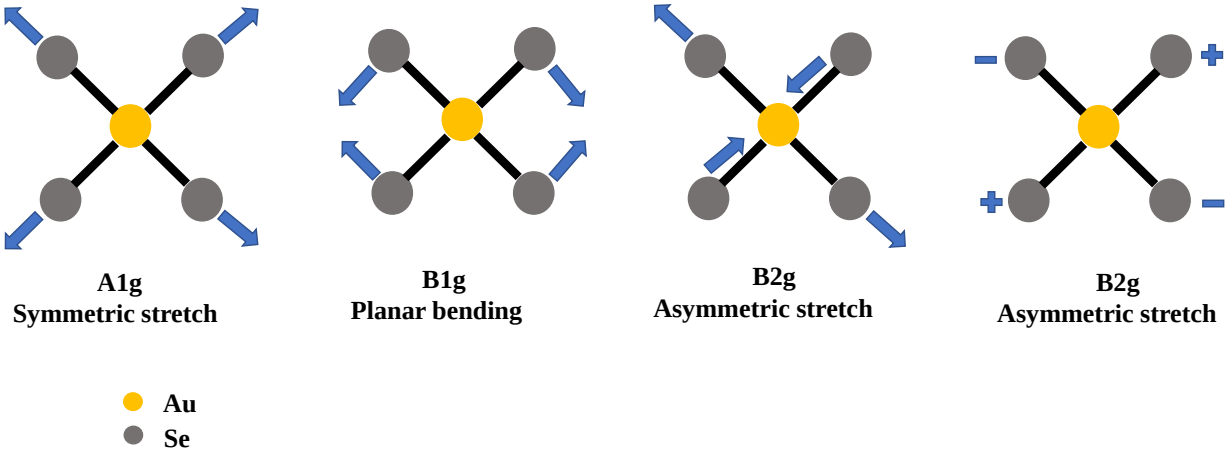

Fig. 5: Schematic representation of D_{4h} point group Raman active vibrational modes of square planar $(Au^{3+}Se_4)^-$ molecule.

Square planar molecules of MX^{n-} nature such as $(ICl_4)^-$, $(PtCl_4)^{2-}$ and $(AuCl_4)^-$ belong to the D_{4h} point group and their similarity to the $(Au^{3+}Se_4)^-$ ions in the current study was used to explain the obtained data. According to molecular symmetry, molecules belonging to D_{4h} point group give rise to seven vibrational normal modes of which three are Raman active and Fig. 5 gives a schematic representation of these Raman active normal modes. Fig. 6(i) shows the theoretical Raman spectra of α-AuSe and β-AuSe together with the experimental data for samples A and C, while Fig. 6(ii) shows the theoretical Raman spectra of α-AuSe and β-AuSe together with the experimental data for samples B and D. From the theoretical α-AuSe spectrum, three peaks are observed. The intense shift at 232 cm^{-1} is attributed to the A_{1g} normal mode and is due to the symmetric stretching of the Au–Se bond. The peak at 265 cm^{-1} is attributed to the antisymmetric stretching B_{2g} mode while the low intensity peak at 176 cm^{-1} is assigned to the B_{1g} normal mode for planar bending. The calculated Raman spectrum of β-AuSe showed two prominent vibrational peaks at 201 cm^{-1} and 306 cm^{-1} which were assigned to symmetric A_{1g} and antisymmetric stretching B_{2g}, respectively. These theoretical assignments were in agreement with reported experimental vibrational modes of square planar pentatomic complex halides [16]. With mixed valent AgO ($Ag^+Ag^{3+}O_2$) being an analogue to AuSe, i.e. Ag^+ is linearly bonded to two oxygen atoms while Ag^{3+} takes on a square planar geometry, it was of interest and therefore fitting to compare the Raman activity of AgO with that of AuSe. Three vibrational normal modes were observed similar to that of α-AuSe [17].

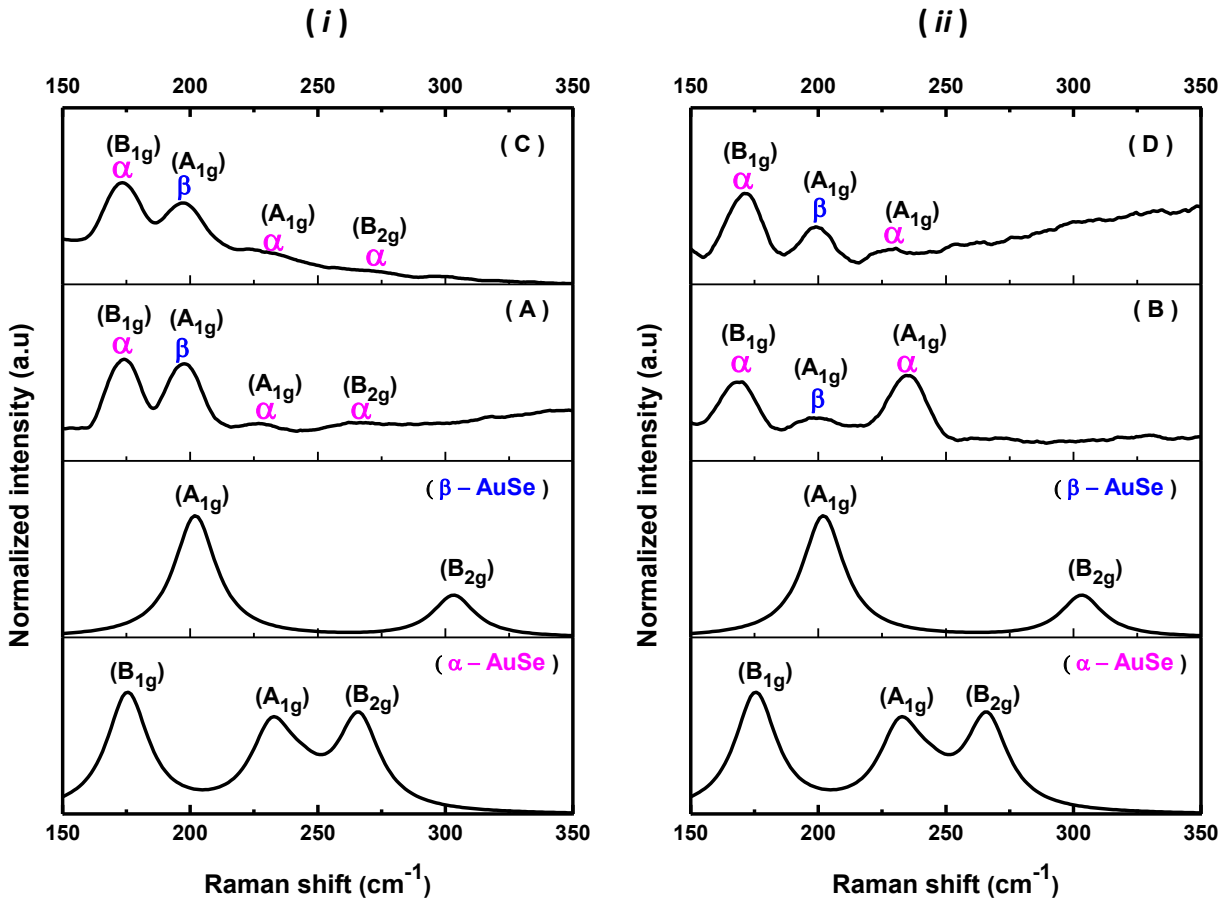

Fig. 6: *(i)* Calculated Raman spectra of α-AuSe and β-AuSe and experimental Raman spectra of as-synthesized AuSe of sample A and C, *(ii)* calculated Raman spectra of α-AuSe and β-AuSe and experimental Raman spectra of as-synthesized AuSe of sample B and D.

The Raman spectra of the particles synthesized via methods A, B, C and D are also shown in Fig. 6. The particles synthesized using methods A and C (Fig. 6(*i*)) revealed a mixture of α- and β-AuSe. The bending vibrations (B_{1g}) in both samples (A and C) was observed at slightly lower wavenumbers at 173 cm^{-1} and 174 cm^{-1}, respectively compared to the theoretical Raman peak of α-AuSe where the peak was observed at 176 cm^{-1}. The α-AuSe symmetric and antisymmetric stretching vibrations of A and C were observed at 224 cm^{-1}, 226 cm^{-1} and 263 cm^{-1}, 269 cm^{-1}, respectively. In addition to the α-AuSe peaks, one peak assigned to β-AuSe symmetric stretching vibration at 196 cm^{-1} for both samples A and C was observed. The shifts in the Raman peaks can be as a result of a number of things such as (i) peaks shifts are observed when layered materials transition from bulk to 2D monolayers [30], (ii) through presence of defects including extrinsic impurities [31] and (iii) lattice strain induced by defects or type of morphology [32]. The Raman spectra of samples B and D are shown in Fig. 6(*ii*). Of evidence

was the disappearance of the α-AuSe antisymmetric stretching vibration (B_{2g}) in both samples B and D. The bending mode (B_{1g}) of α-AuSe phase for sample B was observed at 168 cm^{-1} and that of sample D was observed 170 cm^{-1}, while the A_{1g} symmetric stretching vibration of the α-AuSe phase was observed at 235 cm^{-1} and 229 cm^{-1} respectively. A symmetric stretching vibration of β-AuSe phase was observed at 198 cm^{-1} and 199 cm^{-1} for B and D, respectively. These results revealed that all samples (A, B, C and D) contained both α- and β-AuSe phases, with sample A and C dominated by peaks of the α-phase. Bands not identified may be either very weak or obscured by highly intense bands. The frequencies of the Raman shifts are summarized in Table 3.

Table 3: Summary of the Raman frequencies and their vibrational assignments

Assignments	B_{1g} Planar bending (cm^{-1})	A_{1g} Symmetric stretching (cm^{-1})	B_{2g} Antisymmetric stretching (cm^{-1})
Theoretical α-AuSe	176	232	265
Reaction A	173	224	263
Reaction B	168	235	-
Reaction C	174	226	269
Reaction D	170	229	-
Theoretical β-AuSe		201	306
Reaction A	-	196	-
Reaction B	-	198	-
Reaction C	-	196	-
Reaction D	-	199	-

To get the morphological properties of the nanomaterials, electron microscopy was performed. Fig. 7 shows TEM micrographs of the different nanocrystals. Reactions A and C produced lightly contrasted AuSe nanobelts of various lengths and widths. Deposited on these nanobelts were tiny spherical particles, these are shown as an insert in Fig. 7A. This was also observed in previous experiments [11] and it was confirmed that the nanobelts were α-AuSe while the spherical particles deposited on top of the nanobelts were of β-AuSe nature. These findings also hold for the present study as XRD and Raman spectroscopy confirmed the presence of both polymorphs in samples A and C. Reaction B and D showed densely contrasted AuSe

nanoplates with those in sample B having a larger size than in D. The nanoplates in B were hexagonal in shape with defined facets while those in D had more cylindrical edges. Also observed on the Fig. 7B and 7D, were trace amounts of nanobelts. The nanoplates were the predominant morphologies observed in reactions B and D and were therefore attributed to β-AuSe as confirmed by XRD as the dominant phase.

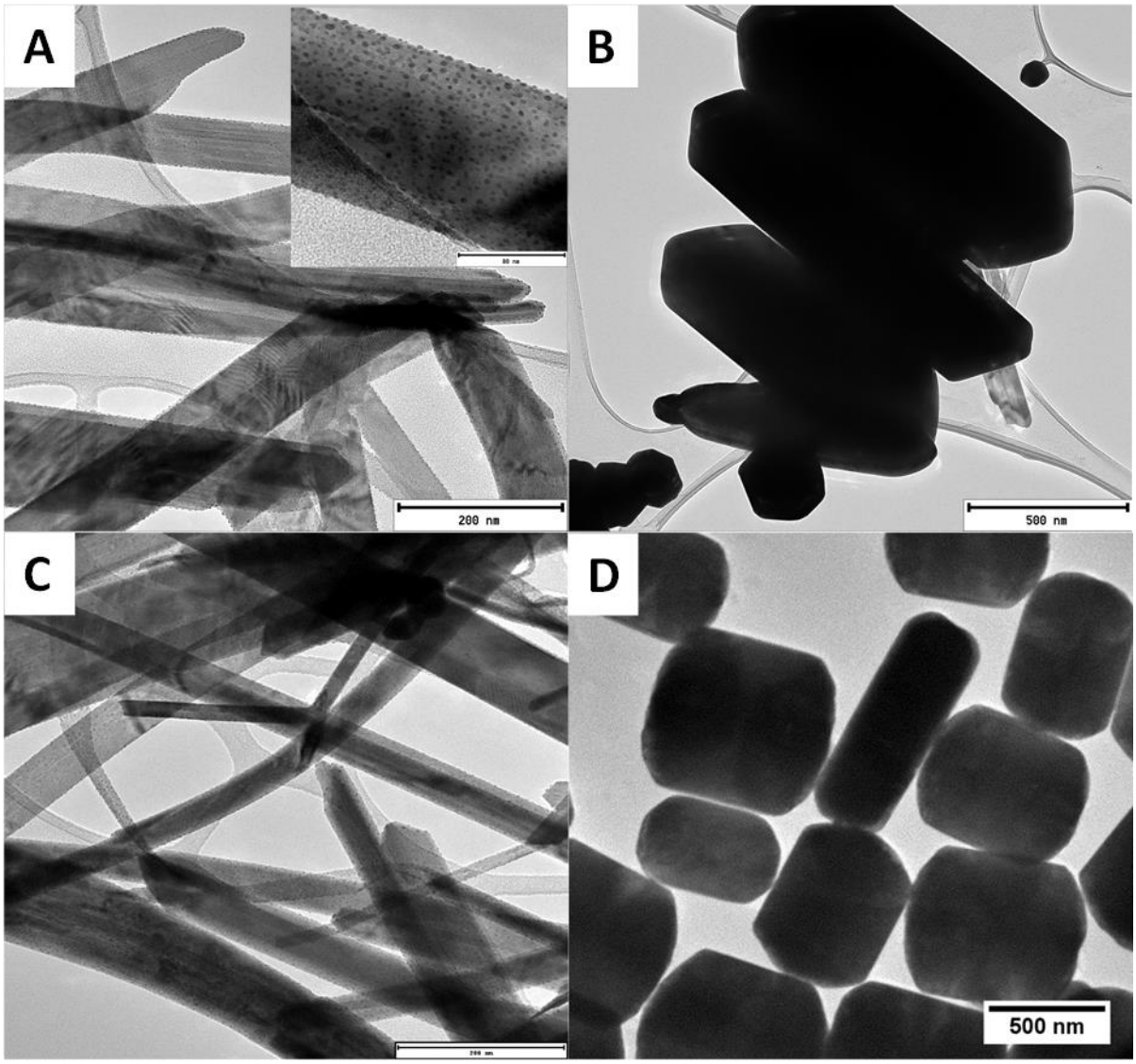

Fig. 7: TEM images of as-synthesized AuSe nanocrystals using the different reaction methods A - D (insert highlighting the nanospheres deposited onto the belts).

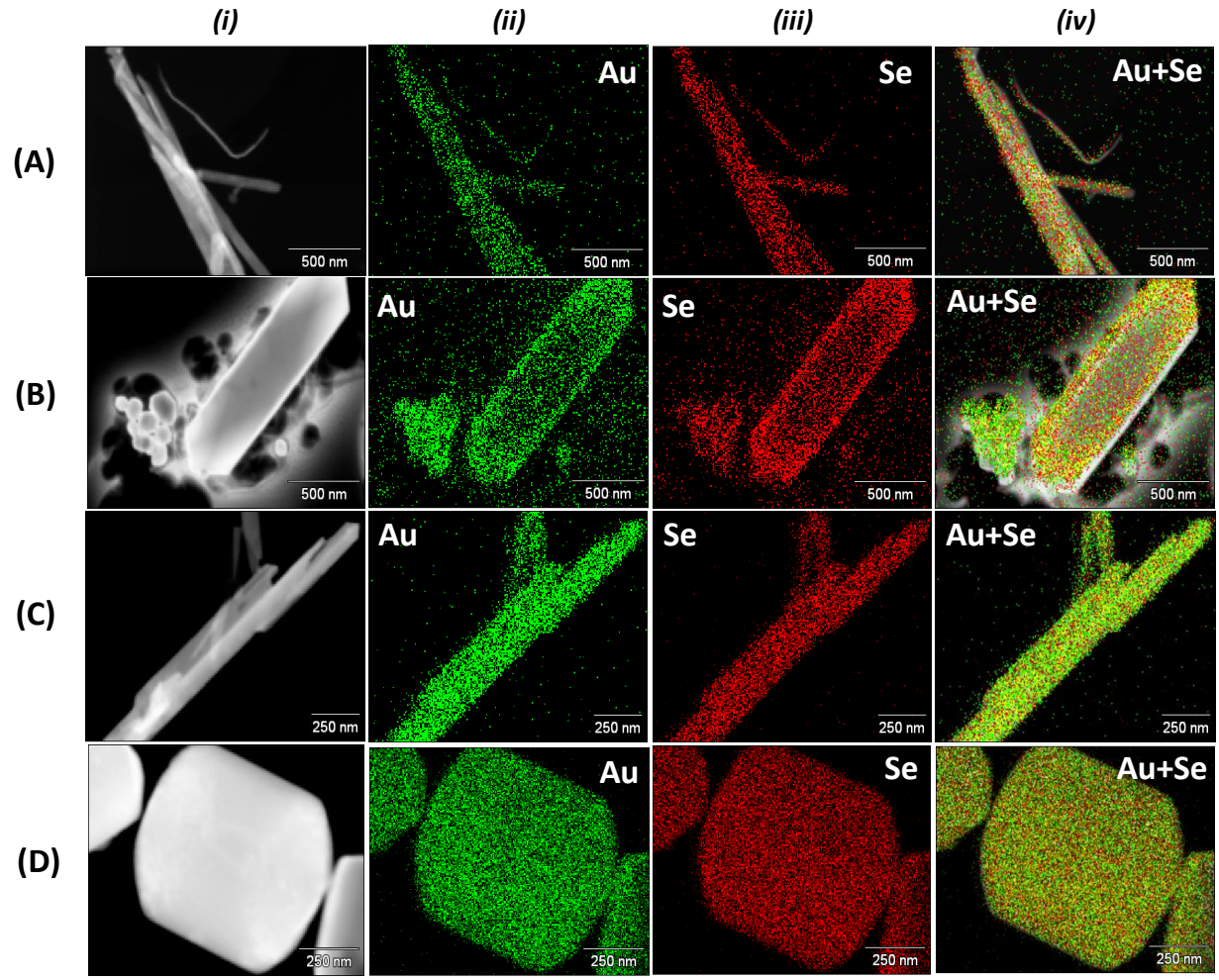

Fig. 8: *(i)* HAADF STEM images of single nanocrystals from each sample A - D, *(ii)* elemental mapping of Au, *(iii)* elemental mapping of Se and *(iv)* summed elemental mapping of both Au and Se for samples A - D.

XRD and XPS confirmed the coordination of Au to Se and therefore the formation of AuSe, but in order to see the extent of homogeneity of the samples, TEM EDX mapping was performed and the results are shown in Fig. 8. Column (i) shows the HAADF STEM images of the single nanostructures which were used as focus regions for each sample. Elemental mapping analysis in column (ii) depicts an even distribution of Au on the nanocrystals, equally, an even distribution of Se is observed in column (iii), for all samples. The summed mappings in column (iv) illustrates the uniformity in distribution of both elements giving complete homogenous AuSe nanomaterials. Shown in Fig. 9 are the SEM images of the synthesized materials. As previously observed in the TEM images, the nanobelts were obtained from reactions A and C whilst nanoplates were obtained in reactions B and D. For the nanoplates,

the SEM images confirm that they are plates. The rod-like shapes appear to be plates lying on one side.

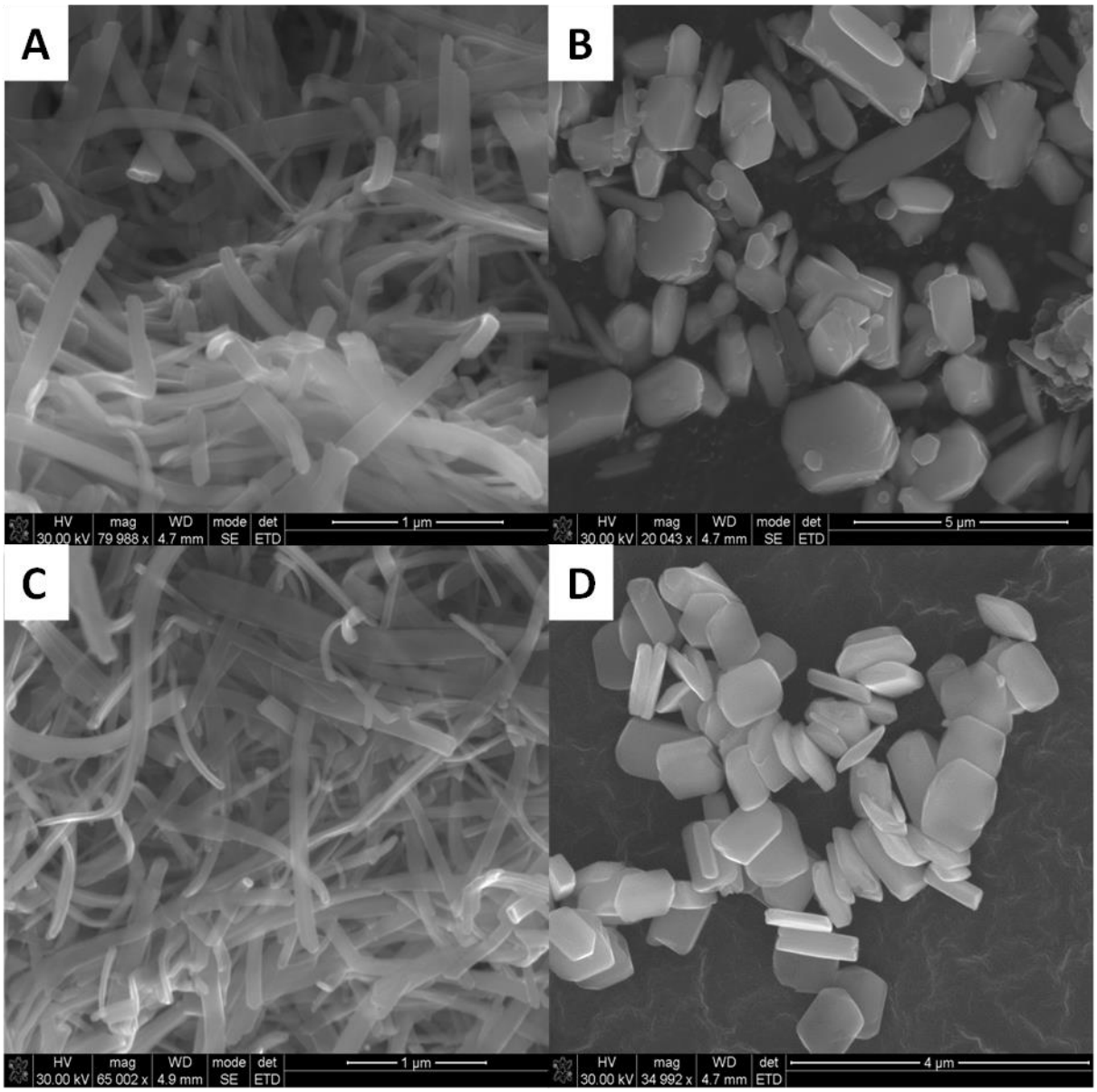

Fig. 9: SEM images of AuSe nanocrystals using the different reaction methods A - D.

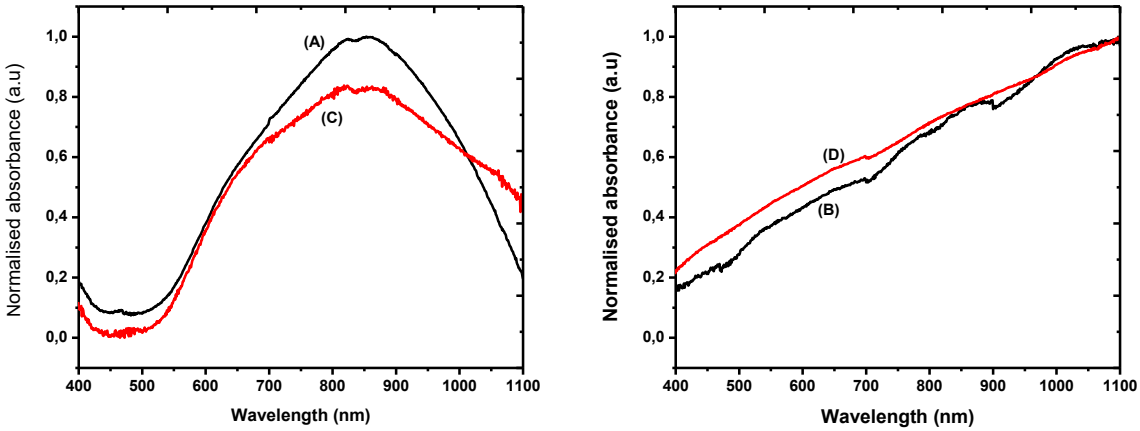

Fig. 10: UV-Vis absorption spectra of the as-synthesized AuSe.

To investigate the optical properties of the nanostructures, UV-Vis absorption spectroscopy was employed, and the obtained spectra are presented in Fig. 10. The α-AuSe dominant samples from reaction A and C showed a large absorption band with a maximum at 853 nm. The broadness of the band is indicative of polydispersed samples. Metal chalcogenides with metallic conductivity such as $Cu_{2-x}Se$ ($x > 0$) and in this case AuSe have been shown to possess NIR localized surface plasmon resonance (LSPR) [33]. Samples from reactions B and D, the β-AuSe dominant samples illustrated an even larger absorption spectral window which spans from 400 nm well beyond 1100 nm (which is the spectral limit of the instrument). This together with the various shoulders observed, suggest that the samples are extremely polydispersed. This is consistent with the electron microscopy images presented above. The surface plasmon resonance (SPR) of gold nanoparticles is well known to be between approximately 500 nm - 600 nm depending on the size and shape [34]. XRD confirmed the presence of gold particle impurities for all samples, for sample A and C, a small shoulder peak slightly red-shifted from 600 nm can be attributed to large Au nanoparticles however it is impossible to assign any peaks for samples B and D.

4. Conclusion

In summary, colloidal synthesis was employed and produced polymorphic gold selenide nanomaterials. In all experiments, both α-AuSe and β-AuSe were formed, however, a level of dominance was observed depending on the sequence of precursor addition. XRD showed that α-AuSe was the dominant phase when gold precursor was added at an elevated temperature contrary to the addition of gold at lower temperatures which presented β-AuSe as dominant.

The Au4f core level spectrum in XPS was able to probe the Au^{+} ions, additionally the Se3d core level spectrum showed evidence of the formation of AuSe with the presence of the Au5p peak suggesting bonding of the selenium to gold. Density Functional Theory calculations gave theoretical Raman spectra which were composed of 3 and 2 lines of Raman-active vibrational modes for α-AuSe and β-AuSe, respectively. Modes of both α- and β-AuSe were present in all four samples, further confirming the co-existence of both phases. Moreover, Raman confirmed the existence of Au^{3+} in the crystal structure further validating the mixed valency of the material. Electron microscopy highlighted the different shapes of these phases; α-AuSe being nanobelts while β-AuSe having plate-like morphology. Elemental mapping of the nanostructures illustrated an even distribution of gold and selenium across all samples confirming the homogenous nature of the nanomaterial. The broad absorbance bands in the UV-Vis spectra of both α-AuSe and β-AuSe showed LSPR in the NIR. These investigations accentuated the co-existence of both polymorphs of AuSe despite various attempts to isolate pure mono-phased AuSe nanomaterials. This could suggest some sort of co-dependence of one form on the other.

Acknowledgments

The authors would like to thank the University of the Witwatersrand, School of Chemistry, University of Malaga (Spain) for the XPS, the Wits Microscopy and Microanalysis Unit (MMU) for their facilities and Rhandzu Rikhotso at the CSIR NCNSM for work performed on TEM EDX mapping. Gratitude also goes to Mintek and NRF for their financial support.

References

[1] M. Pumera, and A.H. Loo, Trends in Analytical Chemistry, 61 (2014) 49-53.

[2] A.J. Mannix, B. Kiraly, M.C. Hersam and N.P. Guisinger, Nature Reviews Chemistry, 1 (2) (2017) 0014.

[3] R. Mas-Balleste, C. Gomez-Navarro, J. Gomez-Herrero and F. Zamora, Nanoscale, 3 (1) (2011) 20-30.

[4] A. Splendiani, L. Sun,Y. Zhang, T. Li, J. Kim, C-H. Chim, G, Galli and F. Wang, Nano Letters, 10 (4) (2010) 1271-1275.

[5] K.S. Kumar, N. Choudhary, Y. Jung, and J. Thomas, ACS Energy Letters, 3 (2) (2018) 482-495.

[6] P.D. Matthews, P.D. McNaughter, D.J. Lewis and P. O'Brien, Chemical Science, 8 (6) (2017) 4177-4187.

[7] M.A. Airo, S. Gqoba, M.P. Kalenga, S. Govindraju, M.J. Moloto and N. Moloto, Journal of Crystal Growth, 406 (2014) 1-7.
[8] S. Gqoba, M. Airo, N. Ntholeng, L. Machogo, R. Sithole, M.J. Moloto, J. Van Wyk and N. Moloto, Materials Today: Proceedings, 2 (2015) 3901-3908.
[9] G.E. Cranton and R.D. Heyding, Canadian Journal of Chemistry, 46 (16) (1968) 2637-2640.
[10] J.E. Cretier and G.A. Wiegers, Materials Research Bulletin, 8 (12) (1973) 1427-1430.
[11] L.F.E. Machogo, P. Tetyana, R. Sithole, S.S. Gqoba, N. Phao, M.A. Ario, P.M. Shumbula, M.J. Moloto and N. Moloto, Applied Surface Science, 456 (2018) 973-979.
[12] A. Rabenau and H. Schulz, Journal of the Less Common Metals, 48 (1) (1976) 89-101.
[13] N. Ntholeng, B. Mojela, S. Gqoba, M. Airo, S. Govindraju, M.J. Moloto and N. Moloto, New Journal of Chemistry, 40 (12) (2016) 10259-10266.
[14] M.D. Segall, P.J.D. Lindan, M.J, Probert, C.J. Pickard, P.J, Hasnip, S.J. Clark and M.C. Payne, Journal of Physics: Condensed Matter, 14 (11) (2002) 2717-2744.
[15] J.P. Perdew, K. Burke and M. Ernzerhof, Physical Review Letters, 77 (18) (1996) 3865-3868.
[16] Y. Pu, F. Cai, D. Wang and J-F. Chen, Industrial & Engineering Chemistry Research, 57 (6) (2018) 1790-1802.
[17] V.K. LaMer and R.H. Dinegar, Journal of the American Chemical Society, 72 (11) (1950) 4847-4854.
[18] A. Rabenau, H. Rau, and G. Rosenstein, Journal of the Less Common Metals, 23 (3) (1971) 291-299.
[19] S. Vorobyev, M. Likhatski, A. Romanchenko, N. Maksimov, S. Zharkov, A. Krylov and Y. Mikhlin, Minerals, 8 (11) (2018) 492.
[20] A. Atewologun, W. Ge, A.D. Stiff-Roberts, Journal of Electronic Materials, 42 (5) (2013) 809-814.
[21] I-S. Liu, H-H. Lo, C-T. Chien, Y-Y. Lin, C-W. Chen, Y-F. Chan, W-F. Sue, S-C. Liou, J. Materials Chemistry 18 (6) (2008) 675-682.
[22] A.M. Ferraria, A.P. Carapeto, A.M. Botelho do Rego, Vacuum, 86 (12) (2012) 1988-1991.
[23] J.P. Allen, D.O. Scanlon and G.W. Watson, Physical Review B, 81 (16) (2010) 161103.
[24] J.F. Weaver, G.B. Hoflund, J. Physical Chemistry, 98 (34) (1994) 8519-8524.
[25] G.B. Hoflund, Z.F. Hazos, Physical Review B, 62 (2000) 11126.
[26] X. Zhang, H. Shi, B.-Q. Xu, Angewandte Chemie. Int. Ed. 44 (2005) 7132.

[27] A.L. Allred, E.G. Rochow, Journal of lnorganic and Nuclear Chemistry, 5 (4) (1958) 264-268.
[28] H. Stammreich and R. Forneris, Spectrochimica Acta, 16(3) (1960) 363-367.
[29] G.I.N. Waterhouse, G.A. Bowmaker and J.B. Metson, Physical Chemistry Chemical Physics, 3 (17) (2001) 3838-3845.
[30] H. Li, Q. Zhang, C.C.R. Yap, B.K. Tay, T.H.T. Edwin, A. Olivier and D. Baillargeat, Adv. Funct. Mater., 22 (2012) 1385-1390.
[31] S. Mignuzzi, A.J. Pollard, N. Bonini, B. Bennan, I.S. Gilmore, M.A. Pimenta, D. Richards and D. Roy, Phys. Rev. B, 91 (2015)195411.
[32] l. Yang, X. Cui, J. Zhang, K. Wang, N. Shen, S. Zeng, S.A. Dayeh, L. Feng and B. Xiang, Scientific Reports, 4 (2014) 5649.
[33] I. Kriegel, C. Jiang, J. Rodríguez-Fernández. R.D. Schaller, D.V. Talapin, Enrico da Como and J. Feldmann, J. Am, Chem. Soc., 134 (2012) 1583-1590.
[34] S.K. Ghosh and T. Pal, Chemical Reviews, 107 (11) (2007) 4797-4862.

Chapter 5

Probing the structure and functionalized surface of colloidal AuSe

Abstract

Herein, we report on the colloidal synthesis of the less explored mixed valent compound, AuSe and investigate the influence capping agents; oleylamine (OLA), 1-dodecanethiol (IDDT) and oleic acid (OA) have on its structure and surface. TEM showed long belt-like structures for both OLA and OA-capped materials as opposed to nanorod structures for 1DDT-AuSe. XRD diffractograms and Raman spectra established the presence of both α- and β-AuSe polymorphs, with dominance of the alpha phase in all three materials. The extent of gold nanoparticle impurities in XRD suggests that 1DDT and OA have a higher reducing ability when producing AuSe. Furthermore, Raman spectroscopy revealed the presence of square planar geometry of the Au^{3+} ions. The vibrational bands of the methylene stretching frequencies in the FTIR spectra confirmed capping by the organic ligands. High resolution XPS spectra of the Au4f core level showed evidence of the Au^{+} ions, confirming the mixed valent nature of the nanocrystals. Compelling evidence of the Au-Se bond formation was obtained from the Se3d core level where a significant peak associated with the Au5p state was observed in all three samples. The high total peak area percentage of the Au^{+} ions (90%) in OLA-AuSe, compared to that of 1DDT (23%) and OA (21%), suggests that OLA is the best capping ligand of the three in producing gold selenide nanocrystals. DFT calculations on the adsorption of the ligands on AuSe showed weak interaction on (001) plane suggesting anisotropic growth along this plane and preference for the alpha phase.

Keywords: layered materials; gold selenide; Raman spectroscopy; XPS; capping agents

1. Introduction

Layered materials have proven to be a versatile class of materials due to their intrinsic features which expose them to a vast array of applications such as optical, electrical, thermal, energy conversion and storage [1]. Due to their unique physical, electronic and chemical properties they can be used in next-generation electronics [2, 3]. Bulk three-dimensional layered materials serve as parents to many two-dimensional materials. Several methods of fabrication exist and these include; top-down methods such as mechanical exfoliation of the bulk [4, 5] and bottom-up methods such as chemical vapour deposition (CVD) [6-8] as well as one pot colloidal synthesis [9, 10]. Colloidal synthesis offers substantial benefits including the ability to tune and control the size, shape and composition of the material. Since this tuning affords manipulation of the chemistry and physics at sub-micron and even nano level, colloidal synthesis has been the preferred choice of method in recent times. These effects can be achieved by variation of reaction parameters including but not limited to; change in time, temperature and capping agent (solvent). These capping agents (sometimes referred to as stabilizers, stabilizing agents or coordinating ligands) are employed to prevent aggregation, coalescence and unlimited or uncontrolled growth of the nanocrystals (NCs) [11]. Capping agents have great influence on the morphology of the nanomaterials as they often give guidance to the growth direction of the nanostructures. In addition to serving as reducing agents, their high boiling points offer the reactions an opportunity to reach high temperatures for easy precursor decomposition as opposed to aqueous based experiments. These stabilizers are normally large organic molecules with functional groups having different affinities to specific chemical environments which then results in preferential binding to certain crystal facets on the nanostructure, producing a defined and distinct shape [12]. For example, ligands having shorter chain lengths result in more branched nanostructures while those with longer chains allow for growth in the lateral direction [13]. In the present study, colloidal synthesis was employed using three most common capping agents with different functional groups; oleylamine (OLA) with an amine moiety, 1-dodecanethiol (1DDT) with a thiol head group and oleic acid (OA) having a carboxylic acid functional group. The effect of their respective binding groups was determined in the preparation of gold selenide (AuSe) nanocrystals. AuSe is a layered material that crystalizes in monoclinic space group C2/m with two polymorphs, α-AuSe and β-AuSe [14]. Fig. 1 shows the molecular structures of the three capping agents.

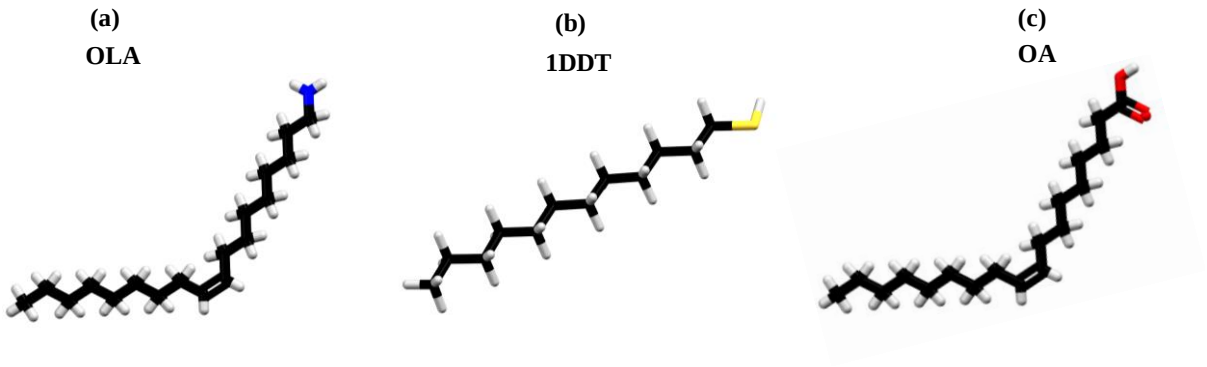

Fig. 1: 2D molecular structures of capping agents (a) oleylamine (OLA), (b) 1-dodecanethiol (1DDT) and (c) oleic acid (OA).

Unlike many other transition metal chalcogenides (e.g. CdSe, $MoSe_2$, and $InSe_2$) which have numerous reports on their structural properties, AuSe is vaguely understood with an electronic structure of much controversy, particularly in reference to the oxidation states of Au atoms in the system. Rabenau *et al.* discussed the mixed valency of both α- and β-AuSe with crystal structure analyses that showed two chemically different sites for Au atoms; one where Au is linearly bonded to two Se atoms and the other with Au bonded to four Se atoms in square planar fashion consequently assigned as Au^+ and Au^{3+} respectively thus giving $Au^+Au^{3+}Se_2$ [15]. This mixed valency finding was further supported by ^{197}Au Mossbauer studies conducted by Wagner *et al.* [16]. However, there have been contradicting reports that only depict evidence of the 1+ ions when using X-ray absorption and photoelectronic spectroscopy [17-19]. In a recent study by Machogo *et al*., evidence of the presence of the +3 ions in both α-AuSe and β-AuSe was depicted using Raman spectroscopy. This was seen in the Raman active vibrational modes of the square planar geometry $(Au^{3+}Se_4)^-$ ions, further confirming mixed valency of AuSe [20]. To the best of our knowledge, colloidal synthesis of AuSe has not been extensively explored apart from our preceding studies which focused on synthesis using solely OLA as a capping agent. The present study aims to outline the structural, vibrational, surface and electronic properties of AuSe brought about using the different surfactants.

2. Experimental

2.1 Chemicals

Gold (III) chloride hydrate 99%, 99% elemental selenium powder, oleylamine (OLA) 70%, oleic acid (OA) 90%, 1-dodecanethiol (DDT) 98%, toluene and 96% absolute ethanol were obtained from Sigma Aldrich and used without any further processing.

2.2 Synthesis of gold selenide

In a three-neck round bottom flask, 15 mL of capping agent (OLA/OA/1DDT) was added followed by purging of nitrogen gas to afford inert conditions. Under reflux and strong magnetic stirring, the solvent was heated to 100 °C followed by addition of 5 mmol selenium dissolved in the respective capping agent, the temperature was further raised to 200 °C and at this point 0.5 mmol gold chloride also dissolved in the respective capping agent was subsequently added. The reaction was carried out at 200 °C and aged for 1 hour. Ethanol was added to flocculate the particles as well was to wash off excess capping agent. AuSe materials were then collected by centrifugation and the black resultant powders were left to dry at room temperature before characterization.

2.3 Numerical simulations of the interaction of the capping ligands with AuSe surfaces

The molecular dynamics simulation in canonical ensemble (constant atom number, volume and temperature (NVT)) was utilized to fully understand the adsorption of OLA, OA and 1DDT on the surface of α- and β-AuSe polymorphs. The interaction energies between each ligand and α- and β-AuSe crystal facets were calculated. The three-dimensional models of each ligand and α- and β-AuSe complex are shown in concentration profiles in Table 3. A vacuum slab for each crystal was created and orientated along the c-plane with thickness of 20 Å, crystal thickness of 30 Å and 1 Å to position the crystal within the portion of vacuum slab. All simulations were executed by using the Forcite Module of Materials Studio. The COMPASS force field was used to calculate the intermolecular potential energy of the α- and β-AuSe crystals, ligands and complexes. The models indicating the absorption of the ligands were generated using absorption locator and sorption of BIOVIA Material Studio 2016 using COMPASS force field [21]. All systems were subjected to energy minimization for geometry optimization before molecular dynamics simulation. The molecular dynamic simulation using NVT lasted for 50 ps with a time step of 1 fs.

2.4 Characterization

Electron microscopy

Transmission electron microscopy (TEM) was carried out on a FEI Technai T12 TEM microscope operated at an acceleration voltage of 120 kV with a beam spot size of 3 in TEM mode. The samples were initially suspended in toluene followed by placing a drop of the suspended nanomaterials on a lacey-carbon copper grid. The grid was allowed to dry at room temperature before analysis.

X-ray diffraction

A Bruker D2 phaser (D2-205530) diffractometer using secondary graphite monochromated CuKα radiation (λ 1.5418 Å) at 30 kV and 10 mA was used to measure powder XRD patterns on the as-synthesized materials. Measurements were taken using a glancing angle of incidence detector at an angle of 2˚, for 2θ values over 5 - 90° in steps of 0.036° with a step time of 0.5 s/step and at a temperature of 25 °C.

Raman spectroscopy

Raman analysis was performed using a T64000 series II triple spectrometer system from HORIBA scientific, Jobin Yvon Technology. The Raman spectra were obtained using 514.5 nm argon laser, through an Olympus microscope with a 50 X objective lens and laser power of 1.5 mW.

Fourier Transform Infrared spectroscopy

Functional group for the organic solvent used was established using the Bruker TENSOR 27 Fourier Transform Infrared (FTIR) spectrophotometer.

X-ray photoelectron spectroscopy

X-ray photoelectron spectroscopy (XPS) measurements were performed with a Physical Electronics PHI 5700 spectrometer with a multi-channel hemispherical electron analyser. Non-monochromatic MgKα X-ray (300 W, 15 kV, and 1253.6 eV) was used as excitation source. The spectrometer energy scale was calibrated using Cu $2p_{3/2}$, Ag $3d_{5/2}$, and Au $4f_{7/2}$ photoelectron lines at 932.7, 368.3, and 84.0 eV, respectively. Samples were mounted on a sample holder without adhesive tape and kept overnight at high vacuum in the preparation chamber before being transferred to the analysis chamber for testing. The spectra were collected in the constant pass energy mode at 29.35 eV. The residual pressure in the analysis chamber was maintained below 1.33×10^{-7} Pa during the spectra acquisition.

3. Results and discussion

The ability to control the size and shape of NCs has become a valuable skill in nanotechnology. Numerous reports detail on the fundamental benefits of having the same material but with different morphologies which therefore have different properties and in turn informs on the diversity of their applications [22, 23]. The as-synthesized gold selenide nanomaterials which

resulted in black powders were characterized using various techniques. TEM was used to visualize the influence that the three capping agents have on the morphology of the NCs. Fig. 2 shows the OLA-capped AuSe (OLA-AuSe) and OA-capped AuSe (OA-AuSe) having long belt-like structures with various width. Although OLA and OA have different binding groups, they have the same chain length of saturated carbons except for carbon 9 and 10 which are double bonded together creating a slight kink in the molecules. The resultant morphology suggests that these capping ligands adsorbed on the basal sides of the AuSe nuclei and due to their length and the branched aspect of the molecules, create steric hindrance which allows for growth of the nuclei only in the lateral direction. The 1DDT-capped AuSe (1DDT-AuSe) NCs depicted much shorter and integrated rod-like structures in criss-cross layout. This morphology can be attributed to the shorter chain length of the ligand molecules (12 saturated carbons) which do not prohibit growth in various directions once adsorbed onto the nucleation site. Also observed in the 1DDT-AuSe sample were gold NCs. Even though these two morphologies (belt-like and criss-cross finger-like structures) may seem very different from one another, they all resemble 2D structures which are generally obtained from layered materials.

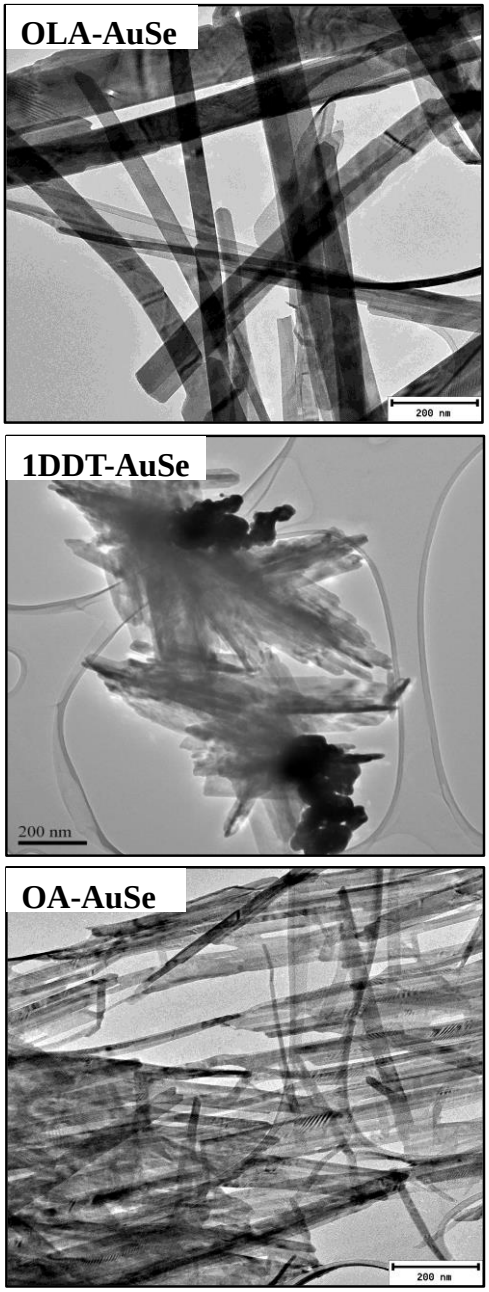

Fig. 2: TEM images of as-synthesized OLA-AuSe, 1DDT-AuSe and OA-AuSe nanocrystals.

Powder X-Ray diffraction was used to determine the phases of the AuSe NCs. Shown in Fig. 3 are the standard XRD patterns of elemental gold (PDF 00-004-0784), elemental selenium (PDF 00-006-0362), α-AuSe (PDF 00-020-0457) and β-AuSe (PDF 00-020-0458) together with experimental XRD patterns of the synthesized materials. All three capped-samples were of a polymorphic nature with both α and β-AuSe phase present. However, in all three cases alpha phase dominance was observed as indicated by the number of peaks attributed to the polymorph. Impurities of elemental selenium (marked with asterisks) and elemental gold

(marked with $) were also detected in all the samples. From the peak intensities, OLA-AuSe showed the least amount of Au impurities relative to 1DDT-AuSe and OA-AuSe which displayed this to a higher degree. This suggests higher reducing power of 1-dodecanethiol and oleic acid over that of oleylamine in the current study. Moreover, when using 1DDT, due to the strong affinity of sulphur to gold [24], once the reduction to Au^{+} occurs, the thiol molecules immediately adsorb onto their surfaces in a immobilizing manner prohibiting further activity. Impurities detected in XRD were not observed under TEM in their entirety, except for the gold nanocrystals imaged in the 1DDT-AuSe sample (Fig. 2).

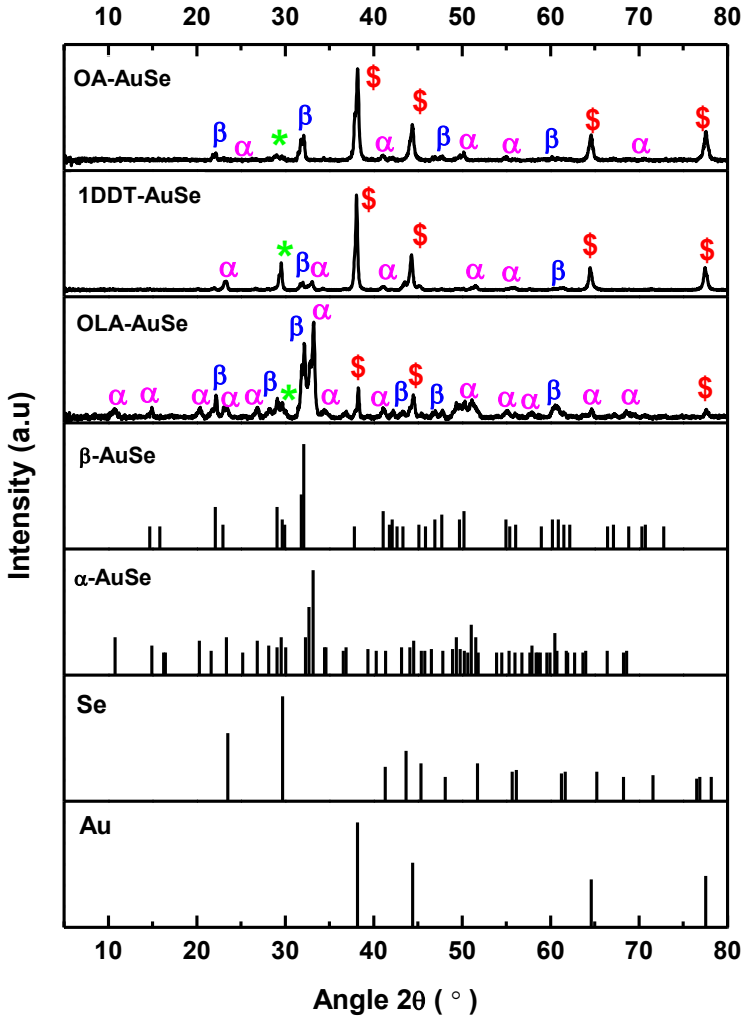

Fig. 3: Standard XRD patterns of elemental Au, elemental Se, α-AuSe & β-AuSe as well as powder XRD patterns of as-synthesized OLA-AuSe, 1DDT-AuSe and OA-AuSe. (Key: α = α-AuSe, β = β-AuSe, $ = elemental Au and * = elemental Se).

Raman spectroscopy was used as an additional technique to further characterize the structure of the nanocrystals. Machogo *et al*. ran theoretical calculations of the Raman spectra of both α-AuSe and β-AuSe using crystal data emanating from the crystal structure in Fig. 1 [20]. Using the data, only the square planar geometry showed Raman activity. Square planar molecules of MX^{n-} nature such as $(ICl_4)^-$, $(PtCl_4)^{2-}$ and $(AuCl_4)^-$ belong to the D_{4h} point group and their similarity to the $(Au^{3+}Se_4)^-$ ions in the current study was used to explain the obtained data. According to molecular symmetry, molecules belonging to D_{4h} point group give rise to seven vibrational normal modes of which three are Raman active.

Figure 4 presents the theoretical Raman spectra of α-AuSe and β-AuSe together with the experimental data for OLA-AuSe, 1DDT-AuSe and OA-AuSe NCs. From the α-AuSe spectrum, three peaks were observed. The intense shift at 232 cm^{-1} is attributed to the A_{1g} normal mode and is due to the symmetric stretching of the Au–Se bond. The peak at 265 cm^{-1} is attributed to the antisymmetric stretching B_{2g} mode while the low intensity peak at 176 cm^{-1} is assigned to the B_{1g} normal mode for planar bending. The calculated Raman spectrum of β-AuSe showed two prominent vibrational peaks at 201 cm^{-1} and 306 cm^{-1} which were assigned to symmetric A_{1g} and antisymmetric stretching B_{2g}, respectively. These theoretical assignments were in agreement with reported experimental vibrational modes of square planar pentatomic complex halides [25]. AgO ($Ag^+Ag^{3+}O_2$) is an analogue to AuSe, i.e. Ag^+ linearly bonded to two oxygen atoms while Ag^{3+} takes on a square planar geometry, it was of interest and therefore fitting to compare the Raman activity of AgO with that of AuSe. Three vibrational normal modes were observed similar to that of α-AuSe [26].

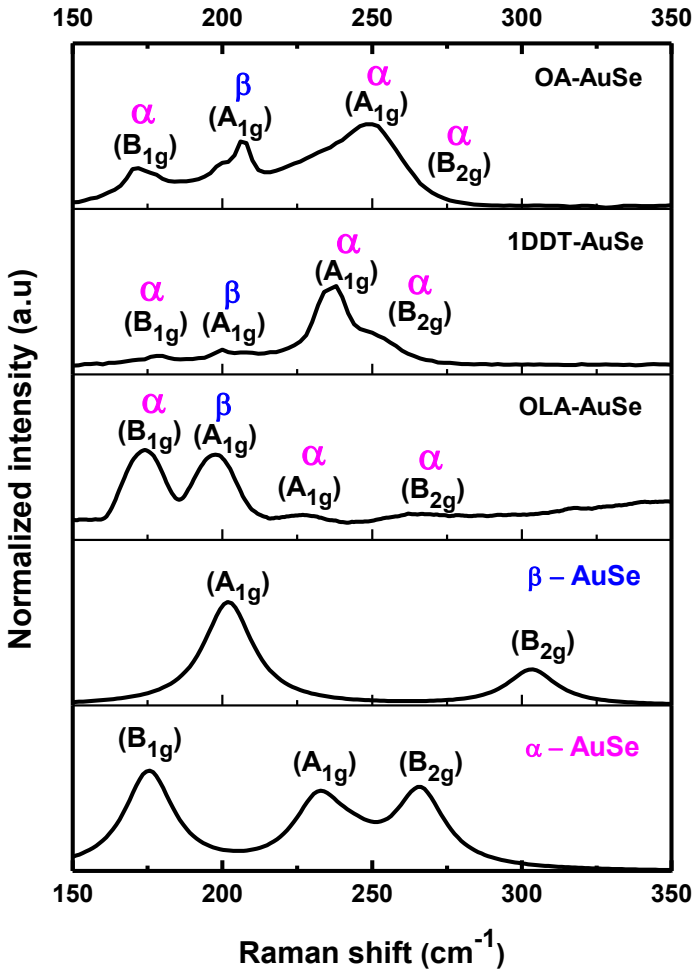

Fig. 4: Calculated Raman spectra of α-AuSe & β-AuSe and experimental Raman spectra of as-synthesized OLA-AuSe, 1DDT-AuSe, OA-AuSe nanocrystals.

All three materials revealed a mixture of α- and β-AuSe. The bending vibration (B_{1g}) in OLA-AuSe and OA-AuSe were observed at slightly lower wavenumbers of 174 cm^{-1} and 173 cm^{-1}, respectively, while that of 1DDT-AuSe was observed at a slightly higher position of 178 cm^{-1} compared to the theoretical Raman peak in α-AuSe at 176 cm^{-1}. The α-AuSe (symmetric & antisymmetric) stretching vibrations were observed at (224 cm^{-1} & 263 cm^{-1}), (238 cm^{-1} and 250 cm^{-1}) and (250 cm^{-1} and 260 cm^{-1}) for OLA-, 1DDT- and OA-AuSe, respectively. In addition to the α-AuSe peaks, one peak assigned to β-AuSe symmetric stretching vibration (A_{1g}) appeared at 196 cm^{-1}, 202 cm^{-1} and 206 cm^{-1} in OLA-AuSe, 1DDT-AuSe and OA-AuSe, respectively. The shifts in the experimental Raman peaks from the theoretical calculations may be as a result of the transitioning of layered materials from bulk to 2D monolayers, the presence of defects including intrinsic impurities or lattice strain induced by defects or type of morphology [27-29]. These results revealed that all samples contained both α- and β-AuSe

phases; however, they were dominated by peaks of the α-phase, a result also confirmed in XRD. Bands not identified may be either very weak or obscured by highly intense bands. The frequencies of the Raman shifts are summarized in Table 1.

Table 1: Summary of the Raman frequencies and their vibrational assignments

	B_{1g} Planar bending (cm^{-1})	**A_{1g} Symmetric stretching (cm^{-1})**	**B_{2g} Antisymmetric stretching (cm^{-1})**
Theoretical α-AuSe	176	232	265
OLA-AuSe	174	224	267
1DDT-AuSe	178	238	250
OA-AuSe	173	250	260
Theoretical β-AuSe		201	306
OLA-AuSe	-	196	-
1DDT-AuSe	-	202	-
OA-AuSe	-	206	-

To determine whether the three organic ligands were indeed capping the NCs, FTIR spectroscopy (represented in Fig. 5) was used to identify their key components and functional groups. OLA, OA and 1DDT all showed absorption bands attributed to the methylene asymmetric $\nu_{as}(CH_2)$ stretching and $\nu_s(CH_2)$ symmetric stretching at 2922 cm^{-1} and 2853 cm^{-1}, respectively while the methyl $\delta(CH_3)$ bending vibration was observed at 1469 cm^{-1}, this is in agreement with previous reported work [30-34]. The spectrum for pure OLA and OLA-AuSe unfortunately did not show evidence of the amine stretching frequency expected around 3000 cm^{-1}, however, the C-H aliphatic peaks were detected on all surfaces of the respective AuSe NCs indicating that the NCs were capped. The characteristic C=O group in OA was assigned to the absorption peak at 1704 cm^{-1} which disappeared upon binding onto the NCs further confirming binding to the NCs surface. The S-H stretching vibration in the 1DDT molecule expected at 2636 cm^{-1} could also not be depicted due to its weak nature.

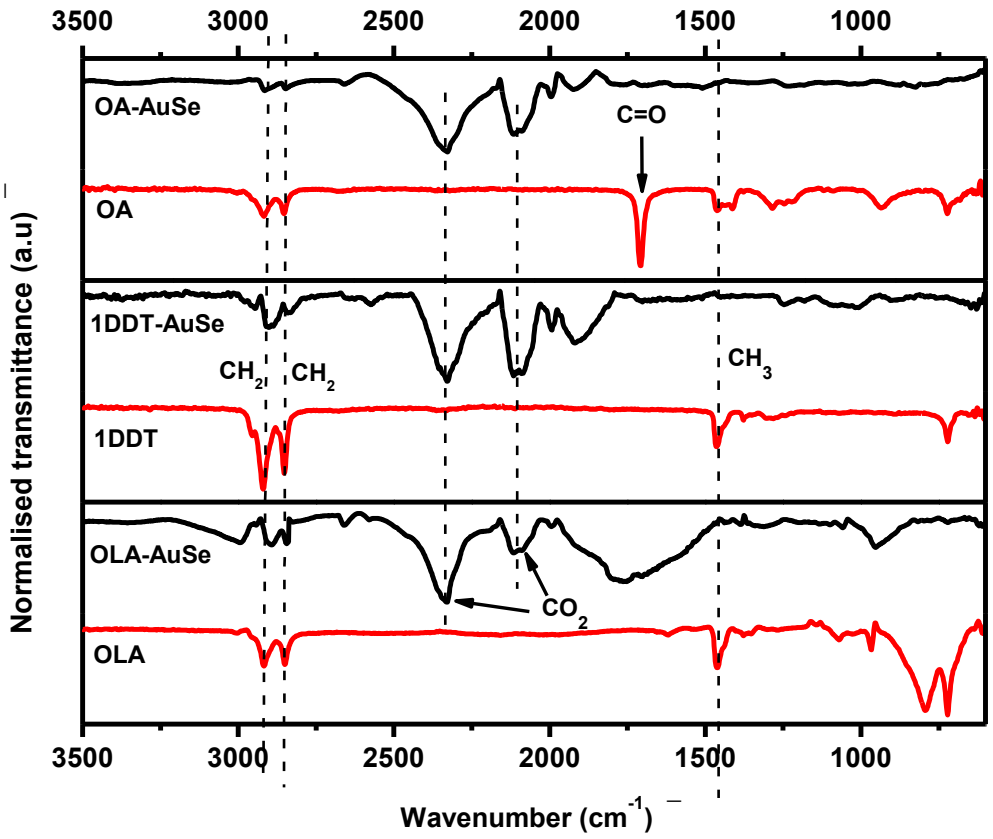

Fig. 5: FTIR spectra of the pure capping agents OLA, 1DDT and OA in red and that of the as-synthesized AuSe nanocrystals in black.

To investigate the surface properties of the AuSe NCs, XPS was performed. Survey spectra of all three samples are shown in Fig. 1S and these give a summary and an account for the elemental composition of the materials. The peaks are attributed to the respective elements of gold and selenium which make up the inorganic compound AuSe. Additionally observed, was carbon from the capping agents used and lastly oxygen which comes as a result of surface oxidation of the capping agents from exposure to the atmosphere. To further understand the bonding associated with the capping agents used as well as to examine their interactions with the surface of AuSe NCs, high resolution XPS was performed. Fig. 6 presents the core level spectra with focus on C1s, O1s, N1s and S2p (all elements associated with the capping ligands) for the as-synthesized materials. For all three samples, the C1s showed a pronounced peak at 284.8 eV attributed to the C-C bonds of the alkyl chains. Additionally, for OA-AuSe, the C1s spectra revealed peaks at 286.5 eV and 288.8 eV which were respectively assigned to the C-O and O-C=O bonds present in the ligand. The O1s core level for all samples displayed a peak at

532.2 eV assigned to C-O and is indicative of oxidation on the surface of the capping agents due to exposure to the atmosphere. The O1s spectrum of OA-AuSe showed two additional peaks, one at 532.6 due to the presence of the metal oxide (Au-O) and the second at 533.4 eV, ascribed to O-C=O, which comes as a result of OA binding onto the surface of gold selenide NCs with the two carboxylate oxygen atoms in a bidentate mode [35].

The absence of the amine group in the FTIR spectra, could not demonstrate the binding of OLA to the nanocrystal surface. However, the N1s core level spectrum of OLA- confirmed this by evidence of a peak at 403.3 eV. Sharma *et al*. stated that the region from 398 eV – 400 eV corresponds to the free or bonded amine group [36]. Moreover, they stated that peaks above 400 eV indicated the presence of N as a charged species, suggesting involvement of electrostatic interactions, particularly with nanoparticle surfaces. The blue shift in the peak of the current study at 403.3 eV strongly confirms binding of OLA with the AuSe surface and is comparable with other observations [37, 38]. Four peaks were observed in the S2p core level spectrum, 166.9 eV attributed to the S-O species of oxidized free/unbound 1DDT, the doublet at 163.6 eV ($2p_{3/2}$) and 164.8 eV ($2p_{1/2}$) which is indicative of the presence of sulphur species with slightly less negative charge, therefore confirming charge transfer from the AuSe nanocrystal surface to the S atom of bound 1DDT and 161.5 eV assigned to Au-S as this is the region where most metal thiolates are depicted [39, 40].

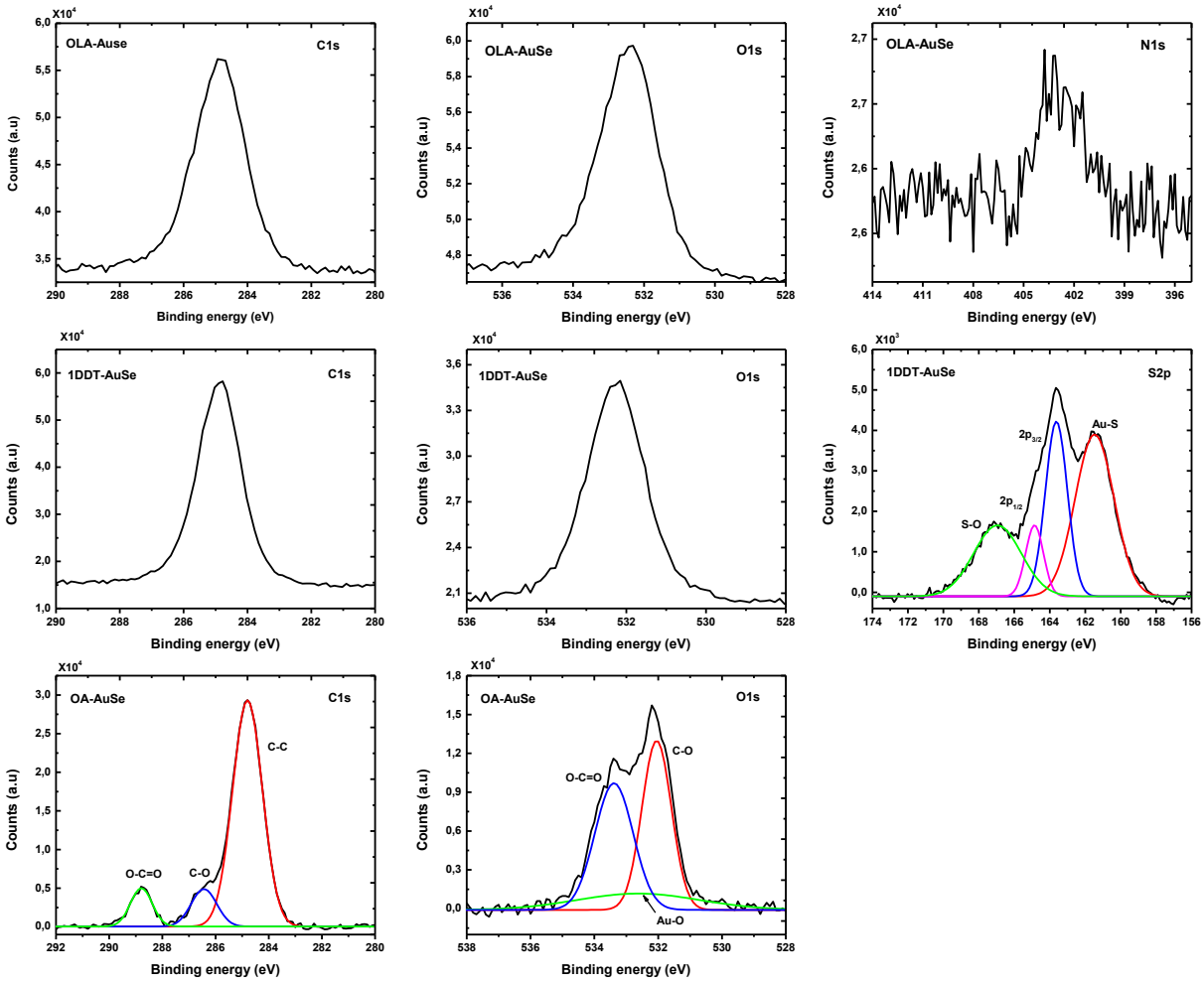

Fig. 6: High resolution XPS spectra with focus on core levels of C1s, O1s, N1s and S2p for OLA-AuSe, 1DDT-AuSe and OA-AuSe.

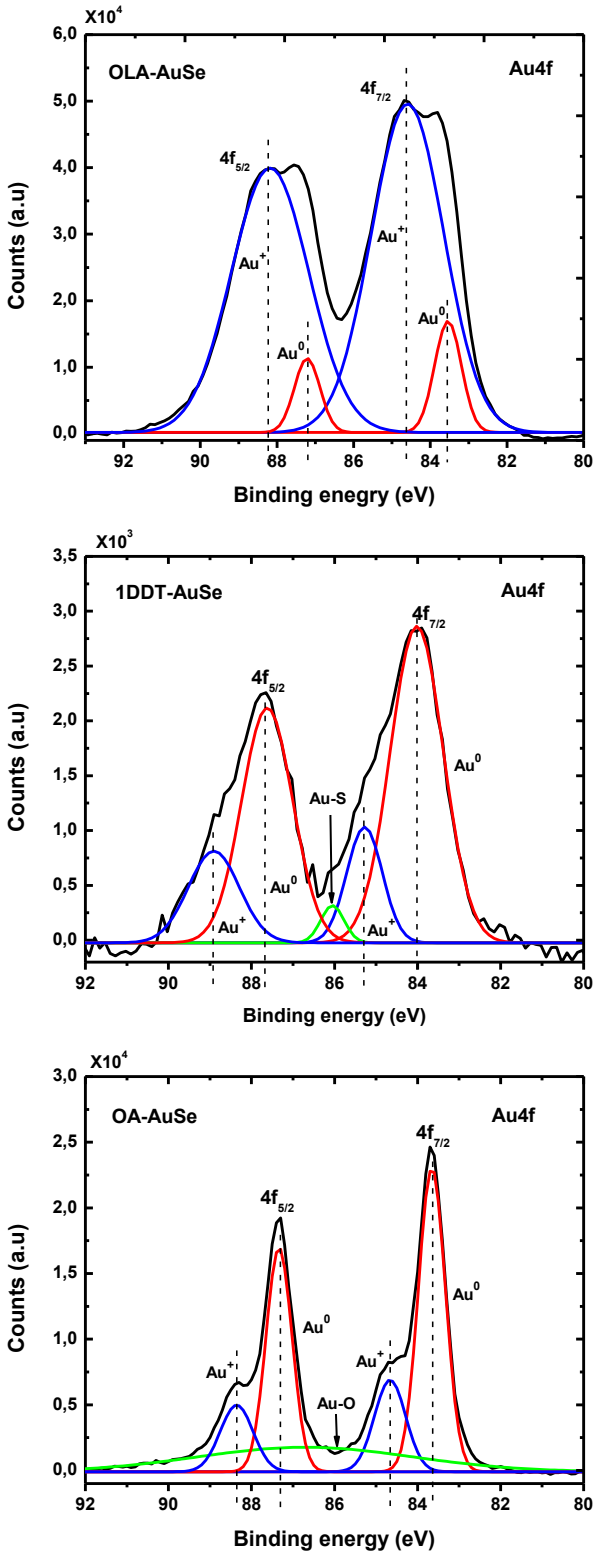

Fig. 7: High resolution XPS spectra with focus on the Au4f core level of OLA-AuSe, 1DDT-AuSe and OA-AuSe nanocrystals. (Deconvolution colour code: red curves = Au^0, blue curves = Au^+ and green curves = Au–X; where X = S or O).

The electronic structure of AuSe is of particular interest due to the complexities and intricacies surrounding the issue of the oxidation state of gold species in the system. Fig. 7 is the high resolution XPS spectra of the Au4f core level for the capped materials and it highlights key features and fundamental differences incurred when using the three surfactants. In all cases, the spectra contained a set of doublets for the $4f_{7/2}$ and $4f_{5/2}$ states, with a spin-orbit splitting of 3.7 eV for each set. The OLA-AuSe spectrum deconvoluted to 4 peaks at the following positions, 83.5 eV ($4f_{7/2}$) and 87.2 eV ($4f_{5/2}$) which were for the zero valent state, Au^0. The presence of Au^0 was also detected by XRD and therefore suggests formation of gold nanoparticles, which were however not observed in the TEM. The second sets of peaks were observed at 84.5 eV ($4f_{7/2}$) and 88.2 eV ($4f_{5/2}$) and were attributed to the monovalent state, Au^+. Of importance is the peak area percentage in Table 2, which shows a total of 9.9% for Au^0 and 90.1 % for Au^+ suggesting a large percentage of the material is AuSe. On the contrary, the opposite was observed for 1DDT-AuSe and OA-AuSe nanocrystals, for which Au^0 showed total peak area percentage of 74.8% and 57.6% whilst Au^+ was 23.0% and 20.8%, respectively. These results illustrated that a larger portion of the material was made of more gold nanoparticles than of AuSe NCs. This result is corroborated by the intense elemental gold peaks observed in the XRD diffractograms for the 1DDT and OA samples. For the 1DDT capped NCs, in addition to the sets of doublets at 84.0 eV ($4f_{7/2}$) and 87.7 eV ($4f_{5/2}$) for Au^0 and 85.2 eV ($4f_{7/2}$) & 88.9 eV ($4f_{5/2}$) for the Au^+ state, a peak at 86.0 eV was observed and is ascribed to the Au-S bonded thiolate species [41, 42]. The interfacial interactions between the gold and sulphur atoms involving partial charge transfer leaves the metal in an slightly positive state, $Au^{\delta+}$, which in turn shifts this species to higher binding energy [43]. This result is consistent with the peak observed in S2p spectrum in Fig. 7 at 161.5 eV. Much like 1DDT, OA was not as effective in producing AuSe as OLA and this is seen (in Fig. 8 OA-AuSe) where the Au^+: Au^0 peak ratio is 1:3 as opposed to 3:1 like in the OLA sample. The deconvoluted core level spectrum of OA-AuSe showed peaks at 83.6 eV ($4f_{7/2}$) and 87.3 eV ($4f_{5/2}$) for Au^0 and at 84.6 eV ($4f_{7/2}$) and 88.4 eV ($4f_{5/2}$) for the Au^+ ions. Due to the abundant availability of oxygen from the capping ligand, surface oxidation of the nanocrystals occurred and this was depicted by the appearance of a peak at 86.7 eV arising from slightly less negatively charged gold species as a result of Au-O surface interactions and partial charge transfer [44]. The presence of the metal oxide was also observed in the O1s spectrum at 532.6 eV in Fig. 7. Both phases of AuSe (α and β) are known to be mixed-valent compounds comprising of both Au^+ and Au^{3+}, however, these XPS results only show the existence of Au^+ nonetheless confirms the presence of the compound. The absence of the Ag^{3+} ions in XPS of mixed valent compound AgO [45], which

has a similar crystal structure as AuSe, highlights the complexities of probing these 3+ ions when using the technique.

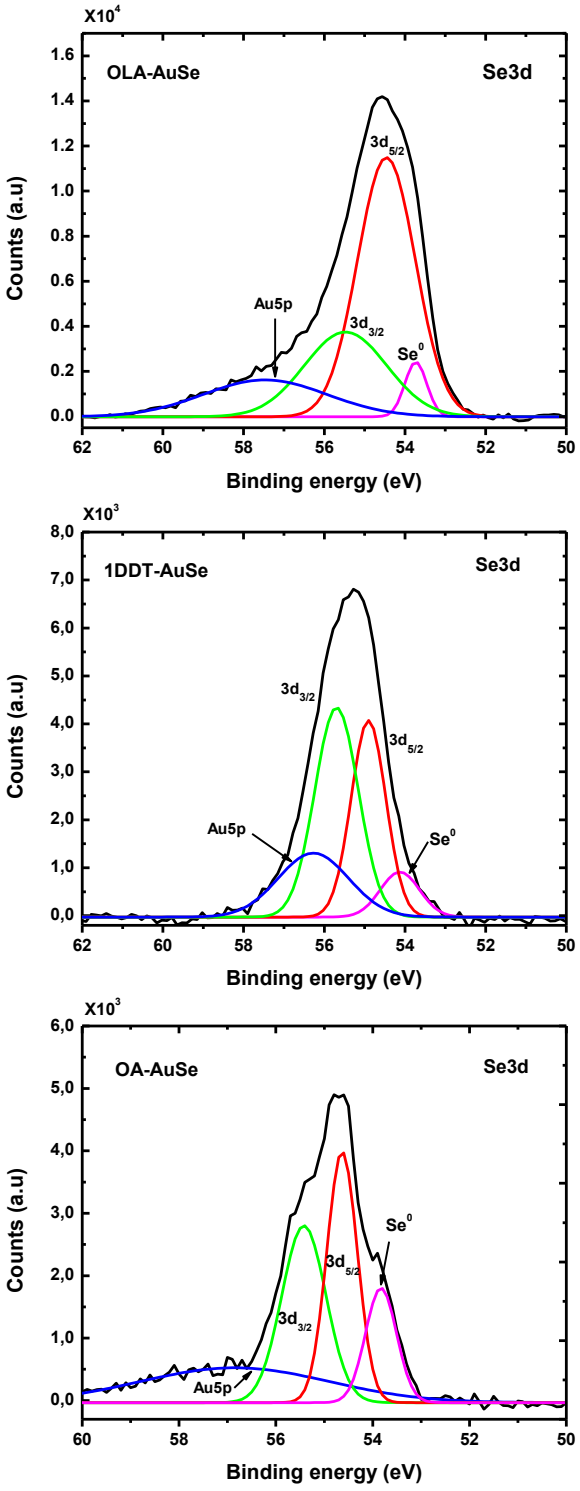

Fig. 8: High resolution XPS spectra with focus on the Se3d core level of OLA-AuSe, 1DDT-AuSe and OA-AuSe nanocrystals. (Deconvolution colour code: red curves = $3d_{5/2}$, green curves = $3d_{3/2}$, blue curves = Au 5p band and purple curves = Se^0).

To determine whether in fact gold was bonded to selenium, Se3d core level spectra for all three samples were collected and are presented in Fig. 8. Evidence of zero valent selenium is depicted at 53.7 eV for OLA-AuSe, at 54.1 eV for 1DDT-AuSe and at 53.8 eV for the OA-AuSe samples. These results are consistent with literature findings of Se^0 where the peak at 54 eV is due to the Se-Se bonds [46, 47]. The presence of elemental selenium was also observed in XRD. All three spectra also possessed a set of $3d_{5/2}$ and $3d_{3/2}$ doublets at; 54.4 eV and 55.4 eV, 54.8 eV and 55.6 eV and lastly 54.6 eV and 55.4 eV for OLA-, 1DDT- and OA-AuSe, respectively. These values were all slightly shifted to higher binding energy from that of Se^0, this shows that selenium atoms gained some charge transfer form Au species, which in turn strongly suggests Au-Se bond formation. Furthermore, a strong presence of the Au5p state was observed at 57.4 eV, 56.3 eV and 56.8 eV for the OLA-, 1DDT- and OA-capped NCs, respectively. This shows compelling evidence of the formation of AuSe and corroborates with the results observed in XRD. Table 2 gives a summary of the XPS results showing elemental composition and peak are percentages.

Table 2: Summary of the atomic composition and stoichiometric assignments obtained from fitting of XPS spectra reported in Fig. 7, 8 and 9 for the as-synthesised capped AuSe nanocrystals

Sample	Element	Atomic %	Peak Binding energy (eV)	Assignments	Peak area %	Sample	Element	Atomic %	Peak Binding energy (eV)	Assignments	Peak area %	Sample	Element	Atomic %	Peak Binding energy (eV)	Assignments	Peak area %
OLA-AuSe	**C**	54.8	284.8	C-C	100	1DDT-AuSe	**C**	71.4	284.8	C-C	100	OA-AuSe	**C**	76.9	284.8	C-C	79.0
															286.5	C-O	11.2
															288.5	O-C=O	9.7
	O	12.4	532.3	C-O	100		**O**	9.2	532.3	C-O	100		**O**	14.6	532.0	C-O	42.2
															532.6	Au-O	16.9
															533.4	C=O	40.9
	Au	13.6	83.5	Au^0 ($4f_{7/2}$)	5.9		**Au**	0.8	84.0	Au^0 ($4f_{7/2}$)	43.6		**Au**	4.8	83.6	Au^0 ($4f_{7/2}$)	33.6
			84.5	Au^{1+} ($4f_{7/2}$)	48.4				85.2	Au^{1+} ($4f_{7/2}$)	10.7				84.6	Au^{1+} ($4f_{7/2}$)	11.8
			87.2	Au^0 ($4f_{5/2}$)	3.8				86.0	Au-S	2.3				86.7	Au-O	21.6
			88.2	Au^{1+} ($4f_{5/2}$)	41.7				87.7	Au^0 ($4f_{5/2}$)	31.1				87.3	Au^0 ($4f_{5/2}$)	23.9
									88.9	Au^{1+} ($4f_{5/2}$)	12.7				88.3	Au^{1+} ($4f_{5/2}$)	8.9
	Se	19.2	53.7	Se^0	4.4		**Se**	6.8	54.1	Se^0	7.9		**Se**	3.6	53.8	Se^0	13.9
			54.4	$3d_{5/2}$	54.1				54.8	$3d_{5/2}$	30.7				54.6	$3d_{5/2}$	29.9
			55.4	$3d_{3/2}$	25.2.2				55.6	$3d_{3/2}$	41.0				55.4	$3d_{3/2}$	30.5
			57.4	$Au5p_{3/2}$	16.4				56.4	$Au5p_{3/2}$	20.3				56.8	$Au5p_{3/2}$	25.6
	N	0.8	403.3	*AuSe-N	100		**S**	11.7	161.6	Au-S	42.5						
									163.6	$2p_{3/2}$	25.9						
									164.8	$2p_{1/2}$	8.5						
									166.9	S-O	22.8						

To further investigate the influence of the capping agents on the morphology of the nanostructures, simulations were undertaken. The numerical simulations are shown in Table 3.1 and 3.2. The orbitals of all ligands were modelled to find the highest occupied molecular orbitals (HOMO) and the lowest unoccupied molecular orbitals (LUMO) to study their interaction with the surface of AuSe. The HOMO and LUMO of all ligands were relatively localized on the polar functional groups. This is indicative of the availability of electron clusters which can, therefore, interact with the surface of AuSe. Furthermore, computational simulation was performed to probe the adsorption of these ligands on the surface of α- and β-AuSe polymorphs. These were created following the reported crystal structure by Rabenau and Schulz [15]. They reported that the crystal structures form waved sheets which are connected by weak Au-Au and Se-Se bonds in α-AuSe and weak Au-Se bonds in β-AuSe. Moreover, it was established that the sheets grow parallel to the (001) plane for α-AuSe and (100) crystal plane for β-AuSe [15]. The simulations were therefore performed bearing the growth on the (001) and (100) crystal surface, and the (111) plane was also modelled to determine its contribution on the growth of these nanomaterials.

The interaction energy (U) of each ligand on each α- and β-AuSe polymorph was calculated. The presence of different crystal planes plays a significant role in directing the molecular adsorption of each ligand on the α- and β-AuSe polymorphs and this has great influence on the growth of the NCs. The interaction energy of α- and β-AuSe polymorphs were theoretically calculated to investigate the strength of each ligand's adsorption on the surface of α- and β-AuSe polymorphs, these values are shown in Table 3. The interaction energy (U) was calculated using the equation below:

$$U = E_{\text{AuSe-Ligand complex}} - E_{\text{Ligand}} - E_{\alpha\text{- or }\beta\text{-AuSe polymorphs}}$$

Where $E_{\text{AuSe-Ligand complex}}$ is the potential energy corresponding to complexes of each ligand with α- and β-AuSe (001), α- and β-AuSe (100) and, α- and β-AuSe (111) crystal surfaces. E_{Ligand} is the potential energy for each ligand molecule, $E_{\alpha\text{- or }\beta\text{-AuSe polymorphs}}$ is the potential energy for α- and β-AuSe (001), α- and β-AuSe (100) and, α- and β-AuSe (111) crystal surfaces.

Table 3.1: α-AuSe simulations

OLA Ligand		Theoretical Sorption Isotherm and surfaces			Binding Energies (Kcal/mol)		
HOMO	LUMO	(001)	(100)	(111)	(001)	(100)	(111)
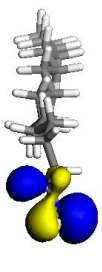		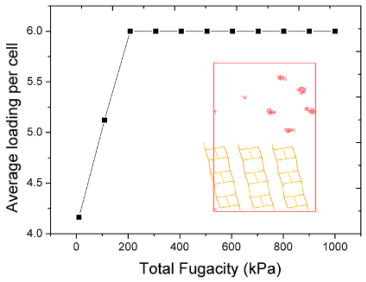	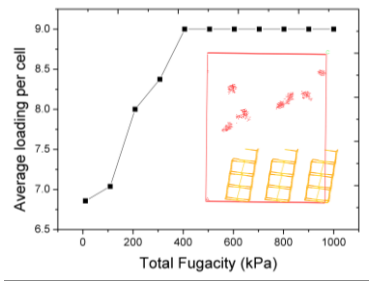	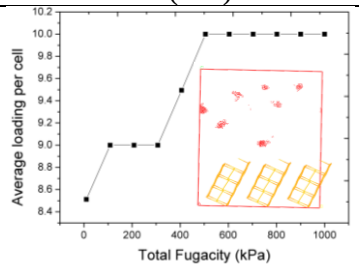	-153	-231	-255
1DDT Ligand							
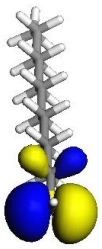	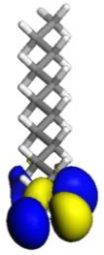	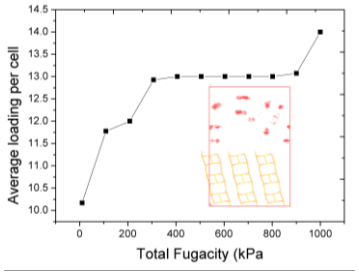	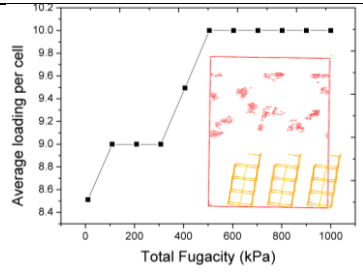	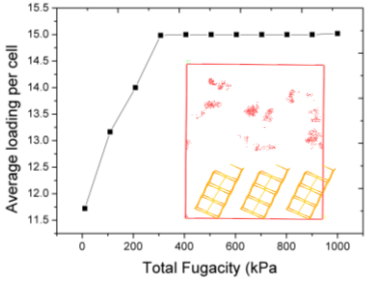	-287	-334	-348
OA Ligand							
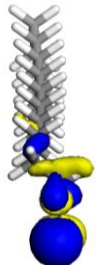	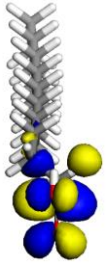	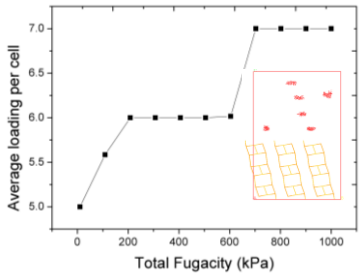	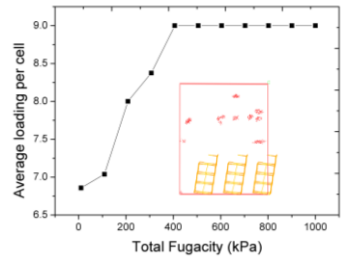	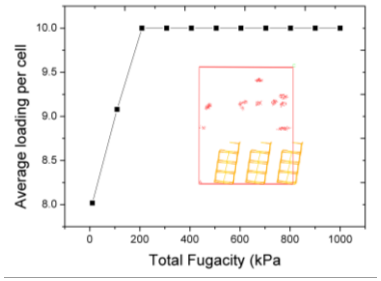	-204	-206	-267

Table 3.2: β-AuSe simulations

OLA Ligand		Theoretical Sorption Isotherm and surfaces			Binding Energies (Kcal/mol)		
HOMO	LUMO	(001)	(100)	(111)	(001)	(100)	(111)
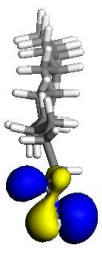		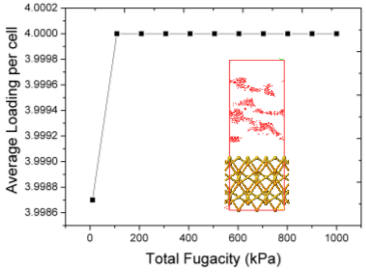	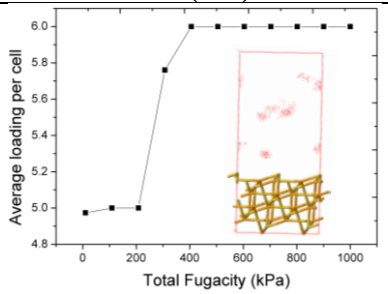	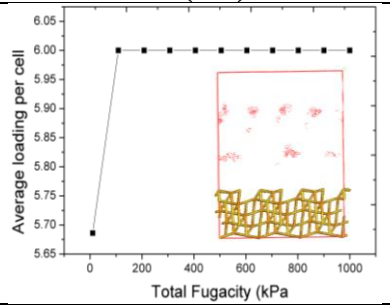	-100	-163	-159
1DDT Ligand							
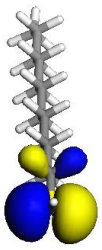		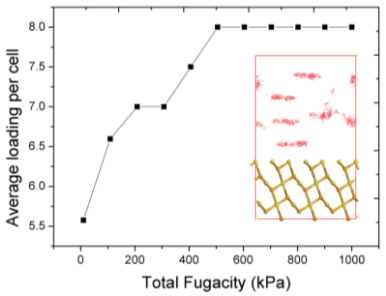	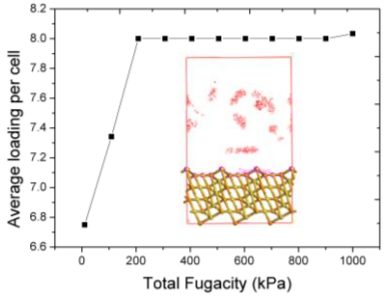	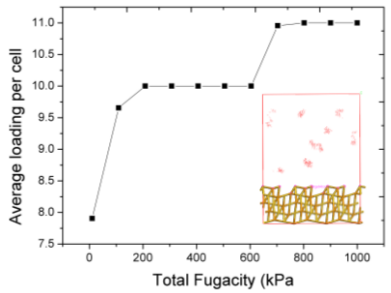	-201	-181	-280
OA Ligand							
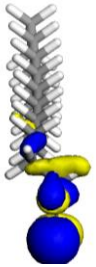	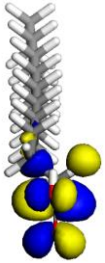	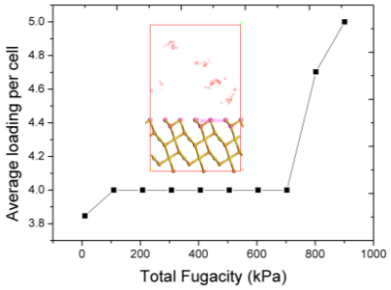	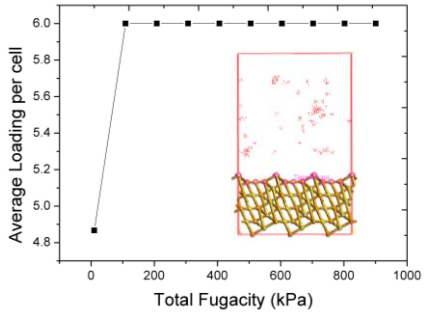	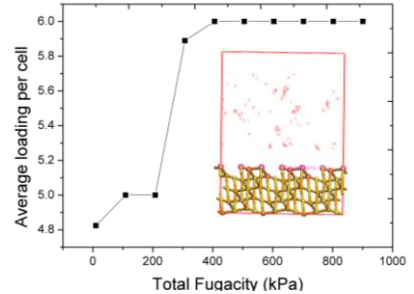	-154	-166	-158

For the α-AuSe simulations in Table 3.1, the sorption isotherms show that more 1DDT ligands are adsorbed on all the planes of the crystal as compared to OLA and OA. In addition, the binding energies for 1DDT are much higher than OLA and OA. This suggests that the surface of α-AuSe is highly passivated by 1DDT. Good passivation results in restrictive growth hence this is in agreement with the observed shorter rods in 1DDT capped nanocrystals as shown in Fig. 2. For all the ligands, the binding energies for the (001) plane are relatively low suggesting freedom for the nanocrystals to grow along this facet hence the observed anisotropic growth for all the samples. The results for β-AuSe are shown in Table 3.2. These are similar to α-AuSe, with 1DDT still showing a stronger interaction than the other two ligands based on the average loading of the ligands per cell as well as the binding energies. Nevertheless, the binding energies in all three crystallographic planes are quite similar and much lower than in α-AuSe. This, therefore, suggests that the NCs are capped equally on all facets therefore favouring a more isotropic type of growth. This is in agreement with Machogo *et al.* where α-AuSe was attributed to anisotropic nanobelts and β-AuSe to isotropic nanoplates [18, 20] and based on the XRD results, all the samples are predominantly α-AuSe.

4. Conclusions

In summary, colloidal synthesis of gold selenide nanomaterials was employed and the influence of oleylamine, 1-dodecanethiol and oleic acid was determined. OLA and OA revealed the same morphology of belt-like structures while 1DDT yielded short rod-like structures. The morphologies appeared to be more affected by the carbon chain length together with the functional head group. In all experiments, both α-AuSe and β-AuSe were formed; however, α-AuSe was the dominant phase. Raman spectra showed modes of both α- & β-AuSe were present in all three samples, further confirming the co-existence of both phases. Moreover, Raman confirmed the existence of Au^{3+} in the crystal structure. The vibrational bands of the methylene stretching frequency in FTIR confirmed capping of the nanocrystals by the organic ligands used. In all cases, the Au4f core level spectra in XPS was able to probe the Au^{+} ions, additionally the Se3d core level spectrum showed strong evidence of the formation of AuSe with the presence of the Au5p peak suggesting bonding of the selenium to gold. Peak area percentages of the Au^{+} state over the Au^{0} state suggested that OLA was the best capping agent of the three in producing AuSe nanomaterials. The use of both XPS and Raman was a breakthrough in elucidating the complex structure of this mixed valent material. The DFT simulations on the adsorption of OLA, 1DDT and OA on AuSe surfaces showed weak

interaction on (001) plane suggesting anisotropic growth along this plane and the anisotropic growth favours the alpha phase.

Conflicts of interest

There are no conflicts to declare.

Acknowledgments

The authors would like to thank the University of the Witwatersrand, School of Chemistry, and Wits Microscopy and Microanalysis Unit (MMU) for their facilities. Gratitude also goes to Mintek, Tiso Foundation and NRF for their generous financial support during the course of this study.

References

[1] D.J. Hynek, J.V. Pondick, J.J. Cha (2019) The Development of 2D Materials for Electrochemical Energy Applications: A Mechanistic Approach, APL Mater. 7: 030902.

[2] Y. Wang, N. Xu, D. Li, J. Zhu (2017) Thermal Properties of Two Dimensional Layered Materials, Adv. Funct. Mater. 27: 1604134.

[3] M. Bernardi, C. Ataca, M. Palummo, C. Grossman Jeffrey (2017) Optical and Electronic Properties of Two-Dimensional Layered Materials, Nanophotonics 6 (2) 479-493.

[4] H. Li, J. Wu, Z. Yin, H. Zhang (2014) Preparation and Applications of Mechanically Exfoliated Single-Layer and Multilayer MoS_2 and WSe_2 Nanosheets, Acc. Chem. Res. 47 (3): 1067-1075.

[5] H. Li, G. Lu, Y. Wang, Z. Yin, C. Cong, Q. He, L. Wang, F. Ding, T. Yu, H. Zhang (2013) Mechanical Exfoliation and Characterization of Single- and Few-Layer Nanosheets of WSe_2, TaS_2, and $TaSe_2$, Small 9 (11): 1974-1981.

[6] J. Xia, X. Huang, L.-Z. Liu, M. Wang, L. Wang, B. Huang, D.-D. Zhu, J.-J. Li, C.-Z. Gu, X.-M. Meng (2014) CVD Synthesis of Large-area, Highly Crystalline $MoSe_2$ Atomic Layers on Diverse Substrates and Application to Photodetectors, Nanoscale 6: 8949-8955.

[7] Y.-H. Lee, X.-Q. Zhang, W. Zhang, M.-T. Chang, C.-T. Lin, K.-D. Chang, Y.-C. Yu, J.T.-W. Wang, C.-S. Chang, L.-J. Li, T.-W. Lin (2012) Synthesis of Large-Area MoS_2 Atomic Layers with Chemical Vapor Deposition, Adv. Mater. 24: 2320-2325.

[8] G. Ye, Y. Gong, S. Lei, Y. He, B. Li, X. Zhang, Z. Jin, L. Dong, J. Lou, R. Vajtai, W. Zhou, P.M. Ajayan (2017) Synthesis of Large-scale Atomic-layer SnS_2 Through Chemical Vapor Deposition, Nano Res. 10 (7): 2386-2394.

[9] Y. Sun, F. Alimohammadi, D. Zhang, G. Guo (2017) Enabling Colloidal Synthesis of Edge-oriented MoS_2 with Expanded Interlayer Spacing for Enhanced HER Catalysis, Nano Lett. 17 (3) 1963-1969.
[10] M.A. Airo, S. Gqoba, F. Otieno, M.J. Moloto, N. Moloto (2016) Structural Modification and Band-gap Crossover in Indium Selenide Nanosheets, RSC Adv. 6: 40777-40784.
[11] L.M. Rossi, J.L. Fiorio, M.A.S. Garcia, C.P. Ferraz (2018) The Role and Fate of Capping Ligands in Colloidally Prepared Metal Nanoparticle Catalysts, Dalton Trans. 47: 5889-5915.
[12] M.S. Bakshi (2016) How Surfactants Control Crystal Growth of Nanomaterials, Cryst. Growth Des. 16: 1104-1133.
[13] M. Green (2010) The Nature of Quantum Dot Capping Ligands, J. Mater. Chem. 20: 5797-5809.
[14] A. Rabenau, H. Rau, G. Rosenstein (1971) Phase Relationships in the Gold-selenium System, J. Less-Common Metals, 24: 291-299.
[15] A. Rabenau, H. Schulz (1976) The Crystal Structures of α-AuSe and β-AuSe, J. Less-Common Metals 48: 89-101.
[16] F.E. Wagner, P. Palade, J. Friedl, G. Filoti, N. Wang (2010) 197 Au Mössbauer Study of Gold Selenide, AuSe, Journal of Physics: Conference Series, 217: 012039.
[17] A.R.H.F. Ettema, T.A. Stegink, C. Haas (1994) The Valence of Au in $AuTe_2$ and AuSe Studied by X-ray Absorption Spectroscopy, Solid State Commun. 90: 211-213.
[18] L.F.E. Machogo, P. Tetyana, R. Sithole, S.S. Gqoba, N. Phao, M. Airo, P.M. Shumbula, M.J. Moloto, N. Moloto (2018) Unravelling the Structural Properties of Mixed-valence α- and β-AuSe Nanostructures using XRD, TEM and XPS, Appl. Surf. Sci. 456: 973-979.
[19] S. Vorobyev, M. Likhatski, A. Romanchenko, N. Maksimov, S. Zharkov, A. Krylov, Y. Mikhlin (2018) Colloidal and Deposited Products of the Interaction of Tetrachloroauric Acid with Hydrogen Selenide and Hydrogen Sulfide in Aqueous Solutions, Minerals 8: 492
[20] L. Machogo, M. Mthimunye, R. Sithole, P. Tetyana, N. Phao, G.N. Ngubeni, M. Mlambo, P.S. Mdluli, P. Shumbula, N. Moloto (2019) Elucidating the Structural Properties of Gold Selenide Nanostructures, New J. Chem. 43: 5773-5782.
[21] A.K. Rappé, C.J. Casewit, K.S. Colwell, W.A. Goddard, W.M. Skiff (1992) UFF, a Full PeriodicTable Forcefield for Molecular Mechanics and Molecular Dynamics Simulations, J. Am. Chem. Soc. 114: 10024.
[22] X. Xiao, E. Han, Z. Zeng, L. Zhu, L. Li, Z. Liu (2019) Nanostructure $NiCo_2S_4$ with Different Morphologies Grown on Ni Foam for High-performance Supercapacitors, Ionics doi.org/10.1007/s11581-019-02840-w.

[23] K.-J. Huang, J.-Z. Zhang, Y. Fan (2015) One-step Solvothermal Synthesis of Different Morphologies CuS Nanosheets Compared as Supercapacitor Electrode Materials, Journal of Alloys and Compounds 625: 158-163.
[24] S. Engel, E.-C. Fritz, B.J. Ravoo (2017) New Trends in the Functionalization of Metallic Gold: from Organosulfur Ligands to N-heterocyclic Carbenes, Chem. Soc. Rev. 46: 2057-2075.
[25] H. Stammreich, R. Forneris (1960) RamanSpectra and Force Constants of Planar Square Molecules of the Type AB_4, Spectrochim. Acta, 16: 363-367.
[26] G.I.N. Waterhouse, G.A. Bowmaker, J.B. Metson (2001) The Thermal Decomposition of Silver (I, III) Oxide: A combined XRD, FT-IR and Raman Spectroscopic Study, Phys. Chem. Chem. Phys. 3: 3838-3845.
[27] H. Li, Q. Zhang, C.C.R. Yap, B.K. Tay, T.H.T. Edwin, A. Olivier, D. Baillargeat (2012) From Bulk to Monolayer MoS_2: Evolution of Raman Scattering, Adv. Funct. Mater. 22: 1385-1390.
[28] S. Mignuzzi, A.J. Pollard, N. Bonini, B. Brennan, I.S. Gilmore, M.A. Pimenta, D. Richards, D. Roy (2015) Effect of Disorder on Raman Scattering of Single-layer MoS_2, Phys. Rev. B 91: 195411.
[29] L. Yang, X. Cui, J. Zhang, K. Wang, M. Shen, S. Zeng, S.A. Dayeh, L. Feng, B. Xiang (2014) Lattice Strain Effects on the Optical Properties of MoS_2 Nanosheets, Scientific Reports, 4: 5649.
[30] R.A. Harris, P.M. Shumbula, H. van der Walt (2015) Analysis of the Interaction of Surfactants Oleic Acid and Oleylamine with Iron Oxide Nanoparticles through Molecular Mechanics Modeling, Langmuir 31: 3934-3943.
[31] R. Lontio Fomekong, J. Ngolui Lambi, G.R. Ebede, P. Kenfack Tsobnang, H.M. Tedjieukeng Kamta, C. Ngnintedem Yonti, A. Delcorte (2016) Effective Reduction in the Nanoparticle Sizes of NiO Obtained Via the Pyrolysis of Nickel Malonate Precursor Modified Using Oleylamine Surfactant, Journal of Solid State Chem. 241: 137-142.
[32] S. Mourdikoudis, L.M. Liz-Marzán (2013) Oleylamine in Nanoparticle Synthesis, Chem. Mater. 25: 1465-1476.
[33] P.I.P. Soares, C.A.T. Laia, A. Carvalho, L.C.J. Pereira, J.T. Coutinho, I.M.M. Ferreira, C.M.M. Novo, J.P. Borges (2016) Iron Oxide Nanoparticles Stabilized with a Bilayer of Oleic Acid for Nagnetic Hyperthermia and MRI Applications, Appl. Surf. Sci. 383: 240-247.

[34] N.K. Pal, C. Kryschi (2015) A Facile One-pot Synthesis of Blue and Red Luminescent Thiol Stabilized Gold Nanoclusters: a Thorough Optical and Microscopy Study, Phys. Chem. Chem. Phys. 17: 21423-21431.

[35] D. Wilson, M.A. Langell (2014), XPS Analysis of Oleylamine/Oleic Acid Capped Fe_3O_4 Nanoparticles as a Function of Temperature, Appl. Surf. Sci. 303: 6-13.

[36] J. Sharma, S. Mahima, B.A. Kakade, R. Pasricha, A.B. Mandale, K. Vijayamohanan (2004) Solvent-Assisted One-Pot Synthesis and Self-Assembly of 4-Aminothiophenol-Capped Gold Nanoparticles, J. Phys. Chem. B 108: 13280-13286.

[37] M. Bella, C. Rivero, S. Blayac, H. Basti, M.C. Record, P. Boulet (2017) Oleylamine-assisted Solvothermal Synthesis of Copper Antimony Sulfide Nanocrystals: Morphology and Phase control, Mater. Res. Bull., 90: 188-194.

[38] M. Aslam, E.A. Schultz, T. Sun, T. Meade, V.P. Dravid (2007), Synthesis of Amine-Stabilized Aqueous Colloidal Iron Oxide Nanoparticles, Cryst. Growth Des. 7: 471-475.

[39] Y. Yu, C.E. Rowland, R.D. Schaller, B.A. Korgel (2015) Synthesis and Ligand Exchange of Thiol-Capped Silicon Nanocrystals, Langmuir 31: 6886-6893.

[40] O.F. Odio, L. Lartundo-Rojas, P. Santiago-Jacinto, R. Martínez, E. Reguera (2014) Sorption of Gold by Naked and Thiol-Capped Magnetite Nanoparticles: An XPS Approach, J. Phys. Chem. C, 118: 2776-2791.

[41] Y. Negishi, K. Nobusada, T. Tsukuda (2005) Glutathione-Protected Gold Clusters Revisited: Bridging the Gap between Gold(I)−Thiolate Complexes and Thiolate-Protected Gold Nanocrystals, J. Am. Chem. Soc. 127: 5261-5270.

[42] Z. Tang, B. Xu, B. Wu, M.W. Germann, G. Wang (2010) Synthesis and Structural Determination of Multidentate 2,3-Dithiol-Stabilized Au Clusters, J. Am. Chem. Soc. 132: 3367-3374.

[43] J.A. Larsson, M. Nolan, J.C. Greer (2002) Interactions between Thiol Molecular Linkers and the Au13 Nanoparticle, J. Phys. Chem. B, 106: 5931-5937.

[44] A.Y. Klyushin, T.C.R. Rocha, M. Hävecker, A. Knop-Gericke, R. Schlögl (2014), A near ambient pressure XPS study of Au oxidation, Phys. Chem. Chem. Phys. 16: 7881-7886.

[45] A.M. Ferraria, A.P. Carapeto, A.M. Botelho do Rego (2012) X-ray Photoelectron Spectroscopy: Silver Salts Revisited, Vacuum 86: 1988-1991.

[46] C. Xing, Z. Xie, Z. Liang, W. Liang, T. Fan, J.S. Ponraj, S.C. Dhanabalan, D. Fan, H. Zhang (2017) 2D Nonlayered Selenium Nanosheets: Facile Synthesis, Photoluminescence, and Ultrafast Photonics, Adv. Optical Mater. 5: 1700884.

[47] C. Ray, S. Dutta, S. Sarkar, R. Sahoo, A. Roy, T. Pal (2013) A Facile Synthesis of 1D Nanostructured Selenium and Au Decorated Nano Selenium: Catalysts for the Clock Reaction, RSC Adv. 3: 24313-24320.

Chapter 6

Electrocatalytic activity of novel AuSe for potential use as a counter electrode in dye-sensitized solar cells

Abstract

Studies to improve the efficiency of dye-sensitized solar cells (DSSCs) include, but are not limited to, finding alternatives such as 2D layered materials as replacement counter electrodes (CEs) to the commonly used Pt. Herein, we report for the first time, the use of AuSe as a counter electrode for the reduction of triiodide ions (I_3^-) to iodide ions (I^-). The colloidal synthesis of gold selenide nanostructures produced α-AuSe and β-AuSe dominated products as determined by XRD. Electron microscopy showed α-AuSe having belt-like structures while β-AuSe had a plate-like morphology. EDS mapping confirmed the elemental composition and homogeneity of the AuSe CEs. Cyclic voltammetry curves of the AuSe CEs displayed the double set of reduction-oxidation peaks associated with the reactions in the I_3^- / I^- electrolyte and therefore were comparable to the Pt CV curve. The α-AuSe CE showed better electrocatalytic activity with a reduction current of 6.1 mA than that of β-AuSe and Pt CEs which were 4.2 mA and 4.8 mA respectively. The peak-to-peak separation (ΔEpp) for the α-AuSe CE was also more favourable with a value of 532 mV over that of the β-AuSe CE of 739 mV however both values were larger than that of the Pt CE which was found to be 468 mV. With some optimization studies, better values for AuSe can be obtained and this makes AuSe a viable alternative candidate for use as a CE in DSSCs.

Keywords: AuSe nanostructures; electrocatalyst; counter electrode; dye sensitized solar cells

1. Introduction

Dye-sensitized solar cells (DSSCs) have emerged as a powerful photovoltaic technology for low power and portable applications and have reached commercial maturity [1, 2]. In spite of this, the highest reported efficiency is 11.9% [3] apart from a recent record of 31.8% that was obtained under a standard Osram 930 Warm White fluorescent tube light at 1,000 lux intensity [4]. The functioning of DSSCs rely on the interconnection of a multicomponent system, therefore improving the device efficiency considers a multifaceted approach. Research efforts on the modification of some of the cell components have been explored, these include alternative synthesis methods for nanostructured semiconductor materials as the photoanode for high dye loading and fast electron transport, the search for dyes/sensitizers with strong visible light harvesting ability, redox electrolytes for fast and efficient hole transport, as well as substitutes for the electron-rich platinum (Pt) counter electrode (CE) [5-8]. The counter electrode is a key constituent which assists in collecting electrons from the external circuit passing them to the electrolyte which in turn donates these electrons to the previously oxidized dye molecules [9]. The key properties of a good CE material are; (i) high conductivity for charge transport, (ii) good electrocatalytic activity for reducing the electrolyte and (iii) excellent stability [10].

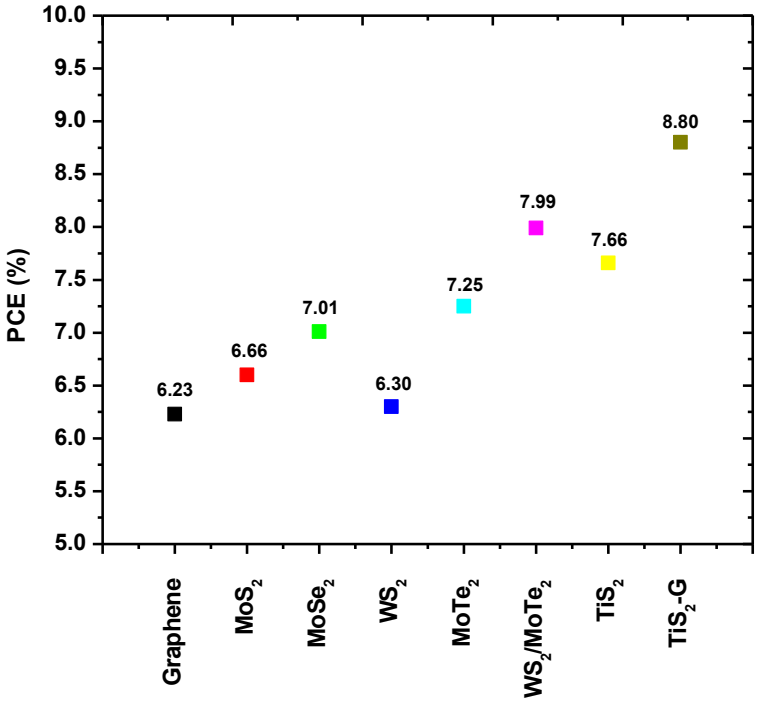

Fig. 1: A plot showing the trend in power conversion efficiencies (PCEs) of a few 2-dimensional layered transition metal chalcogenides.

To date, Pt has been the preferred CE choice due to its metallic nature and willingness to donate electrons, however, it is susceptible to corrosion by the commonly used liquid iodide-triiodide (I^-/I_3^-) electrolyte due to the formation of PtI_4 [11, 12]. Variations such as different carbonaceous materials, carbon-metal composites, polymers and inorganic materials such as metal chalcogenides and metal oxides have been explored as replacement CEs for platinum [5, 13-15]. In addition to the properties listed above, a high surface area is an added advantage for a counter electrode as it allows for faster catalytic redox activity. Transition metal chalcogenides with a two-dimensional layered structure have this feature and have therefore drawn much attention as potential alternative CEs in DSSCs [16]. Some of the reported power conversion efficiencies (PCEs) when using layered materials as CEs include; 6.23% for Graphene [17], 6.6% for MoS_2 [18], 7.01% for $MoSe_2$ [19], 6.30% for WS_2 [20], 7.25% for $MoTe_2$ [21] and 7.99% for $WS_2/MoTe_2$ [22], 7.66% for TiS_2 and 8.80% for TiS_2 nanosheets assembled and decorated on graphene (TiS_2-G) [13] as shown in Fig. 1. Another layered transition metal chalcogenide is gold selenide (AuSe), a relatively unexplored material which is electron rich and therefore has potential as a counter electrode material in DSSCs. AuSe crystalizes in monoclinic space group C2/m with two polymorphs, α-AuSe and β-AuSe with lattice parameters, a = 12.202(2) and 8.355(2) Å, b = 3.690(7) and 3.663(1) Å and c = 8.433(2) and 6.262(1) Å respectively. Both crystal phases of AuSe contain Au^{1+} and Au^{3+} where the $Au^{1+}$is coordinated linearly to two Se atoms whilst Au^{3+} is surrounded by four Se atoms in a square planar geometry [23]. Herein, we report for the first time, the electrocatalytic properties of α- and β-AuSe in the redox reaction of the iodide-triiodide system.

2. Experimental section

2.1 Chemicals

Gold (III) chloride hydrate 99%, 99% elemental selenium powder, oleylamine (OLA) 70%, toluene, 99.5% anhydrous 1-Methyl-2-pyrrolidinone (NMP), 99.9% lithium iodide, ≥ 99.8% iodine, ≥ 95.0% and ≥ 99.9% acetonitrile were obtained from Sigma Aldrich and used without any further processing. Absolute ethanol 99% was obtained from MK Chemical.

2.2 Synthesis of gold selenide

A. For the synthesis of the predominantly α-AuSe sample, in a three-neck round bottom flask, OLA was heated to 100 °C followed by the addition of 0.28 g selenium dissolved in OLA. The temperature was further raised to 200 °C and at this point 0.17 g gold

chloride trihydrate dissolved in OLA was subsequently added. The reaction was carried out at 200 °C and aged for 1 hour.

B. In the synthesis of the predominantly β-AuSe sample, OLA, selenium powder and gold chloride were all placed in a three-neck flask and the temperature was raised to 200 °C over a period of 20 min. Once the required temperature was reached the reaction was aged for 1 hour.

In both experiments, the mixtures were subjected to strong magnetic stirring and inert conditions during the heating as well as aging processes. Inert conditions were achieved by passing of nitrogen gas. Upon aging, ethanol was used to flocculate the particles as well as to wash off any excess OLA. The nanomaterials were then collected by centrifugation.

2.3.1 Characterization

X-ray diffraction

A Bruker D2 phaser (D2-205530) diffractometer using secondary graphite monochromated CuKα radiation (λ 1.5418 Å) at 30 kV and 10 mA was used to measure the powder XRD patterns on the as-synthesized materials. Measurements were taken using a glancing angle of incidence detector at an angle of 2°, for 2θ values over 5 - 90° in steps of 0.036° with a step time of 0.5 s/step and at a temperature of 294 K.

Transmission Electron microscopy

Transmission electron microscopy (TEM) was carried out on a FEI Technai T12 TEM microscope operated at an acceleration voltage of 120 kV with a beam spot size of 3 in TEM mode. The samples were initially suspended in toluene followed by placing a drop of the suspended nanomaterials on a lacey-carbon copper grid. The grid was allowed to dry at room temperature before analysis.

2.4 Fabrication of the counter electrode thin films

Fluorine doped tin oxide (FTO) glass substrates cut into 1 cm * 1.5 cm were cleaned with soapy water and sonicated for 10 min. This was followed by degreasing with acetone and sonication for a further 10 min. The slides were lastly placed in isopropanol and sonicated for 10 min and then left to dry. An ink was prepared by dissolving the as-synthesized AuSe in NMP followed by sonication for 30 min. The ink was deposited onto the FTO substrates by drop-casting a layer followed by baking on a hotplate to allow for evaporation of the solvent and a subsequent

layer was deposited and allowed to bake as previous. For the Pt-CE, two layers of platinum (Pt) was sputter coated onto a clean FTO substrate.

2.4.1 Characterization of the counter electrode (CE) thin films

Scanning Electron microscopy

Scanning electron microscopy (SEM) and energy dispersive spectroscopy (EDS) mapping were carried out on a VEGA3 TESCAN SEM microscope. The AuSe-CEs were mounted on aluminium stubs with carbon tape and analysed accordingly.

Cyclic voltammetry

Electrochemical measurements were carried out on a BASi epsilon E2(1231). A three-electrode system was used where Ag/AgCl electrode acted as the reference electrode, Pt wire as the auxiliary electrode and the prepared AuSe-CEs acted as the working electrode. The electrolyte was made of 49 mM $LiClO_4$, 9.85 mM I_2 and 50 mM LiI in acetonitrile. The electrolyte was purged with nitrogen gas before each scan.

3. Results and discussion

Materials used in this study were previously synthesized and discussed at great length in a previous publications [23]. X-ray diffraction was used to determine the phase of the as-synthesized powders. Fig. 2 shows the obtained diffraction patterns together with the matching standard patterns. For the two synthetic methods, mixed phased gold selenide samples were obtained with sample A having more peaks belonging to α-AuSe (PDF 00-020-0457) and sample B having more of the β-AuSe (PDF 00-020-0458) peaks. Both materials showed impurities of elemental Au (PDF 00-004-0784) and additionally sample B showed those of elemental Se (PDF 00-006-0362).

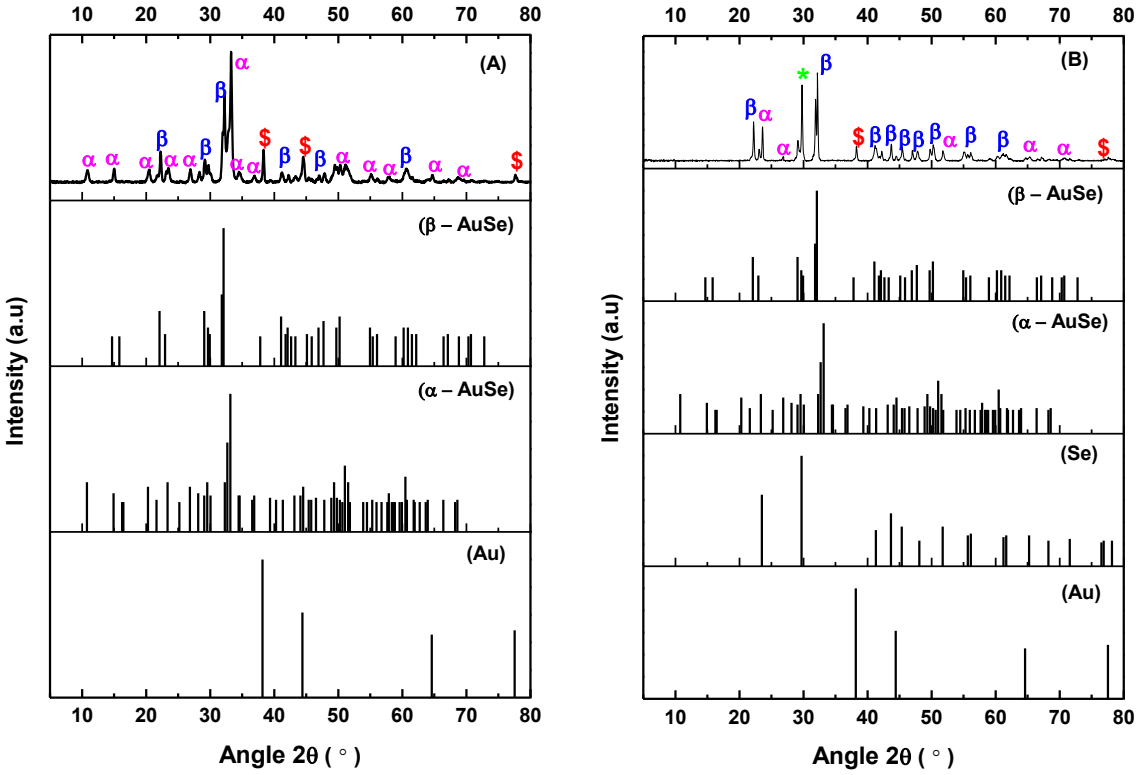

Fig. 2: Powder X-ray diffraction patterns of as-synthesized AuSe matched to standard powder patterns of α-AuSe, β-AuSe, and elemental Au and elemental Se. (Key: α = α-AuSe, β = β-AuSe, $ = elemental Au and * = elemental Se)

The morphology of the samples was analysed by TEM and the results are depicted in Fig. 3. Sample A revealed long belt-like structures of varying lengths and widths, on the other hand, sample B showed short plate-like structures. Owing to the sample distribution displayed on the copper grids (sample A having more belts and sample B showing more plates) it was concluded that the belts were of the α-phase while the plates were of β-phase.

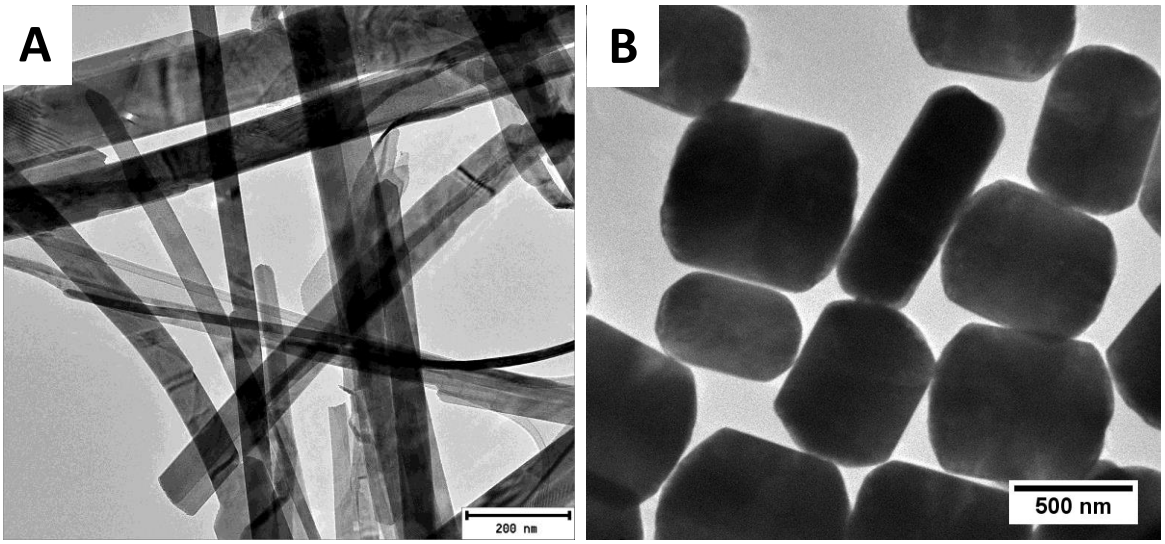

Fig. 3: TEM images of the as-obtained gold selenide materials. (A) showing the α-AuSe nanobelts and (B) the β-AuSe nanoplates.

Upon depositing the materials onto the FTO glass substrates, SEM was performed on the AuSe-CE films to confirm that no morphological changes occurred. Fig. 4(i) shows the images obtained during the SEM analysis where image A displays the aggregated nanobelts (α-AuSe CE) and image B shows the aggregated nanoplates (β-AuSe CE) unaltered. SEM-EDS mapping micrographs in columns (ii) and (iii) displayed even distributions of Au and Se throughout the films, respectively for both CEs. The summed mappings in column (iv) illustrates the uniformity in elemental distribution of both Au and Se giving complete homogenous AuSe-CEs.

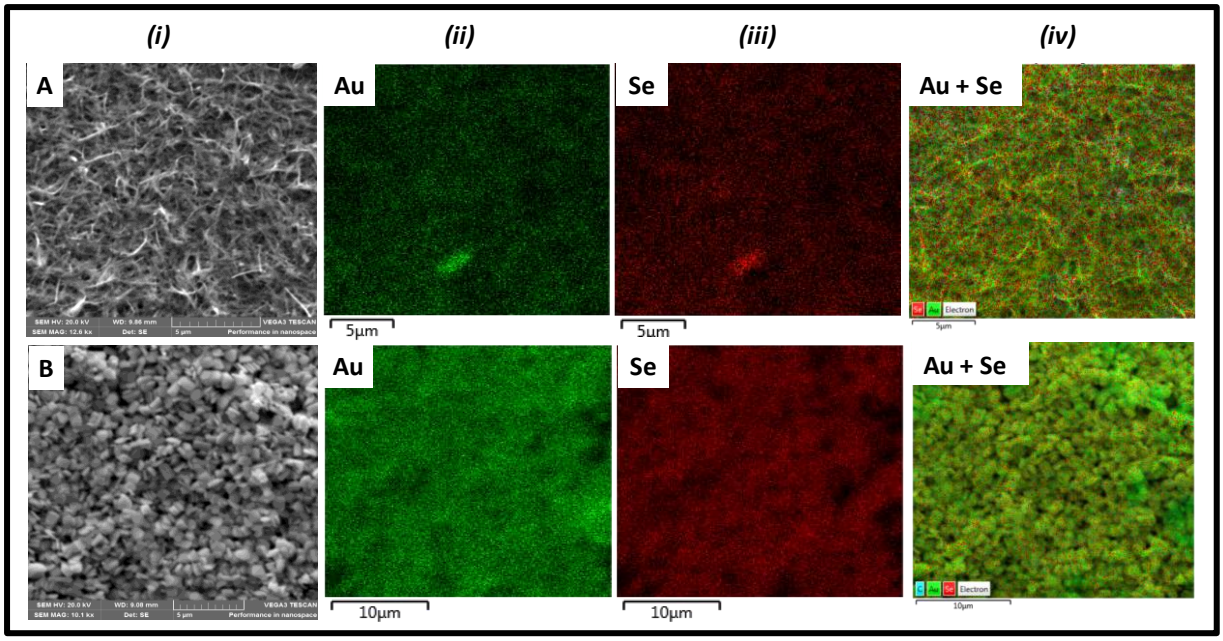

Fig. 4: (i) SEM images of (A) α-AuSe and (B) β-AuSe counter electrodes. Elemental mapping of (ii) Au, (iii) Se and (iv) summed mapping of Au and Se.

Elemental composition was further confirmed by EDS analysis as illustrated in Fig. 5. Both CEs contained Au, Se and traces of C attributed to the capping agent. In addition, the α-AuSe-CE (Fig. 4A) also showed Sn, Si and O which comes from the FTO glass substrate used, which may have not been completely covered with the as-synthesized materials.

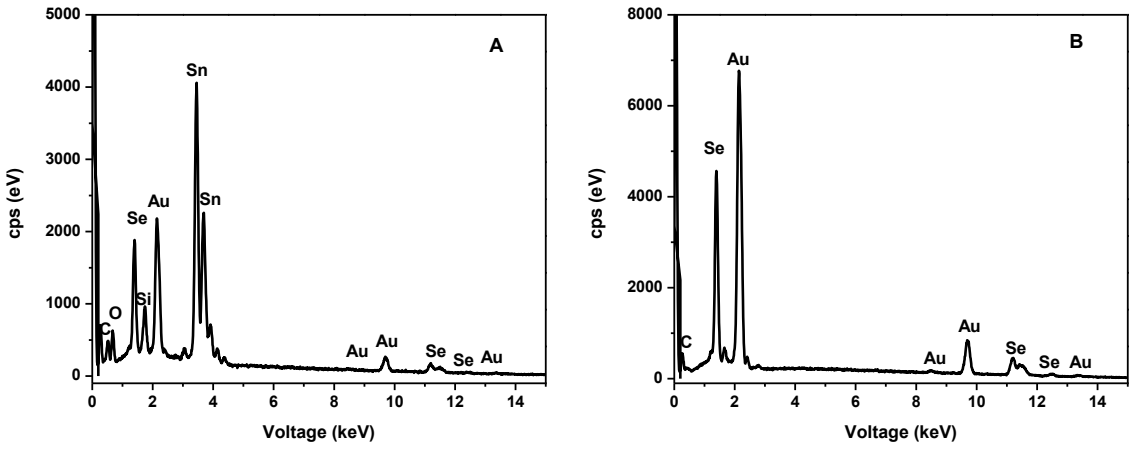

Fig. 5: SEM-EDS of (A) α-AuSe-CE and (B) β-AuSe-CE showing the elemental composition of the materials on the FTO glass substrates.

The electrocatalytic activity of the CEs for the I^-/I_3^- redox couple were evaluated using cyclic voltammetry (CV) at a scan rate of 100mV/s. Fig. 6 shows CV curves of the α-AuSe and β-AuSe CEs in comparison to that of the Pt CE. The curves of both AuSe CEs display similar duck shapes to that of Pt and therefore show compelling evidence that they can be used as alternative counter electrodes in DSSCs. The CV curves are composed of two pairs of reduction-oxidation peaks; the first pair on the left (Red_1/Ox_1) is ascribed to the $I_3^- + 2e^- \leftrightarrow 3I^-$ electron process, while the second pair (Red_2/Ox_2) is ascribed to the $3I_2 + 2e^- \leftrightarrow 2I_3^-$ electron movement [14, 24]. For a robust counter electrode, high electrical conductivity is expected in order to easily facilitate electron transfers from the external circuit to reduce the I_3^- ions [25].

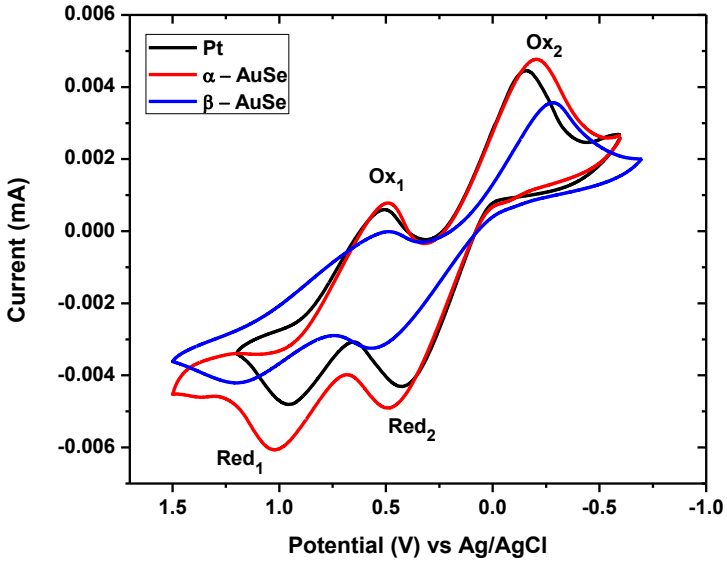

Fig. 6: Cyclic voltammograms of the Pt, α-AuSe and β-AuSe counter electrodes at a scan rate of 100 mV/s for the I^-/I_3^- redox couple.

Two parameters that speak to the quality and performance of the CE are deduced from the resulting CV curves. These are the cathodic peak absolute current of reduction |Current Red_1| and the change in peak-to-peak separation (ΔEpp) between Red_1 and Ox_1. A larger current and smaller Epp indicates good electrocatalytic activity of a CE [26]. Table 1 compares the discussed parameters for each CE, showing α-AuSe having a higher |Current Red_1| of 6.1 mA than that of Pt (4.8 mA) and β-AuSe (4.2 mA). The ΔEpp values are in the order of Pt < α-AuSe < β- AuSe. On the other hand, the nanobelt structure of α-AuSe gives them much larger

apparent surface area and active catalytic sites, leading to a higher current density than the Pt electrode. These findings suggest that the α-AuSe CE is the better of the two AuSe CEs.

Table 1: Summary of the absolute current and peak-to-peak separation (ΔEpp) of each CE

CE	|Current Red_1 (mA)|	ΔEpp (mV)
Pt	4.8	468
α-AuSe	6.1	532
β-AuSe	4.2	739

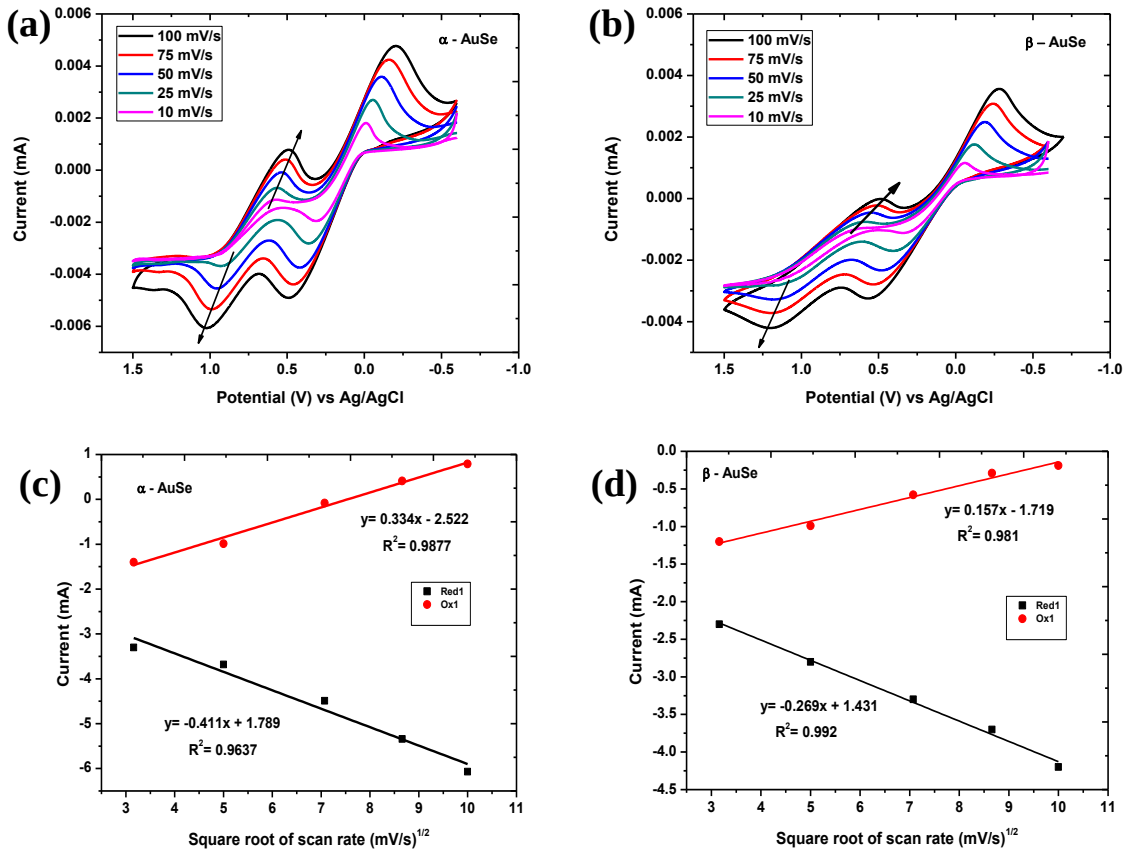

Fig. 7: Cyclic voltammograms for (a) α-AuSe and (b) β-AuSe CEs at varying scan rates from 10 mV/s to 100mV/s. Dependence of anodic and cathodic peak currents on square root of scan rates for (c) α-AuSe and (d) β-AuSe CEs.

The behaviour of the CEs over different scan rate conditions was investigated and is shown in Fig. 7 (a) and (b) for α-AuSe and β-AuSe, respectively. For both CEs there is an increase in |Current Red_1| and ΔEpp with an increase in scan rate. Of evidence is the disappearance of the

Red_1 peak at 10 mV/s suggesting this condition is not favourable for the reduction of triiodide ions using the AuSe CEs. Fig. 7(c) and 7(d) show the anodic and cathodic current as a function of the square root of scan rate for the two samples and the relationship is linear. This linear relationship reveals that the reaction of the I_3^-/I^- redox couple at both CEs is dominated by diffusion-controlled transport, and there is no specific interaction between the I_3^-/I^- redox couple and the CEs [26].

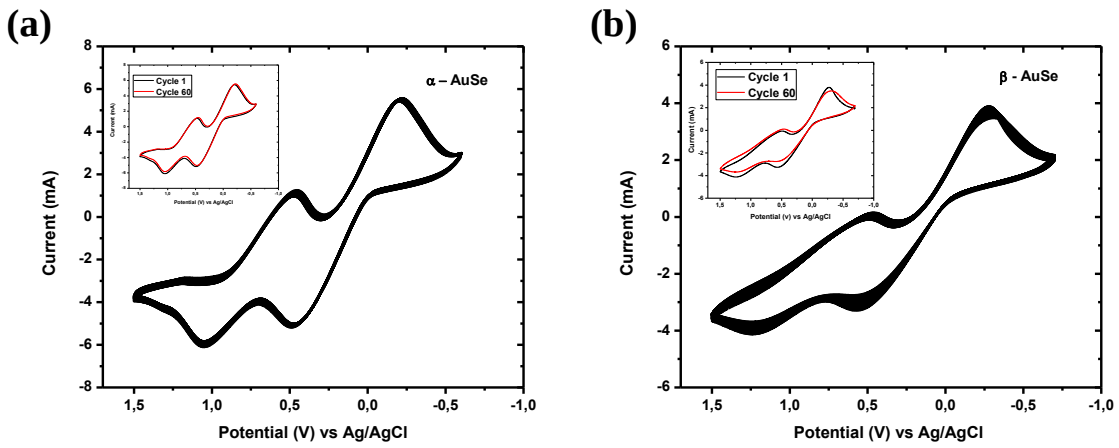

Fig. 8: Cyclic voltammograms for, (a) α-AuSe and (b) β-AuSe CEs for 60 consecutive cycles, with inserts showing the 1st and the 60th cycle for both electrodes.

The reproducibility and stability of the AuSe CEs were investigated at a scan rate of 100mV/s for 60 consecutive redox cycles and the resultant curves are presented in Fig. 8 (a) and (b) for α-AuSe and β-AuSe, respectively. There were minimal changes in the shapes of the CV curves. Inserts in the respective graphs show the first and sixtieth cycle and only slight changes were observed. This shows compelling evidence that the AuSe CEs possess excellent reversible redox activity and as well as good electrochemical and chemical stability.

4. Conclusion

In summary, colloidal gold selenide was successfully synthesized and the as-synthesized materials were effectively incorporated onto FTO glass to form homogenised counter electrode films. Powder XRD showed biphasic materials where both α and β-AuSe phases present in each sample, however, a level of dominance was observed in each. TEM depicted long belt-like structures for the α-AuSe dominated sample and short plate-like structures for the β-AuSe dominated sample. SEM analysis confirmed the morphology of the nanostructures on the CE films, it further validated the elemental composition with EDS mapping. Cyclic voltammetry

showed compelling evidence that both α-AuSe and β-AuSe have potential use in dye sensitized solar cells as counter electrodes with good electrocatalytic activity towards reduction of I_3^- ions in the iodide-triiodide redox couple. The higher cathodic peak current (|Current Red_1|) of 6.1 mA and lower ΔEpp value of 532 mV for the α-AuSe CE, makes it the more preferred of the two CEs, compared to 4.2 mA and 739 mV for the β-AuSe CE. The two AuSe CEs gave larger ΔEpp values than the Pt CE (468 mV), however with some optimization studies, better values can be attained. With these novel, preliminary results, AuSe can be used as an alternative counter electrode to Pt in dye sensitized solar cells.

Conflicts of interest

There are no conflicts to declare.

Acknowledgments

The authors would like to thank the University of the Witwatersrand, School of Chemistry, Wits Microscopy and Microanalysis Unit (MMU) for their facilities and Mr Siyasanga Mpelane at the University of Johannesburg for the worked performed on SEM analyses. Gratitude also goes to Mintek, Tiso Foundation and the NRF for their financial support.

References

[1] L. Li, X. Wang, Z. Ma, L. Liu, H. Wang, W. Zhang, X. Li, Applied Surface Science, 475 (2019) 109-116.

[2] K.S. Lee, Y. Lee, J.Y. Lee, J.-H. Ahn, J.H. Park, ChemSusChem, 5 (2012) 379-382.

[3] Y. Xie, Y. Tang, W. Wu, Y. Wang, J. Liu, X. Li, H. Tian, W.-H. Zhu, Journal of the American Chemical Society, 137 (2015) 14055-14058.

[4] Y. Cao, Y. Liu, S.M. Zakeeruddin, A. Hagfeldt, M. Grätzel, Joule, 2 (2018) 1108-1117.

[5] M. Ye, X. Wen, M. Wang, J. Iocozzia, N. Zhang, C. Lin, Z. Lin, Materials Today, 18 (2015) 155-162.

[6] J. Wu, Z. Lan, J. Lin, M. Huang, Y. Huang, L. Fan, G. Luo, Chemical Reviews, 115 (2015) 2136-2173.

[7] M.R. Narayan, Renewable and Sustainable Energy Reviews, 16 (2012) 208-215.

[8] S. Thomas, T.G. Deepak, G.S. Anjusree, T.A. Arun, S.V. Nair, A.S. Nair, Journal of Materials Chemistry A, 2 (2014) 4474-4490.

[9] D. Nechiyil, B.P. Vinayan, S. Ramaprabhu, Journal of Colloid and Interface Science, 488 (2017) 309-316.

[10] Y.-S. Yen, H.-H. Chou, Y.-C. Chen, C.-Y. Hsu, J.T. Lin, Journal of Materials Chemistry, 22 (2012) 8734-8747.
[11] S.S. Nemala, P. Kartikay, R.K. Agrawal, P. Bhargava, S. Mallick, S. Bohm, Solar Energy, 169 (2018) 67-74.
[12] E. Olsen, G. Hagen, S. Eric Lindquist, Solar Energy Materials and Solar Cells, 63 (2000) 267-273.
[13] X. Meng, C. Yu, B. Lu, J. Yang, J. Qiu, Nano Energy, 22 (2016) 59-69.
[14] X. Li, J. Bai, B. Zhou, X. Yuan, X. Zhang, L. Liu, Chemistry – A European Journal, 24 (2018) 11444-11450.
[15] U. Ahmed, M. Alizadeh, N.A. Rahim, S. Shahabuddin, M.S. Ahmed, A.K. Pandey, Solar Energy, 174 (2018) 1097-1125.
[16] E. Singh, K.S. Kim, G.Y. Yeom, H.S. Nalwa, RSC Advances, 7 (2017) 28234-28290.
[17] S.S. Nemala, P. Kartikay, S. Prathapani, H.L.M. Bohm, P. Bhargava, S. Bohm, S. Mallick, Journal of Colloid and Interface Science, 499 (2017) 9-16.
[18] S. Vijaya, G. Landi, J.J. Wu, S. Anandan, Electrochimica Acta, 294 (2019) 134-141.
[19] X. Yuan, B. Zhou, X. Zhang, Y. Li, L. Liu, Electrochimica Acta, 283 (2018) 1163-1169.
[20] S. Hussain, S.F. Shaikh, D. Vikraman, R.S. Mane, O.-S. Joo, M. Naushad, J. Jung, RSC Advances, 5 (2015) 103567-103572.
[21] S. Hussain, S.A. Patil, D. Vikraman, N. Mengal, H. Liu, W. Song, K.-S. An, S.H. Jeong, H.-S. Kim, J. Jung, Scientific Reports, 8 (2018) 29.
[22] S. Hussain, S.A. Patil, A.A. Memon, D. Vikraman, H.G. Abbas, S.H. Jeong, H.-S. Kim, H.-S. Kim, J. Jung, Inorganic Chemistry Frontiers, 5 (2018) 3178-3183.
[23] L. Machogo, M. Mthimunye, R. Sithole, P. Tetyana, N. Phao, G.N. Ngubeni, M. Mlambo, P.S. Mdluli, P. Shumbula, N. Moloto, New Journal of Chemistry, (2019).
[24] X. Qian, H. Li, L. Shao, X. Jiang, L. Hou, ACS Applied Materials & Interfaces, 8 (2016) 29486-29495.
[25] X. Wu, J. Duan, Y. Zhao, X. Yang, H. Chen, B. He, Q. Tang, Solar Energy, 180 (2019) 85-91.
[26] Q.S. Jiang, R. Chen, X. Guo, Y. Zhu, W. Cheng, W. Li, X. Yang, H.C. Chen, Solar Energy, 179 (2019) 59-66.

Chapter 7

Overall conclusions and recommendations

7.1 Conclusions

Herein, this thesis reports for the first time, synthesis of two-dimensional gold selenide layered nanomaterials. Studies comparing the molar ratios of gold to selenium precursors resulted in predominantly β-AuSe although α-AuSe was also formed. These phases came in two distinctly different morphologies; α-AuSe as long nanobelts and β-AuSe was nanospheres. Temperature studies resulted in the presence of excess unreacted selenium at lower temperatures of 160 °C whereas excess reduced gold was reported at higher temperatures (280 °C). Working temperature of 200 °C was thus chosen as the optimum due to less impurities observed. Variations in the sequence of precursor addition also produced both alpha and beta polymorphs. XRD illustrated that α-AuSe was the dominant phase when the gold precursor was added at elevated temperatures, contrary to the addition of gold at lower temperatures which presented β-AuSe as dominant. Again, α-AuSe was depicted as belt-like structures but β-AuSe had a plate-like morphology. The nanomaterials were homogenous in nature with an even distribution of gold and selenium as illustrated by TEM-EDS mapping of each particle.

Synthesis of AuSe using different capping agents was carried out, both phases, α and β-AuSe were produced, however for all three capping agents α-AuSe was predominant. OLA and OA produced nanobelts and 1DDT showed short rod-like nanostructures, this result was attributed mainly to the carbon chain length in addition to the attaching functional head group. The presence of both phases in all experiments suggests a level of co-dependency of one form to another. For all the as-synthesized AuSe samples, XPS showed the presence of Au^{+} ions in the crystal structure. In addition to the XRD results, XPS further confirmed the formation of AuSe. This was particularly evident in the Se3d core level spectra showing shifts in binding energies of selenium, which was attributed to the charge transfer from the gold atoms to the more electronegative selenium atoms. Moreover, strong presence of the Au5p peaks were also observed further suggesting selenium to gold bonding. The mixed valency of the AuSe system was confirmed by Raman spectroscopy when peaks ascribed to the square-planar geometry were observed. This geometry is described as having the Au^{3+} ions coordinated to four selenium atoms. The electronic properties of the nanomaterials proved the chemical formula to

be $Au^{+}Au^{3+}Se_2$ hence the reduced nomenclature, AuSe. Furthermore, Raman spectroscopy illustrated the presence of both polymorphs in the obtained samples, which corroborated the XRD results. Computational studies on the attachment of the capping agents on three different facets of AuSe showed that 1DDT had a tendency on binding strongly compared to OLA and OA hence restricting anisotropic growth. This was consistent with the TEM results where short rods were obtained for 1DDT capped particles and long belts were obtained for both OLA and OA capped particles.

The electrocatalytic properties of AuSe were investigated using cyclic voltammetry and were reported for the first time. The materials showed good redox catalytic activity towards the I^{-}/I_3^{-} electrolyte, illustrating the materials' potential use as a counter electrode in dye sensitised solar cells. Alpha-AuSe CE performed better with a lower ΔEpp value (532 mV) and a higher cathodic peak current of 6.1 mA than 739 mV and 4.2 mA for the β-AuSe CE in addition, the current density of α-AuSe was far better than Pt (4.8 mA) suggesting it can reduce the electrolyte far better than Pt and this is the most desirable property of a CE.

In summary, AuSe nanomaterials were successfully synthesized. The materials were composed of both α-AuSe and β-AuSe despite numerous attempts to produce pure single-phased materials. The type of morphologies adopted by the materials can be categorized into two groups; α-AuSe anisotropic and β-AuSe isotropic. An additional complexity to the synthesis is the outcome of excess unreacted precursors which needs to be thoroughly investigated, to obtain pure AuSe samples. However, that said, predominantly α-AuSe sample showed very good electrocatalytic properties and as such it can be used as a counter electrode in DSSCs.

7.2 Recommendations

Gold selenide is a relatively unexplored and under-reported material. The successful synthesis using facile and inexpensive colloidal methods opens its territory for more exploration in better understanding the inorganic layered compound. Apart from its complex structure, its good electrocatalytic performance in the iodide-triiodide redox couple makes it a promising and more stable alternative for the corrosion prone Pt metal as a counter electrode in DSSCs.
Future work would include but not limited to:

- The use of ^{197}Au Mössbauer spectroscopy to further probe the properties of AuSe.

- A better understanding of the co-dependency of the two polymorphs perhaps using theoretical simulations and to find solutions on isolation methods in order to obtain pure phases.
- To use gold complexes as single source precursors and see if these will reduce the impurities and control the crystal phase.
- To study the electrocatalytic properties using electrochemical impedance spectroscopy.
- To fabricate the DSSC device based on α-AuSe as a CE and investigate whether the device will outperform the platinum-based device.

Appendix

Chapter 3: Supporting information

Unravelling the structural properties of mixed-valence α- and β-AuSe nanostructures using XRD, TEM and XPS

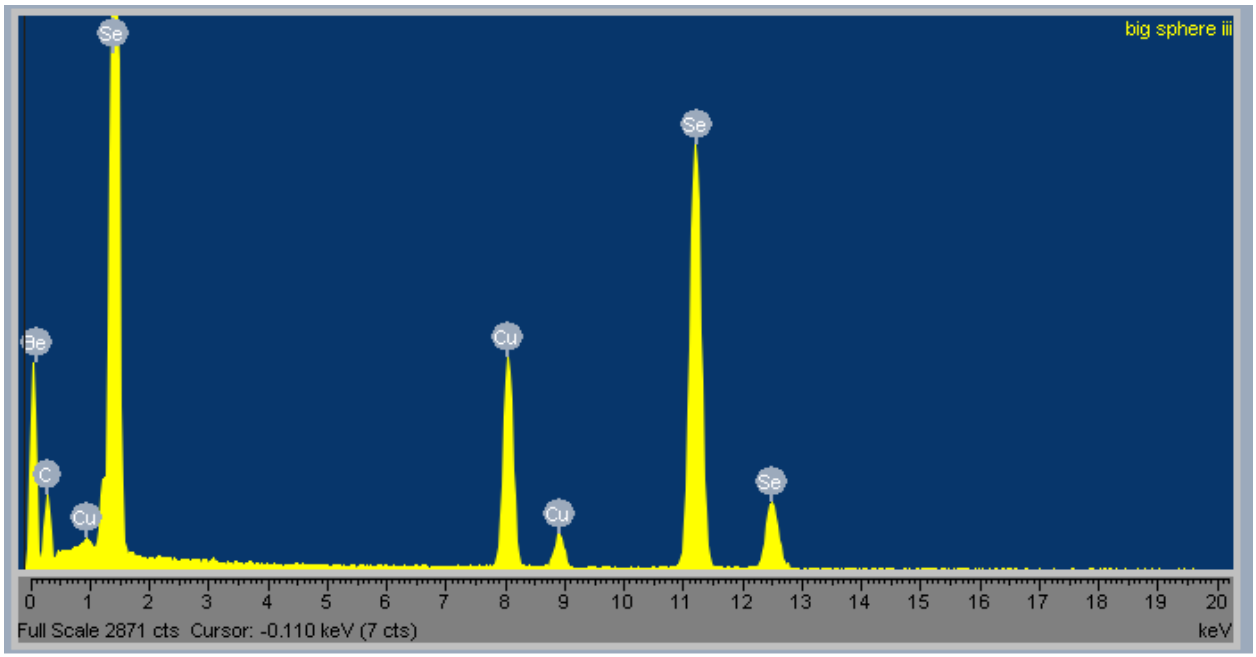

Fig. 1S: EDS spectrum of the fused spheres showing the presences of selenium only. No gold peaks were detected. The Cu and C are attributed to the carbon coated copper grid.

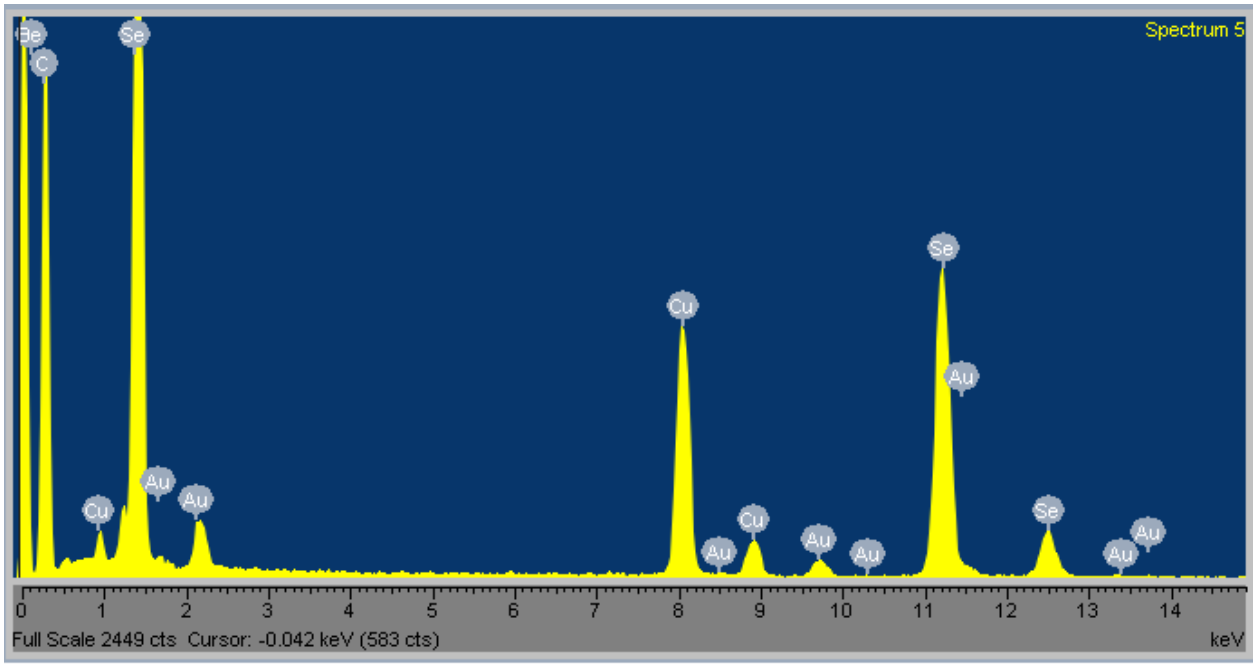

Fig. 2S: **EDS spectrum of agglomerated nanorods showing the presence of both Au and Se. The Cu and C peaks are attributed to the carbon coated copper grid.**

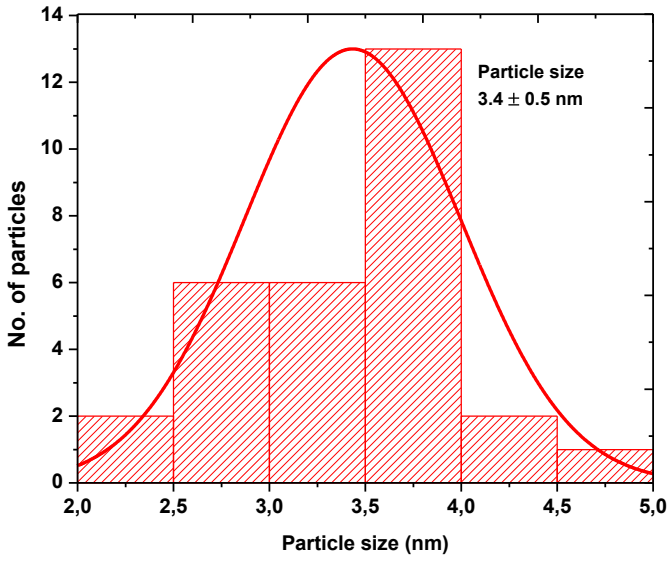

Fig. 3S: Histogram showing particle size distribution of the tiny particles on the nanobelts.

Probing the structure and functionalized surface of colloidal AuSe

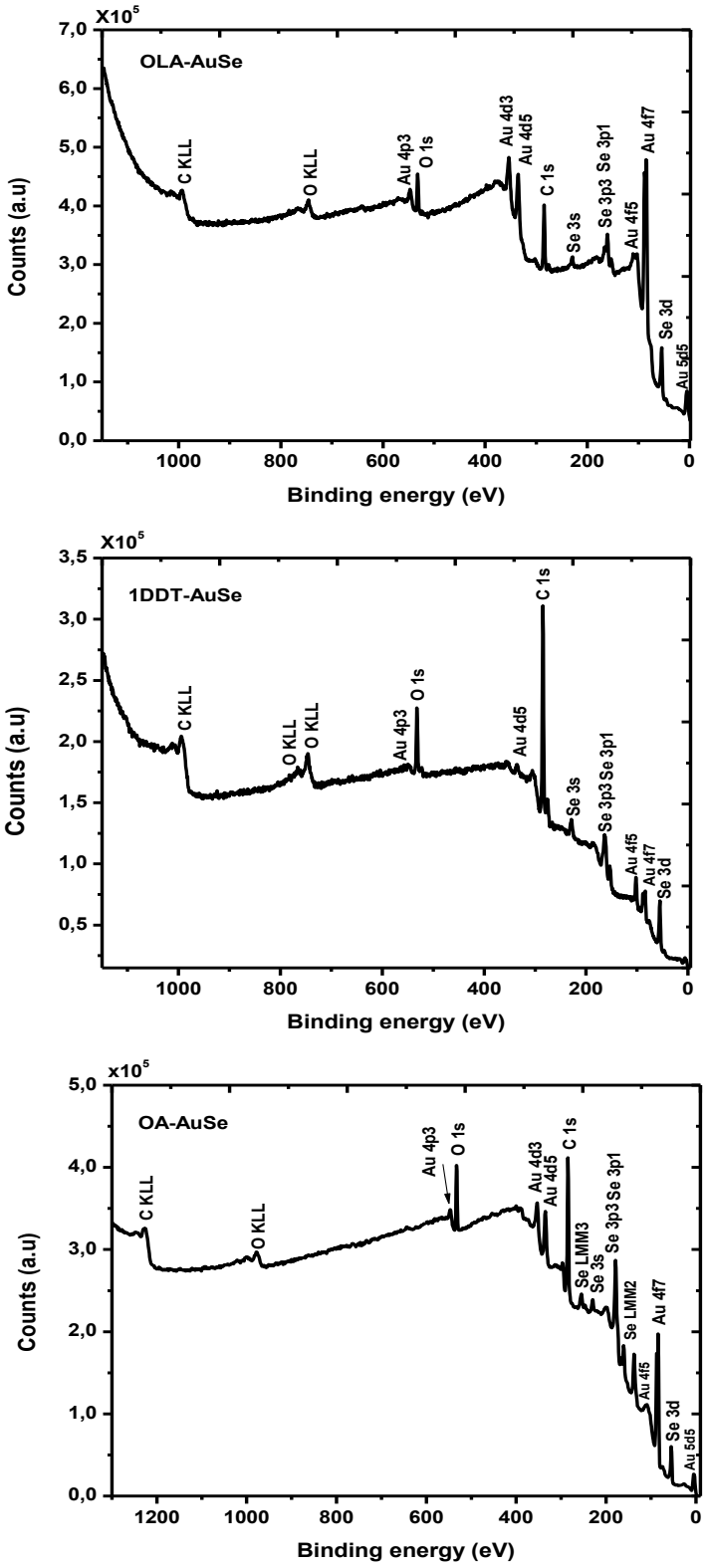

Fig. 1S: XPS survey spectra of OLA-AuSe, 1DDT-capped AuSe and OA-AuSe nanomaterials.